Quantification of vascular morphogenesis in the chick embryo and its relationship to the hemodynamic environment

Submitted in partial fulfillment of the requirements for

the degree of

Doctor of Philosophy

in

Biomedical Engineering

William J. Kowalski

B.E., Biomedical Engineering, Stevens Institute of Technology

Carnegie Mellon University
Pittsburgh, PA

December, 2013

Acknowledgements

I express my gratitude to my advisor, Dr. Kerem Pekkan, for giving me the opportunity to learn and develop new skills under his guidance. His supervision allowed me to cultivate an interdisciplinary knowledge base and pursue research projects that truly interested me. I am also grateful for Dr. Brad Keller, who often acted as a secondary advisor and always provided a sharp, clinical perspective to my work. My thesis committee is equally exceptional, and I thank Dr. Adam Feinberg and Dr. Lance Davidson for providing constructive criticisms and suggestions for new avenues I may otherwise have not explored.

Contributions of fellow lab members to this thesis are ubiquitous, and I am honored to share credit with Chia-Yuan Chen, Onur Dur, Prahlad Menon, Michael Patrick, Shephaly Soni, and Joe Tinney. I especially thank Nick Teslovich, who worked with me for nearly four years. His skill and effort were critical to the completion of this research.

The following funding sources contributed to the work presented in this thesis: Carnegie Mellon University Department of Biomedical Engineering, NSF CAREER Award 0954465, American Heart Association Beginning Grant in Aid 0765284U, Pittsburgh Supercomputing Center Grant CCR080013, and NIH T32 EB003392 Biomechanics in Regenerative Medicine.

Finally, I give my thanks to my family for their constant support. Their gestures of encouragement, big and little, were always appreciated.

Abstract

Congenital heart disease (CHD) has the highest incidence and mortality rate of all birth defects in the U.S., occurring in at least 8 of every 1000 live births, and accounting for more than 24% of birth defect related infant deaths. Clinical and experimental data indicate that the hemodynamic environment has a significant role in the etiology of CHD, motivating the development of fetal valvuloplasty to reverse the progression of heart defects *in utero*. The efficacy of this intervention relies heavily on understanding the biomechanical relationships between blood flow and cardiovascular growth and remodeling. This thesis describes several studies using the chick embryo model designed to quantify vascular morphogenesis *in vivo* and link the observed trends to hemodynamic forces such as wall shear stress (WSS). Morphogenesis of the embryonic aortic arches, a series of bilaterally paired vessels surrounding the foregut and the precursors to the great vessels, was investigated using fluorescent dye injection and optical coherence tomography imaging. These experimental results were combined with computational fluid dynamics models of flow through the aortic arches, which revealed a correlation between transitioning aortic arch patterns and acute increases in WSS. Additionally, a regression analysis found a strong polynomial relationship between luminal aortic arch growth and deviations in WSS. Transformations of the aortic arches were further investigated using a computational optimization-based growth model. The model demonstrated that selection of the adult single aortic arch was influenced by the rotation of the outflow tract of the heart. The principle of minimum work, combined with this model, accurately predicted the transformation to a single aortic arch configuration. In order to support predictive computational models, quantitative data of vascular growth is required. Morphogenesis of an embryonic vitelline artery was tracked using a time-lapse, long-term optical coherence tomography based imaging system. Global and

local growth of the artery was quantitatively analyzed at high spatial and temporal resolution. Finally, a model of hypoplastic left heart syndrome in the chick embryo was used to determine alterations in intracardiac flow patterns that may lead to the progression of this defect. Out of three venous injection sites, two shifted their flow pattern significantly. This change was observed soon after the intervention to generate the defect was performed, suggesting that flow disruption is an early insult leading to hypoplastic left heart syndrome. Together, these studies support the importance of the hemodynamic environment in determining vascular morphogenesis in the embryo. The combined experimental and computational approach provided new quantitative data of embryonic vascular morphogenesis. The results of these studies and the methods established in this thesis lay the foundation for future research on the biomechanics of cardiovascular development.

Table of Contents

List of Tables

List of Figures

List of Abbreviations

AA	aortic arch(es)
AV	atrioventricular
CHD	congenital heart disease
DA	dorsal aorta
ECM	extracellular matrix
HH	Hamburger-Hamilton
HLHS	hypoplastic left heart syndrome
ICFP	intracardiac flow patterns
LAL	left atrial ligation
LCCV	left common cardinal vein
LVV	left vitelline vein
micro-CT	micro computed tomography
MRM	magnetic resonance microscopy
NCC	neural crest cell(s)
OCT	optical coherence tomography
OT	outflow tract
OTB	outflow tract banding
PIV	particle image velocimetry
RCCV	right common cardinal vein
RVV	right vitelline vein
SEM	scanning electron microscopy
VVL	vitelline vein ligation
WSS	wall shear stress

Chapter 1

Introduction and review of previous work

The heart and vasculature is the first organ system to form and the only one which is required to function successfully throughout the embryonic and fetal life for survival (Burggren and Keller, 1998). It is also the organ system associated with the highest incidence and mortality of all birth defects as well as the highest morbidity and mortality rates in adults (Go et al., 2013). In the US, congenital heart disease (CHD) occurs in at least 8 of every 1000 live births and accounts for more than 24% of birth defect related infant deaths (Roger et al., 2011). Most children born with CHD represent either new genetic mutations or epigenetic insults that alter cardiac morphogenesis *in utero* and result in CHD. The past half-century has produced dramatic advances in the expertise and technologies available to diagnose, manage, and treat CHD, improving the survival rate to 90%. Comparable outstanding progress has been made over the past 25 years in defining the molecular and epigenetic mechanisms that regulate cardiovascular morphogenesis in a broad range of invertebrate and vertebrate species. Concurrent success in the adaptation of bioengineering principles including the visualization of regional blood flow, calculation of mechanical shear stress, and computational modeling of morphogenesis and disease complements the understanding of cardiovascular biology and improves clinical management. This work has enhanced our understanding of the relationships between hemodynamics and the growth and remodeling of the embryonic cardiovascular system and provides direct evidence that changes in biomechanical loading within the developing heart regulate cardiac structure and function dynamically throughout embryogenesis. This paradigm has been translated as a rationale for cardiac intervention in the mid-gestation human fetus and intervention in humans has shown that restoration toward normal biomechanical loading partially

restores the growth and remodeling of left heart structures (mitral valve, aortic valve, aorta), though recovery of fetal myocardial growth after fetal intervention remains suboptimal (McElhinney et al., 2010; Pekkan et al., 2008b; Pekkan et al., 2008c; Pekkan et al., 2008d; Wang et al., 2009). This thesis seeks to expand the knowledge of embryonic hemodynamics and morphogenesis to uncover quantitative principles relating biomechanical cues and cardiovascular growth.

1.1 Review of cardiovascular morphogenesis

Cardiovascular development is highly conserved among vertebrate species. These shared processes are a boon to developmental biologists and bioengineers who regularly employ a variety of animal models to study the formation of the heart and vasculature. Some of the more widely used vertebrate models are the zebrafish, frog, chick, and mouse (Al Naieb et al., 2012; Bruneau, 2008; Glickman and Yelon, 2002; Isogai et al., 2001; Levine et al., 2003; Lohr and Yost, 2000; Martinsen, 2005; Nieuwkoop and Faber, 1994; Savolainen et al., 2009). While the mature cardiovascular systems differ among these species, all share common morphological and structural events with human development, making them suitable for investigation. A timeline overview of selected events is given in Table 1. Each species has its own advantages and disadvantages. The variety of transgenic strains and high number of homologous genes with humans have made the mouse embryo the prominent model for the study of genetic perturbations, though its internal development hampers *in vivo* measurements (Bradshaw et al., 2009; Wang et al., 2006). The zebrafish is also used as a genetic model, though less homologous to humans, while its transparent body allows non-invasive *in vivo* measurements of hemodynamics and cardiac function (Corti et al., 2011; Hove et al., 2003). The large size of frog

embryos makes them well suited for gene manipulation by microinjection and the availability of molecular markers has enabled detailed cell fate-mapping (Lee and Saint-Jeannet, 2009; Warkman and Krieg, 2007). The chick embryo develops externally, remains immotile for much of its developmental cycle (unlike the zebrafish and frog), and is transparent and easily accessible, all of which have made it highly utilized for morphologic and hemodynamic measurements (le Noble et al., 2004; Poelma et al., 2010). In addition, the mature heart of the chicken has four fully septated chambers, closely resembling that of the human. The primary objective of this thesis is to further our understanding of external hemodynamic and biomechanical factors and their role in the growth and morphogenesis of the cardiovascular system. Given its over 100 year history in this field (Hughes, 1934; Kirby et al., 1983; Oosterbaan et al., 2009; Rychter, 1962; Thoma, 1893), as well as the advantages stated above, we have selected the chick embryo as our model organism (Figure 1). Developmental staging of the chick embryo was performed by Hamburger and Hamilton and is referred to as HH in the remainder of this thesis (Hamburger and Hamilton, 1951).

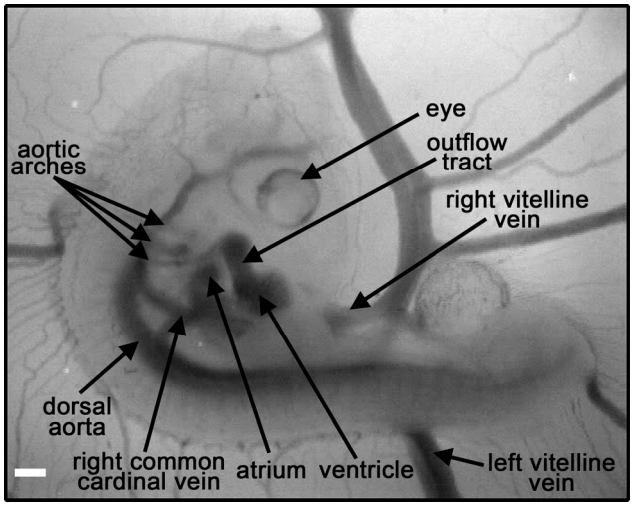

Figure 1. An HH21 chick embryo with relevant cardiovascular structures labeled. The embryo is viewed from a right lateral perspective. Scale bar is 250 μm.

Table 1. Comparative timeline of events in cardiovascular development.

	Zebrafish	Xenopus NF stages	Mouse	Chick HH stages	Human Streeter
gestation/incubation period			20 days	21 days	9 months
mature heart		46 (4.42d)	16d	36 (10d)	
linear heart tube	1d	32 (1.67d)	8d	9 (1.29d)	X (22d)
first heartbeat	1d	33 (1.83d)	8d	9 (1.29d)	X (22d)
blood flow begins	1d	33 (1.83d)	8.5d	10 (1.46d)	X (22d)
cardiac looping[1]	1-2d	32-40 (1.67-2.75d)	8-10.5d	10-24 (1.46-4d)	X-XVII (22-35d)
onset of ventricular trabeculation	2d	41 (3.17d)	9.5d	16 (2.23d)	XII (26d)
atrial septation	N/A	44-46 (3.83-4.42d)	10-14.5d	16-36 (2.23-10d)	XIV-XVI (29-33d)
ventricular septation	N/A	N/A	9-14d	17-34 (2.42-8d)	XIV (229d)
atrioventricular cushions form	2d	39 (2.33d)	10d	16 (2.23d)	XIII (28d)
outflow tract cushions form		39 (2.33d)	10d	19 (3.23d)	XV (31d)
first aortic arch[2]	1d	31-37 (1.54-2.21d)	9-10d	14-18 (2.13-3d)	X-XIII (22-28d)
second aortic arch[2]	1.5d	31-37 (1.54-2.21d)	9.5-10d	14-21 (2.13-3.5d)	XII-XIV (26-29d)
third aortic arch[2]	2d	32-46 (1.67-4.42d)	9.5-13d	15-34 (2.16-8d)	XIII-XVII (28-35d)
fourth aortic arch	2d	35 (2.08d)	10.5d	18 (3d)	XIII (28d)
fifth aortic arch	2.5d	35 (2.08d)		20-24 (3.33-4d)	
sixth aortic arch[2]	2.5d	40-41 (2.75-3.17d)	11-12.5d	21-46 (3.5-21d)	XIV-XVII (29-35d)
pulmonary arteries	N/A	41 (3.17d)	12d	22 (3.62d)	XIV (29d)

d – days post fertilization
[1]time interval encompasses dextral looping through mature s-loop
[2]time interval encompasses AA formation through degeneration or loss of connection with the descending aorta.

1.1.1 The heart

The heart and vasculature are formed from cells originating in the splanchnic mesoderm. Two laterally positioned groups of cells at the anterior region of the embryo form the primary heart

field, also referred to as the cardiogenic mesoderm and encompass the cellular origins of the atrial and ventricular structures (Rawles, 1943; Redkar et al., 2001). Cells within the primary heart field migrate anteriorly and toward the midline of the embryo while presumptive endocardial cells begin to delaminate and form a pair of bilateral endocardial tubes on either side of the primitive gut. These endocardial tubes are flanked by the myocardial precursor population of the primary heart field. As the foregut is formed by inward folding of the splanchnopleure, the cardiac tubes are brought together and eventually fuse at the ventral midline to form the primitive heart tube oriented along the cranio-caudal axis at HH9 (Martinsen, 2005). The heart tube does not fully close, however, until HH12.

Spontaneous action potentials propagate through the presumptive myocardium before the cardial tubes fuse and the myocytes become contractile (Kamino et al., 1981). The heart begins to contract and blood begins to flow a few hours after formation of the linear heart tube. The venous pole is located caudally and blood flows cranially through the atrium, ventricle, and exits at the arterial pole. The heart tube is initially composed of three layers: an inner endocardium, an outer two-cell layer of myocardium, and a thick cardiac jelly in between. The cardiac jelly is at first cell-free, consisting of an extracellular matrix (ECM), including hyaluronan, chondroitin sulfate, fibronectin, laminin, collagen, and various proteoglycans, secreted by the myocardium (Person et al., 2005). Through HH22, additional cell populations participate in elongation of the heart tube and further development of the heart structures (de la Cruz et al., 1977). Importantly, a secondary heart field located in the splanchnic mesoderm adjacent to the floor of the caudal pharynx adds to the arterial pole of the heart tube between HH14-22 (Waldo et al., 2001). These cells give rise to the outflow tract (OT) and smooth muscle at the base of the mature aorta and

pulmonary trunk, though the extent and contribution of the secondary heart field is not fully understood (Abu-Issa et al., 2004; Mjaatvedt et al., 2001).

Almost immediately after the linear heart tube forms, it begins the morphogenetic process of cardiac looping. A major consequence of cardiac looping is that it positions the presumptive heart chambers into their mature anatomical locations. The first phase, dextral looping, results in a ventral bend in the heart tube, which rotates to the right to form a C-shaped curve (Figure 2B) (Manner, 2000). As looping continues, the atrial region migrates dorsally and cranially while the ventricular region shifts ventrally and caudally, forming an immature S-loop (Figure 2C). This process continues until the atrium is positioned cranial and dorsal to the ventricle, resembling the mature anatomy, creating the mature S-loop at HH18 (Figure 2D) (Manner, 2000). From HH18-24, the OT migrates and rotates from a rightward location to its final position at the ventral midline of the heart (Manner, 2000). Throughout looping, the ventricular and atrial chambers are expanding, creating the appearance of a ballooning tube. Cardiac looping can be replicated on models of the heart tube by applying opposing torsions to the caudal and cranial ends (Manner, 2004). While asymmetric genetic expression has been indicated (Baker et al., 2008; Mercola and Levin, 2001), intrinsic and extrinsic forces are required for cardiac looping (Taber, 1998a; Voronov et al., 2004).

Occurring at the same time as looping, localized enhanced secretions of ECM components by myocardial cells generate regional expansions of the cardiac jelly, forming the endocardial cushions in the atrioventricular (AV) canal and OT (Markwald et al., 1977). The molecular events causing this localized secretion are still undetermined (Person et al., 2005). By HH17, endocardial cells begin to undergo epithelial-to-mesenchymal transition and invade the cushions, forming the cushion mesenchyme cell population (Kirby et al., 1983; Person et al.,

2005). In the OT, migrating neural crest cells (NCC) also invade the cushions (Kirby et al., 1983). The AV cushions form at the dorsal, ventral, right, and left boundaries, creating four distinct structures (Butcher and Markwald, 2007). The dorsal and ventral cushions fuse at the midline of the AV canal by HH25, dividing the right and left AV canals (Butcher and Markwald, 2007). The left and right lateral AV cushions form the mural leaflets of the mitral and tricuspid valves, respectively. The ventral cushion forms the portion of the anterior mitral valve leaflet associated with mitral-aortic continuity while the dorsal cushion forms the basal portion of the anterior mitral valve leaflet and the septal leaflet of the tricuspid valve (de la Cruz and Markwald, 2000). Remodeling of the AV cushions to the structured valve leaflets occurs through HH28-36 (Martinsen, 2005).

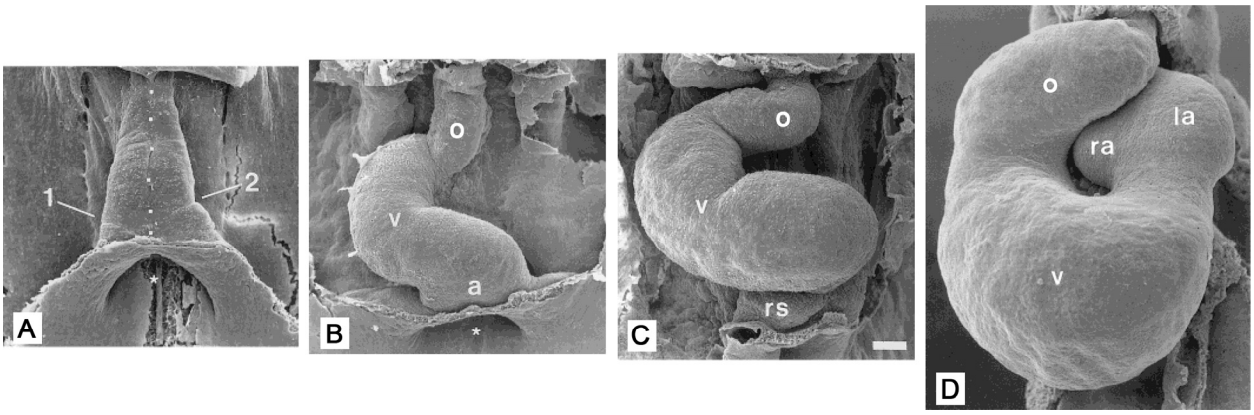

Figure 2. Ventral views of phases in cardiac looping. A) The linear heart tube (HH9); the right (1) and left (2) lateral furrows and anterior intestinal portal (asterisk) are labeled. The dotted line gives the ventral midline of the tube. B) Completion of dextral looping (HH12). C) Formation of the immature S-loop (HH14). D) The mature S-loop (HH18). a – atrium, v – ventricle, o – outflow tract, la – left atrium, ra – right atrium, rs – right horn of sinus venosus. Scale bar is 100 μm. Adapted from (Manner, 2000).

A total of 5 cushions form in the OT of the embryonic chick heart, which are divided into proximal (conal) and distal (truncal) regions, demarcated by the dog-leg bend of the OT (Qayyum et al., 2001). Two proximal cushions, right and left proximal, fuse to form an intracardiac septum, while three distal cushions, distal dorsal, distal right and left ventral, form the leaflets of the arterial valves and the walls of their supporting sinuses (Qayyum et al., 2001). The aortopulmonary septum, a horseshoe-shaped outgrowth of the pharyngeal mesenchyme, grows toward the distal OT at HH25, fusing with the distal cushions at HH27 to septate the aortic sac (Qayyum et al., 2001). As the cushions and aortopulmonary septum fuse, they form a spiral septum within the OT. A pair of distal intercalated cushions form at HH29 and constitute the remaining valvulogenic structures (Qayyum et al., 2001). As the aortopulmonary septum elongates, it separates the distal dorsal cushion into a right and left half. Thus, the three leaflets of the aortic valve are formed by the right portion of the distal dorsal cushion, the distal right ventral cushion and the right intercalated cushion while the leaflets of the pulmonary valve are formed by the left-sided counterparts (Qayyum et al., 2001). Formation of the semilunar valve leaflets and sinuses requires cavitation of the distal cushions (beginning at HH30), after which the luminal component elongates to form a valve leaflet while the mural component differentiates into the walls of the sinus. Stratification of the ECM to form the characteristic leaflet structure occurs later from HH42 through hatching (Hinton et al., 2006; Tan et al., 2011).

Ventricular trabeculation begins at HH16, and the forming trabeculae constitute the majority of myocardial mass increases through HH21 (Sedmera et al., 2000). The compact myocardium undergoes a highly proliferate phase from HH34-40 (Sedmera et al., 2000). Ventricular septation occurs as major trabecular bundles expand and fuse with the endocardial cushions and is completed by HH34 (Martinsen, 2005). Atrial septation occurs due to the

growth of mesenchymal tissue toward the AV cushions and is completed by HH36, although the foramen ovale maintains a right to left communication until hatching (Martinsen, 2005). As the OT is undergoing septation, its outer myocardial layer is retreating proximally via apoptosis, reducing by 67% in length between HH27-32, becoming a compact ring at the level of the pulmonic infundibulum (Watanabe et al., 1998; Watanabe et al., 2001). Extracardiac space begins to form to separate the aorta and pulmonary artery trunks. The smooth muscle of the media begins to form at HH27, with elastin and collagen matrix production following soon after (Bergwerff et al., 1996; Qayyum et al., 2001; Waldo et al., 2005b). Cellular events that occur during this rapid arterialization are not known, and the source of the smooth muscle cells is disputed (Anderson et al., 2003; Okamoto et al., 2010; Sanchez Gomez et al., 2005; Ya et al., 1998). These septation events create the mature, four-chambered heart with aortic and pulmonary outlets by HH36.

1.1.2 The arterial and venous poles

As the primary heart field arose in the anterior mesoderm, cells in the posterior region give rise to hemangioblasts, the precursors to blood and blood vessels, which create networks of intraembryonic and extraembryonic blood vessels through vasculogenesis. Hemangioblasts condense into aggregations called blood islands, which coalesce into solid cords and interconnect to form a seamless vascular network. Lumens form through cord-hollowing as the outer angioblasts differentiate into endothelial cells and the inner cells become blood (Strilic et al., 2009; Strilic et al., 2010). Further remodeling of these networks takes place through angiogenesis, while arterial and venous differentiation is largely due to inherent genetic expression (le Noble et al., 2008; Othman-Hassan et al., 2001).

The first intraembryonic vessel to emerge is the dorsal aorta (DA), the major artery of the chick embryo, derived from migrating angioblasts originating in the somatic mesoderm (Strilic et al., 2009). Bilaterally symmetric left and right cranial aortae fuse at the mid-level of the embryo to form the single DA. Connecting the cranial aortae to the OT initially is the first aortic arch (AA), a bilateral pair of vessels that run medially through the first pharyngeal arch, surrounding the anterior foregut (Hiruma and Hirakow, 1995). As pharyngeal arches emerge in a cranial-caudal fashion, each receives its own AA vessel, totaling six AA pairs, numbered I-VI. AA formation proceeds through both vasculogenic and angiogenic mechanisms; angioblasts derived from the pharyngeal mesenchyme arise *de novo* and are linked to the cranial aortae and aortic sac through angiogenesis (Anderson et al., 2008; Coffin and Poole, 1988; DeRuiter et al., 1993). The endothelial lumens are ensheathed by ectomesenchyme derived from NCC, which stabilize the AA and are the source of smooth muscle and non muscular cells of the vessel wall (Waldo et al., 2005a; Waldo et al., 1996). AA I and II are populated by pre-otic NCC, while AA III-VI are associated with NCC from the region between the mid-otic placode and the caudal limit of somite three, the so-called "cardiac neural crest" (Kuratani and Kirby, 1991).

Though six AA pairs emerge during development, three pairs generally co-exist at early embryonic time points and the symmetric AA pairs are selectively reduced and remodeled into the mature asymmetric aortic arch and pulmonary arteries by HH36 (Hiruma and Hirakow, 1995; Kardong, 2009). Only three of the six AA pairs persist (III, IV, VI). Cranial-most AA I and II remodel into capillary beds and AA V exists only as a transient segment of AA VI (Hiruma and Hirakow, 1995). AA III forms portions of the brachiocephalic and common carotid arteries. The right lateral AA IV forms a segment of the transverse adult aortic arch while the left lateral AA IV regresses. This asymmetric AA IV pattern is different in mammals: the left lateral AA IV

contributes to the adult aortic arch and the right lateral AA IV forms a short segment of the proximal right subclavian artery. The caudal-most AA VI contributes to segments of the central pulmonary arteries and ductus arteriosus. Bilateral regression of the carotid ducts (cranial aortae between AA III and IV, also called the γ-segment), and unilateral regression of the α- and β-segments of the left cranial aorta (portions between the subclavian artery and descending dorsal aorta and AA IV and the subclavian, respectively) completes the right sided aortic arch pattern of the mature chicken (Hiruma and Hirakow, 1995; Molin et al., 2002). These events are summarized in Figure 3.

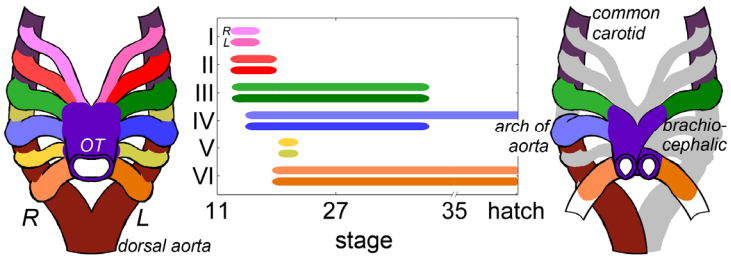

Figure 3. Timeline and schematic of the AA derivatives in the chick embryo. The timeline depicts the duration of the connection between the heart and descending DA, where line width is an approximation of the frequency that the AA is present. The time axis is skewed to highlight the early stages investigated in this thesis. Though AA V is included here, it never truly connects to the DA. The schematic on the left represents the six embryonic AA pairs. The schematic on the right depicts the mature avian great vessel pattern, where gray represents embryonic AA sections that disappear prior to the final configuration.

NCC within the AA begin to express α-smooth muscle actin as early as HH18, suggesting the onset of differentiation (Bergwerff et al., 1996; Bergwerff et al., 1998). The mesenchymal source of the smooth muscle of the dorsal aorta is mesodermal in origin and begins to differentiate at about the same time (Bergwerff et al., 1996). Additional cell layers are added

and deposition of matrix components such as elastin (HH31) and collagen (HH42) separate cell layers and create a lamellar pattern of actin expression and appearance of adventitial fibroblasts, though the timeline is not the same for all AA (Bergwerff et al., 1996; Bergwerff et al., 1998; Hughes, 1943). There are notable differences in the histogenesis of AA pairs, including a discontinuity in actin expression at the distal region of AA IV (Bergwerff et al., 1999) and a lower number of and thicker cell layers in AA VI (Bergwerff et al., 1996). In addition, asymmetric vascular apoptosis patterns result in the normal regression of AA and DA segments such as the carotid ducts (Molin et al., 2002). Though the regression mechanism for AA is still undefined, these apoptosis patterns suggest that it may be similar to capillary remodeling and occlusion of the ductus arteriosus during postnatal life (Echtler et al., 2010; Meeson et al., 1996). Apoptosis followed by delamination of endothelial cells into the lumen occludes blood flow, leading to further cell death.

Blood islands within the yolk sac form the extensive extraembryonic vitelline network, which bring nutrients to the embryo. The right and left vitelline veins (RVV, LVV) drain this extensive network and connect directly to the heart, forming the atrial inflow (van den Berg and Moorman, 2011). These vessels fuse in a cranial to caudal fashion to become the portal vein. The major intraembryonic veins are the bilaterally symmetric anterior and posterior cardinal veins, which join to form the right and left common cardinal veins (RCCV, LCCV) (Rosenquist, 1971a). Veins draining the allantois, the external gas exchange organ of the chick embryo, connect directly to the RCCV and LCCV, which then join the RVV and LVV at the level of the heart to form the common mouth of the systemic veins. At HH14, this venous pole is bilaterally symmetric and the inflow is centered within the common atrium (Manner and Merkel, 2007). By HH21, however, due to a rightward shift of the common mouth and the onset of atrial septation,

the systemic venous blood empties solely into the right portion of the atrial inflow (Manner and Merkel, 2007). This shift concurrently results in elongation of the LCCV, creating the asymmetric venous pole. At HH21, the pulmonary veins begin to form from the splanchnic mesoderm overlying the foregut and drain into the left portion of the atrial inflow (Rosenquist, 1971b; van den Berg and Moorman, 2011). By HH25, a discrete systemic venous sinus is observed, with both the RCCV and LCCV covered by myocardium (van den Berg and Moorman, 2011). The left anterior cardinal vein eventually joins the RCCV by formation of the left brachiocephalic venous trunk. The LCCV persists only as a portion of the coronary sinus venosus while the RCCV forms the superior vena cava in the mature chicken (Liem et al., 2001). A portion of the RVV persists as a short, distal segment of the inferior vena cava while the LVV and posterior cardinal veins largely regress over the course of later development.

Abnormalities associated with the AA are present in over 20% of congenital heart disease, with the most common being patent ductus arteriosus and coarctation of the aorta (Go et al., 2013). Double aortic arch, caused by persistence of both AA IV laterals, and right aortic arch, occurring when the dominant arch of aorta forms from the right lateral of AA IV, results in a vascular ring compressing the trachea and esophagus, causing upper airway obstruction and dysphagia (Backer and Mavroudis, 1997). Interrupted aortic arch is induced by unilateral obliteration of the left AA IV in left arch dominant aortas, is often associated with loss of the right AA IV resulting in an aberrant origin of the right subclavian artery, and is always associated with a ventricular septal defect, in which blood from both ventricles flow through the pulmonary artery and is shunted to the systemic circulation through a patent ductus arteriosus (Sadler and Langman, 2006). Defects of the venous connections are less common and can

include a left or double superior vena cava, abnormal pulmonary vein connections, and double inferior vena cava at the lumbar region (Sadler and Langman, 2006).

1.2 Hemodynamics of cardiovascular development

1.2.1 Hemodynamic trends during embryonic development

Early studies of the embryonic heart suggested that peristalsis drives blood flow, in which a unidirectional contractile wave travels from atrium to ventricle to outflow tract (Barry, 1942; Patten and Kramer, 1933). This mechanism was used to explain the persistence of forward flow in the absence of valves, i.e. valveless pumping. However, aspects of embryonic blood flow, such as its pulsatile waveform, are not consistent with peristaltic pumps (Forouhar et al., 2006; Manner et al., 2010). Studies performed using zebrafish embryos suggested a different form of pumping consistent with Liebau pumps (Forouhar et al., 2006). Liebau pumps achieve unidirectional flow by compression of a single point asymmetrically located between two sites of mismatched impedance (Liebau, 1957). While there is still debate over how the valveless heart propels blood flow, one possible explanation is a combination of both mechanisms; a Liebau pump with multiple compression sites that act in sequence (Manner et al., 2010). Additionally, the presence of endocardial cushions may generate pulsatile flow even under peristaltic pumping conditions (Taber et al., 2007).

Experimental measurements of hemodynamics at various developmental stages have been performed by numerous researchers. Cardiac output and heart rate are traditionally measured at the DA using pulsed-Doppler ultrasound (Broekhuizen et al., 1999; Broekhuizen et al., 1993; Clark and Hu, 1982; Hu and Clark, 1989; Lucitti et al., 2005; Lucitti et al., 2006; Ursem et al., 2001; Yoshigi et al., 2000). However, new techniques such as particle image

velocimetry (PIV) and Doppler optical coherence tomography (OCT) have been used to obtain flow velocity measurements directly at the OT and obtain comparable results (Ma et al., 2010; Poelma et al., 2010). Heart rate varies between independent studies, which may be due to temperature differences or experimental technique. However, a general linearly increasing trend is found with respect to developmental stage (Figure 4B). Cardiac output, however, increases exponentially over development, which suggests a similar exponential trend in stroke volume given the linear increase in heart rate (Figure 4A). Normalized to body weight, cardiac output remains constant while stroke volume decreases slightly from HH12-29 (Hu and Clark, 1989). Blood pressure is measured using a servo-null system (Clark et al., 1986; Hu and Clark, 1989; Keller et al., 1991). Studies in the chick embryo demonstrate that ventricular blood pressure increases exponentially during development, though peak systolic pressures increase at a faster rate than end diastolic pressures (Figure 4C) (Clark et al., 1986; Hu and Clark, 1989). Stroke work and total cardiac power both increase exponentially, while total vascular resistance and characteristic impedance decrease exponentially, though impedance at a slower rate (Hu and Clark, 1989; Lucitti et al., 2005). Together, these measurements demonstrate the rapidly changing hemodynamic environment during cardiovascular growth and morphogenesis.

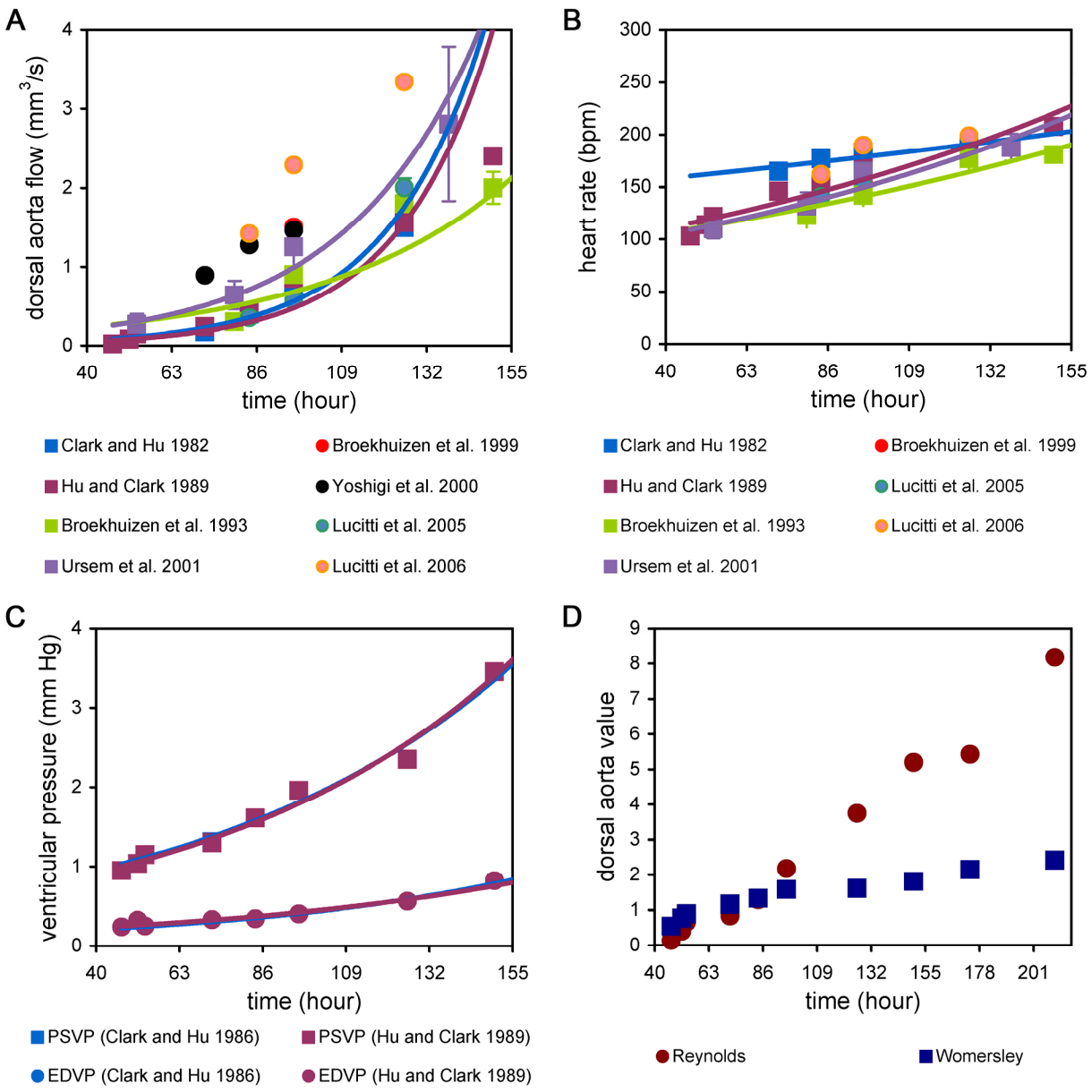

Figure 4. Hemodynamic trends during chick embryo development. A) Cardiac output increases exponentially with developmental stage. B) Heart rate varies among independent studies, but generally increases linearly over development. C) End diastolic and peak systolic ventricular pressures (EDVP, PSVP) increase exponentially. D) Reynolds and Womersley numbers in the DA. Flow and diameter data are based on (Broekhuizen et al., 1993; Hu and Clark, 1989) and viscosity is taken from (Al-Roubaie et al., 2011). Blood density is assumed to be 1025 kg/m^3.

Blood flow within the embryonic cardiovascular system is laminar and quasi-steady, indicated by low Reynolds (Re) and Womersley (Wo) numbers (Figure 4D). In the chick embryo DA, Re and Wo range between 0.1-9 and 0.5-3, respectively, between HH12-36, compared to values of Re 1000 and Wo 40 in the mature human aorta. The low Wo values indicate that velocity profiles are parabolic and quasi-steady, which has been demonstrated through PIV analysis of the HH18 vitelline vessels (Poelma et al., 2008). Computing Re and Wo numbers requires blood viscosity, which can differ significantly between embryonic and mature blood. In mature mammals, blood exhibits non-Newtonian behavior, in which the apparent viscosity decreases nonlinearly with increasing shear rates (Fung, 1997). This non-Newtonian rheology is primarily due to the presence of red blood cells, which are biconcave and deformable. Embryonic red blood cells, however, are spherical and make up a smaller percentage of the blood volume (Rychter et al., 1955). Rheological studies of HH24-34 chick embryonic blood revealed that hematocrit increases linearly, however the embryonic blood behaved as a Newtonian fluid throughout the investigated stages (Al-Roubaie et al., 2011). Hematocrit was also shown to be a good predictor of blood viscosity in the chick embryo.

1.2.2 Hemodynamics as an environmental factor

As blood flows through the vascular system, it exerts a normal force due to pressure, circumferential stress due to vessel deformation under pressure, and a tangential wall shear stress (WSS). These forces deform the vascular wall and in particular the endothelial cells, which respond by transducing biochemical signals leading to morphological and structural changes (Chien, 2007). Vascular adaptation in response to blood flow, or the "flow dependency principle" has long been established in the mature cardiovascular system (Kamiya and Togawa, 1980). Increased transmural stress due to hypertension elicits a remodeling response including

wall thickening, increased smooth muscle proliferation, and increased collagen production and turnover (Fung and Liu, 1991; Intengan et al., 1999a; Intengan et al., 1999b; Nissen et al., 1978; Olivetti et al., 1980; Tedgui et al., 1992). These effects act to return wall stress to normal values (Fung and Liu, 1991). Although the molecular mechanisms are not fully known, experiments demonstrate that matrix metalloproteinases have a key role (Asanuma et al., 2003; Grote et al., 2003; Jackson et al., 2002). Experiments in a variety of species to alter blood flow within vessels demonstrate that increased flow results in increased diameter and decreased flow results in decreased diameter or vessel regression (Bayer et al., 1999; Girerd et al., 1996; Gruionu et al., 2005; Guyton and Hartley, 1985; Kamiya and Togawa, 1980; Langille and O'Donnell, 1986). This growth response returns WSS to levels prior to the flow alteration and is endothelium dependent (Kamiya and Togawa, 1980; Langille and O'Donnell, 1986). These studies provide ample evidence that hemodynamic forces such as pressure and WSS are critical environmental factors determining vascular morphology and the mechanosensitive endothelium is the primary mechanism for transducing these biomechanical cues into biochemical signals that regulate vascular adaptation events (Lehoux et al., 2006).

The role of hemodynamics is also present in the embryo, where the mechanical forces of blood flow are significant in the growth, morphogenesis, and remodeling of the cardiovascular system (Culver and Dickinson, 2010). Indeed, the earliest studies of relationships between hemodynamics and vascular morphology were performed on the vitelline network of the chick embryo (Thoma, 1893). Several earlier works tracked intracardiac blood flow patterns, theorizing that the paths of multiple streams determined cardiac septation (Bremer, 1932; Jaffee, 1965; Jaffee, 1967), though these conclusions were later contradicted (Yoshida et al., 1983). Currently, the environmental, biomechanical role of hemodynamics has been demonstrated at

nearly every stage of cardiovascular development, including cardiac looping (Broekhuizen et al., 1999), valve formation (Hogers et al., 1999; Vermot et al., 2009; Yalcin et al., 2011), ventricular trabeculation and myocardial remodeling (Sedmera et al., 2002; Sedmera et al., 1999; Tobita et al., 2005), septation (Hogers et al., 1999), development of the cardiac conduction system (Reckova et al., 2003), morphogenesis of the AA (Corti et al., 2011; Hogers et al., 1999; Hu et al., 2009; Rychter and Lemez, 1965), arterial remodeling (Lucitti et al., 2005), and arterial-venous differentiation (le Noble et al., 2004).

Several mechanical interventions are applied in the chick embryo to perturb blood flow and study the morphological, structural, and genetic effects. Three widely used models are vitelline vein ligation (VVL), left atrial ligation (LAL), and outflow tract banding (OTB). VVL modifies the venous network by ligating or clipping the RVV or LVV to occlude blood flow and results in an acute reduction in preload, redirected intracardiac and AA flow patterns, and altered gene expression (Groenendijk et al., 2004; Hogers et al., 1999; Stekelenburg-de Vos et al., 2003). Exclusion of the presumptive left atrium in LAL embryos results in reduced LV filling with compensatory increased RV filling and creates a phenotype reminiscent of hypoplastic left heart syndrome in humans (Sedmera et al., 1999; Tobita et al., 2005). OTB produces chronic increased ventricular afterload and altered OT velocity by tying a suture around the midpoint of the OT, reducing its cross-section and results in a thicker compact myocardium (Keller et al., 1997; Miller et al., 2003; Sedmera et al., 1999). The consequences of these, as well as other, interventions are discussed in detail throughout this thesis, as relevant to the subsequent chapters.

While both pressure and WSS impact embryonic cardiovascular morphogenesis, WSS has been the focus of most studies as it can be chronically altered by the surgical interventions mentioned above. Pressure, however, returns to normal values quickly after interventions,

seemingly at the sacrifice of flow (Lucitti et al., 2005), and is therefore harder to manipulate long-term. Understanding the mechanosensation and mechanotransduction of WSS to generate biochemical activity related to vascular growth and remodeling remains elusive. Multiple high throughput gene array studies on endothelial cells from the human aorta and umbilical vein have demonstrated laminar WSS regulates hundreds of endothelial genes and that under chronic WSS more genes are suppressed than induced (Brooks et al., 2002; Chen et al., 2001; McCormick et al., 2001). *In vitro* tests show that endothelial cells can sense WSS levels as low as 0.02 Pa (Olesen et al., 1988). How these studies translate to the embryo is currently unknown. Proposed mechanisms for mechanosensation include the endothelial cell glycocalyx (Nikmanesh et al., 2012), cell-cell adhesions (Tzima et al., 2005), ion channels (Olesen et al., 1988), and primary cilia (Egorova et al., 2011a; Van der Heiden et al., 2006). Many studies related to endothelial mechanosensation are performed *in vitro* using mature cells, necessitating additional research to uncover the full *in vivo* endothelial response to hemodynamic forces. A wide variety of studies have identified genes, proteins, and signaling molecules involved in WSS sensing in the embryo, which have been recently reviewed (Roman and Pekkan, 2012). These studies are referred to throughout the remainder of this thesis.

1.3 Modeling blood flow in the embryo

Understanding the relationships between hemodynamic forces and vascular growth requires quantitative knowledge of these forces. Doppler ultrasound techniques are useful for measuring flow velocity, but only produce a 1D velocity component parallel to the scanning direction, and velocity profiles must be estimated (Zheng et al., 2006). Doppler-OCT also gives a 1D velocity component, but has a greater spatial resolution than Doppler ultrasound. Combining Doppler-

OCT with 3D reconstructions of structural OCT data can produce 3D velocity profiles (Davis et al., 2009; Ma et al., 2010). The OCT imaging depth is limited to about 1 mm in the chick embryo and is therefore not applicable to intraembryonic vessels after HH21. This technique requires anatomical 3D reconstructions and gating algorithms to account for cardiac contractions and flow pulsatility. The maximum velocities measured with Doppler-OCT are limited by the scanning frequency of the OCT system, however phase unwrapping algorithms can be used to correct for slower scan rates (Davis et al., 2009). PIV techniques have the advantage of obtaining spatially resolved velocity vectors (Vennemann et al., 2006). PIV relies on high-speed imaging to track flow markers, which can be either seeded particles or the red blood cells (Poelma et al., 2012), and measurable velocities are therefore limited by the imaging speed. The ability to measure velocities of intraembryonic vessels is dependent on tissue transparency and PIV is normally performed prior to HH18. Techniques such as Doppler-OCT and PIV that provide velocity profiles can be used to compute WSS based on the velocity derivative at the vessel wall. This method is commonly used for experimental measurements of WSS, and results of several studies performed in the chick embryo are provided in Table 2 (Poelma et al., 2010; Poelma et al., 2008; Rugonyi et al., 2008).

To overcome the limitations discussed above, computational models of blood flow in the embryonic heart and vasculature are commonly used. These models range from simple 2D representations of the cardiac chambers (Santhanakrishnan et al., 2009) to pulsatile 3D models of flow that incorporate wall motion (Liu et al., 2011). Model geometries can be idealized, but most are reconstructed from imaging data. Advances in imaging techniques such as serial tissue sections (DeGroff et al., 2003), micro computed tomography (micro-CT) (Henning et al., 2011), and magnetic resonance microscopy (Smith et al., 1992) have made it possible to obtain high-

resolution 3D geometries of the embryonic chick cardiovascular system. However, these techniques apply fixation methods that can distort the morphology and cannot capture the wall motion of the beating heart. *In vivo* micro-CT is possible, but scan rates may be insufficient for the beating embryonic heart (Henning et al., 2011). OCT is a non-invasive imaging modality with sufficient spatial and temporal resolution for *in vivo* imaging of the chick heart (Yelbuz et al., 2002). Cardiovascular geometries are combined with experimentally determined boundary conditions such as velocity, pressure, and flow distributions to generate computational fluid dynamics (CFD) models of hemodynamics. Such models have been used to examine flow at the AV canal (Yalcin et al., 2011), OT (Bharadwaj et al., 2012; Liu et al., 2012), and AA (Wang et al., 2009). Hemodynamic parameters such as WSS can then be derived from the CFD solution to obtain biomechanical loading information; several example values are given in Table 2. Other computational models investigate structural mechanics of the developing heart, revealing stresses and strains within the embryonic ventricle (Buffinton et al., 2013). While pulsatile flow models, moving wall models of the OT, and structural models of the ventricle exist, a complete fluid-structure-interaction model of the beating embryonic heart has not been achieved. Information such as ventricular material properties, myocardial fiber angles, and complete 4D reconstructions of the heart are lacking in this endeavor.

Computational models have also been developed to predict cardiovascular growth in response to hemodynamic loading. These models have been primarily performed in adult, diseased states (Figueroa et al., 2009; Watton et al., 2009). Growth models have been proposed for the embryonic heart (Lin and Taber, 1995; Taber and Chabert, 2002) and aorta (Taber and Eggers, 1996; Wagenseil, 2010), but remain simplistic and confounded by a paucity of data on the microstructure and mechanical properties of the embryonic cardiovascular system. Perhaps

more limiting, however, is the lack of temporal data such as growth rates and coupled quantitative hemodynamic and morphologic data. Without this information, it is difficult to formulate the fundamental principles driving these models and nearly impossible to train them for accurate predictions. Enhanced quantitative data will enable predictive computational frameworks to test new theories of hemodynamic and morphologic relationships and possibly serve as a tool for surgical planning of fetal interventions. Incorporation of molecular models could further lead to novel treatment strategies for CHD.

Table 2. Velocity and WSS measurements at various locations in the chick embryo.

location	stage	velocity (mm/s)	peak WSS (Pa)	technique	reference
AV canal	HH17	40	1.93	CFD	(Yalcin et al., 2011)
	HH23	120	7.83		
	HH27	450	25.01		
	HH30	600	28.72		
AA	HH18	12	5.47	CFD	(Wang et al., 2009)
	HH24	19	9.56		
OT	HH16	78	1.82	CFD	(Bharadwaj et al., 2012)
	HH23	200	5.82		
	HH27	550	23.61		
	HH30	600	53.61		
OT	HH18	80	6.00	CFD	(Liu et al., 2012)
OT	HH17	-	3.20	PIV	(Poelma et al., 2010)
OT	HH18	78	-	Doppler-OCT	(Rugonyi et al., 2008)
ventricle	HH15	26	5.00	PIV	(Vennemann et al., 2006)
vitelline	HH18	0.8	0.3	PIV	(Poelma et al., 2008)

1.4 Thesis outline

This thesis is dedicated to quantifying morphogenesis in the early chick embryo and defining relationships that link events in cardiovascular development to changes in blood flow. We apply a multimodal bioengineering approach that combines non-invasive high resolution imaging with computational modeling to obtain *in vivo* data and test biomechanically-motivated principles of

cardiovascular growth. Chapter 2 investigates AA growth and blood flow at a key transitional stage in AA patterning and shows that hemodynamic loading plays an important role in the timing and progression of this process. Chapter 3 continues the examination of the AA, focusing on morphogenesis and selection. We apply a predictive computational framework to demonstrate that an optimization principle may explain species-specific AA patterns and AA defects in humans. Chapter 4 describes a novel technique for long-term imaging of the chick embryo and the quantification of global and local growth of a vitelline artery. Chapter 5 considers the role of blood flow in hypoplastic left heart syndrome and applies the chick LAL model to measure alterations in intracardiac flow patterns. We also develop an *in silico* CFD model of LAL to investigate changes in hemodynamic loading. Finally, Chapter 6 provides overall conclusions and future directions for this work.

Chapter 2

Critical transitions in early embryonic aortic arch patterning and hemodynamics

2.1 Introduction

Unlike the adult circulation, where the right and left ventricles eject through semilunar valves into the pulmonary and systemic arterial circulations, respectively, the embryonic ventricle ejects blood through multiple, bilaterally paired aortic arches (AA). In the chick embryo, six symmetric AA pairs emerge and are selectively remodeled to form the asymmetric right-sided arch of aorta as described in Chapter 1 (§1.1.2, Figure 3)**.** The AA transformation patterns were initially described through India ink injection and serial section experiments in the chick embryo (Hughes, 1934; Kastschenko, 1887; Pexieder, 1969; Sabin, 1917). The first complete 3D analysis of AA morphogenesis used corrosion casts and scanning electron microscopy to generate detailed morphology from chick embryo HH12 to hatching, providing a contemporary timeline of AA development (Figure 3) (Hiruma and Hirakow, 1995). Advances in imaging technology, including micro-computed tomography (micro-CT) (Henning et al., 2011), magnetic resonance microscopy (MRM) (Smith et al., 1992), and optical coherence tomography (OCT) (Yelbuz et al., 2002) now support comprehensive high-resolution studies of the 3D morphology of chick embryonic vasculature. Despite these advances, work related to AA morphogenesis has been predominantly descriptive and a lack of morphometric data persists. Studies that report measures of AA diameter often apply dehydration and fixation methods prior to acquiring measurements, which can distort vascular geometry (Pexieder, 1969; Stewart et al., 1986).

Several studies have demonstrated a relationship between hemodynamics and the global (organ scale) growth of the AA, where epigenetic perturbations in blood flow lead to congenital defects affecting the great vessels (Hogers et al., 1999; Hu et al., 2009; Rychter, 1962; Rychter and Lemez, 1965). While these studies provide evidence for the role of hemodynamics in AA growth and remodeling, limited quantitative spatial and temporal data on AA morphometry and flow have been available for biologists and bioengineers. In our previous work (Wang et al., 2009), we quantified changes in AA geometry, blood flow, and wall shear stress (WSS) between HH18 and 24 in the chick embryo (3 and 4 days, respectively). Our *in vivo* measurements demonstrated that both AA III reduce in diameter while both AA IV increase in diameter. Using composite three dimensional (3D) AA models reconstructed from micro-CT scanning, we conducted stage-specific computational fluid dynamics (CFD) simulations to quantify AA blood flow and spatial variations in WSS. The results revealed a significant shift in the distribution of cardiac output to the individual AA; in particular, the AA that received the largest amount of flow changed from AA III at HH18 to AA IV at HH24. WSS values in the AA increased from HH18 to 24, with the largest increase occurring in AA IV. This change in WSS was correlated with the enlargement of AA IV diameter, providing the first quantitative evidence for flow-dependent growth in the embryonic AA.

Our previous study also demonstrated that during the 24 hour period between HH18 and 24, cranial AA II degenerates to a capillary bed and the caudal-most AA VI emerges. AA II, III, and IV were present in all HH18 embryos while AA III, IV, and VI were present in all HH24 embryos. While this stage-specific lack of inter-embryo variation in AA configuration seems to indicate a controlled developmental process, there have been no investigations of the intermediate stages to determine how this transition occurs. Should the intermediate stages

present with uniform AA configurations, then it is possible that this transition is a tightly controlled and prescribed developmental program regulated by inherent temporal genetic activation. However, significant intra-stage variations in AA architectures would support the alternate hypothesis that epigenetic and environmental factors such as fluctuations in AA hemodynamics could be involved in determining final AA fates.

In the current study, we investigated the transitional HH21 (3.5 days), applying the multimodal 3D quantitative approach established in our previous work. *In vivo* imaging of HH21 AA was performed using fluorescent dye microinjections and OCT to acquire quantitative structural data without disrupting the morphology of the embryo. Representative 3D models of the HH21 AA were reconstructed from micro-CT scans and used for CFD analysis. We demonstrate that multiple AA configurations exist in "normal" HH21 embryos, suggesting a possible vulnerable window in the transition in AA configuration from HH18 to 24. CFD analyses indicate that variations in cardiac output distribution may be a critical factor in AA growth and selection by disrupting the timing of events such as AA regression, generation, and asymmetric growth. Thus, defining critical windows of developmental plasticity and the role of epigenetic, environmental factors that impact these developmental trajectories will help identify the origins of cardiovascular malformations and provide insights into the optimal timing for fetal intervention strategies to restore normal biomechanical loading. (McElhinney et al., 2010).

2.2 Methods

2.2.1 *In vivo* aortic arch diameter measurement

Fertilized white Leghorn chick eggs were incubated at 37°C and 60-70% relative humidity to HH21 (3.5 days). We windowed the shell and removed the overlying membranes to expose the

embryo and gain optical access. Using our fluid microinjection technique, we injected embryos with approximately 0.5 μl of Rhodamine B diluted in PBS (Mujumdar et al., 1993). We recorded time-lapse movies of each injection and extracted still frames for further analysis. The left and right lateral AA were identified using anatomical landmarks and AA midpoint diameters were then measured (Figure 5). A total of three measurements were made on each vessel and then averaged to obtain the midpoint diameter. AA identity and diameter measurements were performed by three independent observers, and inter-observer agreement was assessed using Bland-Altman analysis (Bland and Altman, 1986). A total of 32 right-lateral and 18 left-lateral HH21 embryos were injected and analyzed.

Dye injection data was confirmed using a spectral domain OCT (SDOCT) system (Thorlabs Spectral Domain Ganymede, Thorlabs, Inc., NJ) to acquire noninvasive, *in vivo* images of the right and left lateral AA (4.3 μm resolution). OCT is an echo-based modality, which uses low-coherence interferometry to measure the axial distance of back-reflected light (Huang et al., 1991). We have previously applied and validated our OCT system in the development of a novel velocimetry technique for live embryos (Chen et al., 2012). Details of our OCT system are given in Chapter 4 of this thesis. Briefly, the axial resolution was 5.8 μm in air and 4.3 μm in water and the lateral resolution was 15 μm. The maximum A-scan rate of our OCT system was 29 kHz (equivalent to 38.3 fps for 757 A-lines per frame). The rate of data transfer and live streaming of the 2D OCT scan produced an actual recorded frame rate of 17.1 fps for a 757 A-line image (12.9 kHz). The sample refractive index is defined for the medium surrounding the sample and was considered 1.33 for *in ovo* embryo imaging.

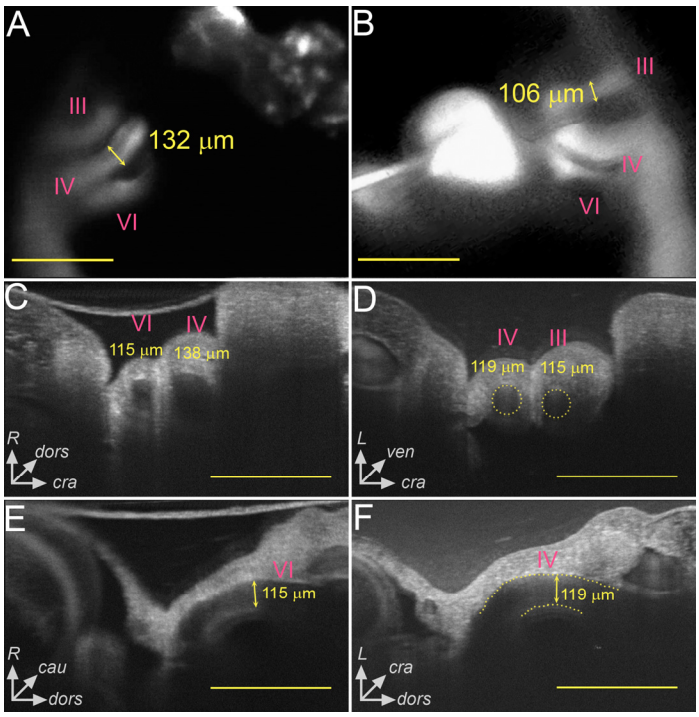

Figure 5. Multimodal imaging was used to obtain *in vivo* AA diameter measurements in HH21 chick embryos. Video recordings from fluorescent dye microinjections were processed to obtain individual AA identity and midpoint diameter data (A,B). OCT was used to obtain transverse (C,D) and longitudinal (E,F) sections through the AA to analyze midpoint diameter and AA tapering. Both the right (A,C,E) and left (B,D,F) laterals were imaged. In D, the dotted circles represent the AA lumen based on our image processing algorithm. The dotted lines in F highlight the boundaries of the AA lumen. Comparison between imaging modalities showed good agreement ($p>0.05$). The axes in C-F demonstrate the dorsal (dors), ventral (ven), cranial (cra), caudal (cau), right (R), and left (L) directions to orient the reader. Scale bars are 500 μm.

Eggs were windowed as described above and placed in a temperature and humidity controlled imaging chamber. We acquired time-resolved 757 x 757 (1.5 x 1.5 mm) 2D transverse image sequences, each lasting approximately five cardiac cycles. As the AA curves

around the foregut to connect to the dorsal aorta (DA), its proximal portion has a significant lateral orientation while the mid to distal region is oriented predominantly dorso-ventral. We acquired transverse sections approximately halfway between the start of the dorso-ventral orientation and the connection to the DA (Figure 5). Sequential 2D images were averaged in order to identify the AA lumen by negative contrast (Figure 5). Red blood cells produce a transient reflection as they pass through the scanning beam, and applying an intensity-average removes these areas while maintaining the constant signal from the surrounding tissue. We applied an *ad hoc* image processing code to quantitatively measure AA diameter from OCT scans. Approximately 10 discrete points marking the boundary of the AA lumen were manually selected from an intensity-averaged 2D transverse image. The centroid and radius were then computed by fitting the circle equation to the selected points. A total of 17 right lateral and 10 left lateral embryos were analyzed using OCT, with one measurement per AA per embryo. We performed two-tailed, unpaired t-tests assuming equal variance to determine significant differences ($p<0.05$) in AA diameters at HH21 (right vs. left lateral of the same AA pair, right laterals compared against each other, left laterals compared against each other).

For some of the HH21 embryos, the full AA lumen could not be visualized with OCT due to excessive light scattering at the air-egg interface and through the pharyngeal arch tissue (Figure 5). During the manual identification of the lumen, we only selected points where the boundary was clearly visible, normally encompassing an arc length of 1/2 to 2/3 of the total circumference. To test whether this truncated arc affected our measurements, we applied our technique to a phantom vessel of known diameter. Our phantom consisted of a clear nylon fiber (Stren Original 4 lb monofilament fishing line, Pure Fishing, Inc., SC) submerged in water. The expected fiber diameter, measured with a micrometer, was 203 μm. We acquired a 757 x 757

transverse image of the phantom using our OCT system and selected 14 points marking the fiber boundary, including 9 points distributed along the top 1/2 of the circumference and 5 points along the bottom 1/3. We then computed four diameter measurements, each using different subsets of the total 14 points selected to determine if the circular arc length contained by the selected boundary affected our measurement (Figure 6). The OCT measured fiber diameter was 240 μm and only varied by 2 μm when the number and circumferential distribution of the selected points changed. This test demonstrated that the truncated arc selected during AA measurements will produce a valid result and that the entire cross section does not need to be visible. The OCT measured diameter was larger than the expected fiber diameter (18% error), which may indicate over-estimation when applying our measurement technique to the AA. Considering the average AA diameter of 113 μm (Table 3), this error indicates our measurements are accurate to within 20 μm and is within the standard deviation (SD) of the AA diameters. However, the discrepancy in the fiber measurement may also be due to the tolerance of the micrometer.

To further assess the diameters computed from the circle fitting method, we acquired longitudinal AA sections for those embryos where the inner-most wall of the AA was visible under OCT (Figure 5, note that the inner-most wall is towards the bottom). A total of four longitudinal AA images (2 right, 2 left) were acquired for this comparison, and we obtained three diameter measurements per AA at different points along the vessel length. The measurement from the longitudinal section taken at approximately the same position as the transverse section agreed well with the diameter computed from the circle fitting method in all cases (within ±5 μm, we did not perform statistical t-tests due to the insufficient sample sizes). The diameters reported here only refer to those from the transverse images, as the longitudinal sections were

only used to check the fairness of those measurements. The longitudinal measurements, and that the OCT and fluorescent dye measurements agree, suggest that our OCT data are an accurate measurement of AA lumen diameters.

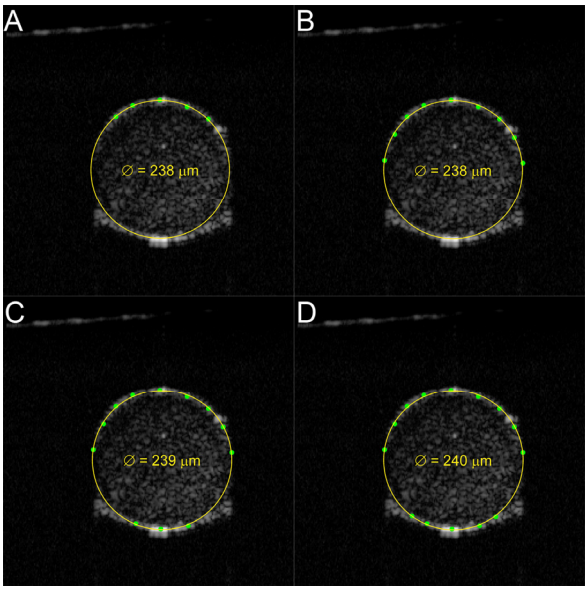

Figure 6. Diameter measurement of a nylon filament using OCT. Each panel (A-D) represents the diameter computed based on the selected points (green dots). The best fit circle is shown in yellow and the diameter is given at the center. The distribution of the selected points around the circumference of the fiber did not significantly affect the calculated diameter. This method is sufficient to measure AA diameters from transverse sections where the entire lumen boundary is not visible.

2.2.2 3D aortic arch imaging and reconstruction

We injected a rapidly polymerizing resin (diluted MICROFIL® Silicone Rubber Injection Compounds MV-blue, Flow Tech Inc, Carver, MA) into HH21 embryos to obtain 3D casts of the AA, as previously described by our group (Wang et al., 2009). Casts were scanned using micro-CT (Scanco Inc.) and we reconstructed 3D models using our established protocols (Wang et al.,

2009). We acquired micro-CT scans of 20 embryos. Several selected scans were imported into computer-aided modeling software (Geomagics Inc., Durham, NC) and combined to create a representative AA geometry with smooth inflow/outflow boundaries required for CFD. This baseline model contained AA III and IV, as they are the two vessels present across HH21 (see Results below). Using fluorescent injection and OCT imaging as a guide, we transformed the baseline configuration into the other three patterns observed at HH21 by adding AA vessels using our sketch-based 3D anatomical editing tool (Dur et al., 2011). The 3D models compared well with experimental measurements (Table 6, Table 7), supporting realistic data from CFD analysis.

2.2.3 Computational fluid dynamics simulation and analysis

We performed 3D CFD simulations as previously described (Wang et al., 2009). A pulsatile 2^{nd}-order CFD solver (Fluent 6.3.26, ANSYS Inc.) simulated blood flow through the AA models, applying rigid, no-slip walls and Newtonian assumptions ($\rho = 1060$ kg/m^3, $\mu = 3.71 \times 10^{-3}$ Pa-s) (Al-Roubaie et al., 2011). We prescribed time-dependent flow waveforms as plug-flow inflow boundary conditions, based on our previously published outflow tract (OT) velocity measurements (Figure 7) (Yoshigi et al., 2000). The distribution of cardiac output to the trunk and cranial vessels was set at a ratio of 90/10 using flow-split boundary conditions (Hu and Clark, 1989). Steady-state solutions were used to initialize the flow field prior to transient solutions. Convergence was enforced by reducing the residual of continuity equation by 10^{-6} at all time steps. Flow variables were monitored in real-time at the aortic inlet and descending aorta outlet during the course of each solution to ensure that nonlinear start-up effects were eliminated. A mesh sensitivity study at three refinement levels was performed to assure grid independency. Six cardiac cycles were simulated and required approximately 48 h on a Linux

workstation with two Quad Core Intel Xeon processors (8 nodes each 2.66 GHz) with 8GB of shared parallel memory.

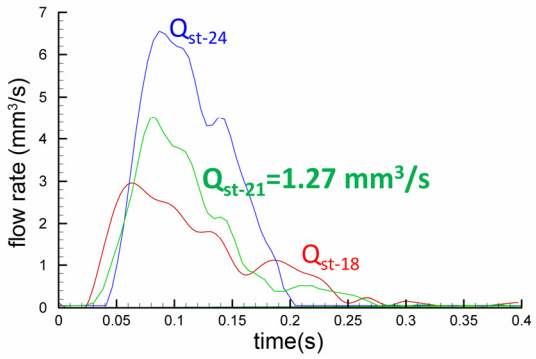

Figure 7. The pulsatile flow waveform used to represent a single cardiac cycle at the OT for the CFD model was interpolated from the data published by (Yoshigi et al., 2000).

2.3 Results

2.3.1 Variation of aortic arch number and type at HH21

In our previous study of HH18 and 24 embryos, we observed no inter-embryo variation in AA configurations; HH18 contained AA II, III, and IV while HH24 contained AA III, IV, and VI (Wang et al., 2009). In the present investigation of HH21 embryos, however, we identified four different AA configurations based on visual inspections of fluorescent dye injections, demonstrating significant variability (Figure 8). Anatomical landmarks, such as pharyngeal arch 2, were used to identify the AA present. Two three AA patterns were observed, which we refer to as 3AA-cranial (AA II, III and IV present) and 3AA-caudal (AA III, IV, and VI present). A two AA configuration, 2AA, was found with only AA III and IV present. A four AA configuration, 4AA, displayed AA II, III, IV, and VI. The 3AA-cranial contains the same AA as HH18 while the 3AA-caudal includes the same AA as HH24 (Wang et al., 2009). The 2AA and 4AA patterns are unique to HH21. All four configurations were observed for both laterals in at

least two embryos. The 3AA-caudal configuration appeared the most frequently (n = 20 right, n = 8 left), followed by 4AA (n = 5 right, n = 5 left), 3AA-cranial (n = 4 right, n = 3 left), and finally 2AA (n = 3 right, n = 2 left). Although lacking simultaneous left and right lateral measurements in the same embryo, our analysis confirmed bilateral symmetry of all AA configurations by observing the flipped embryos after injection and cessation of heart beat.

We did not observe AA V in any of our fluorescent dye injections. Polymeric casts suggest that AA V branches from and then reconnects to AA VI prior to anastomosis with the DA and that it is significantly smaller than the other AA (Hiruma and Hirakow, 1995). The large size of pharyngeal arch 2 allowed us to identify which AA vessels were present with little difficulty and there were no disagreements when comparing independent observer classifications. AA V may not be fully formed by HH21 or does not receive significant flow to produce a fluorescent signal; therefore, we cannot confirm the presence of AA V at HH21.

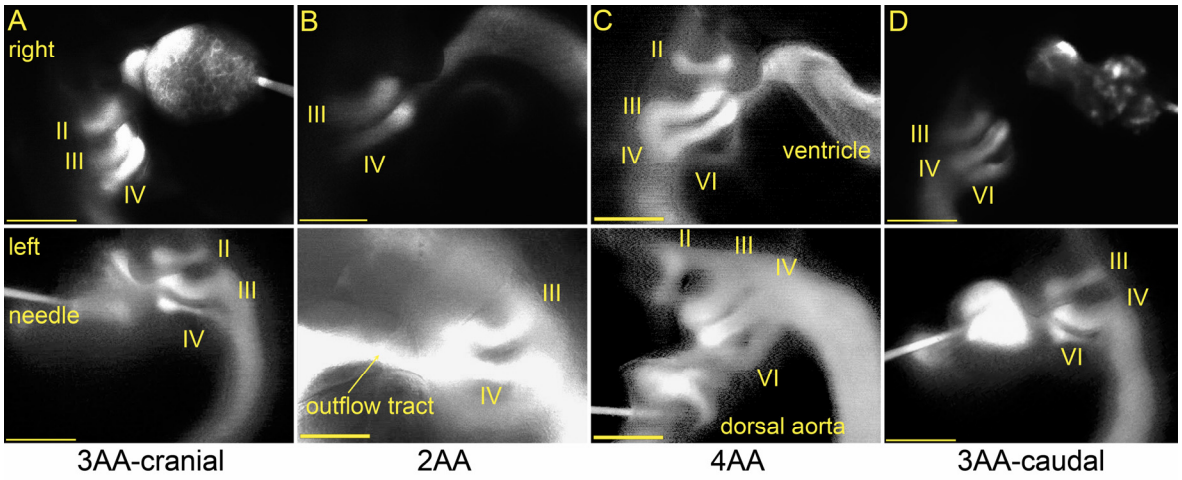

Figure 8 Four distinct AA configurations were observed at HH21, identified through fluorescent dye microinjection. Right (top) and left (bottom) lateral snapshots from video recordings are shown. (A) The 3AA-cranial pattern includes AA II, III, and IV. (B) The 2AA pattern only includes AA III and IV. (C) AA II, III, IV, and VI are present in the 4AA configuration. (D) The 3AA-caudal pattern includes the caudal-most AA VI. Scale bars are 500 µm.

2.3.2 Dimensions of the HH21 aortic arches

Average mid-point AA diameters were measured from fluorescent dye injections after classification of the AA configuration. The inter-observer bias in fluorescent dye measurements was 2 μm and the limits of agreement were -26 to 29 μm, demonstrating reasonable agreement. AA measured with OCT were not classified, and data from OCT was combined with all fluorescent dye data to generate the average HH21 diameter measurements (Table 3). Fluorescent dye injection and OCT measurements were unmatched, though the average difference between mean diameters obtained using the two methods was 5 μm, suggesting close concordance. Further, a two-tailed, unpaired t-test did not show significant differences between the two methods ($p>0.05$). Statistical comparison of the HH21 AA diameters revealed that the left lateral AA VI was smaller than the left lateral AA IV and III ($p<0.05$, Table 3). Using only the classified fluorescent dye data, we performed further analysis to determine if significant differences in AA diameter existed between the AA configurations. For the vast majority, no significant differences were found; however, the right lateral AA II was larger in the 3AA-cranial vs. 4AA configuration, and the left lateral AA III was larger and the left lateral AA IV smaller in the 3AA-cranial vs. 3AA-caudal configuration (Figure 9). These data indicate that although AA configurations vary at HH21, AA diameters are fairly uniform throughout the HH21 time period. However, we also recognize that the small sample size of certain AA configurations (i.e. 2AA) may limit statistical comparisons. We also compared the average HH21 diameter data with our previous measurements at HH18 and 24 (Wang et al., 2009) and found significant differences ($p<0.05$) between both AA IV laterals from HH18 to 21, and between the right lateral AA IV and both AA VI laterals from HH21 to 24 (Figure 10, Table 4). In all cases, the diameter was larger at the later stage.

Table 3. Average AA midpoint diameter (±SD) for all four possible AA present at HH21.

AA	Midpoint diameter (±SD) (mm)	
	R	L
II	0.109 (0.009)	0.110 (0.024)
	n = 9	n = 8
III	0.125 (0.020)	0.114 (0.019)*
	n = 39	n = 27
IV	0.123 (0.021)	0.115 (0.021)†
	n = 49	n = 28
VI	0.118 (0.026)	0.094 (0.027)*,†
	n = 41	n = 14

*,† indicate a statistically significant difference ($p<0.05$) between AA diameters

Table 4. Average HH21 AA diameter (±SD) data compared with our previous HH18 and HH24 data (Wang et al., 2009).

		Midpoint diameter (±SD) (mm)			*n* (number of embryos)		
AA	lateral	HH18	HH21	HH24	HH18	HH21	HH24
II	R	0.112 (0.021)	0.109 (0.009)		23	9	
	L	0.101 (0.025)	0.110 (0.024)		33	8	
III	R	0.129 (0.037)	0.125 (0.020)	0.123 (0.016)	23	39	30
	L	0.127 (0.023)	0.114 (0.019)	0.112 (0.015)	33	27	24
IV	R	0.083* (0.020)	0.123*,‡ (0.021)	0.140‡ (0.024)	23	49	30
	L	0.075† (0.011)	0.115† (0.021)	0.118 (0.019)	29	28	24
VI	R		0.118♦ (0.026)	0.138♦ (0.024)		41	29
	L		0.094♣ (0.027)	0.113♣ (0.019)		14	24

*,†,‡,♦,♣ indicate a statistically significant difference ($p<0.05$) between AA diameters.

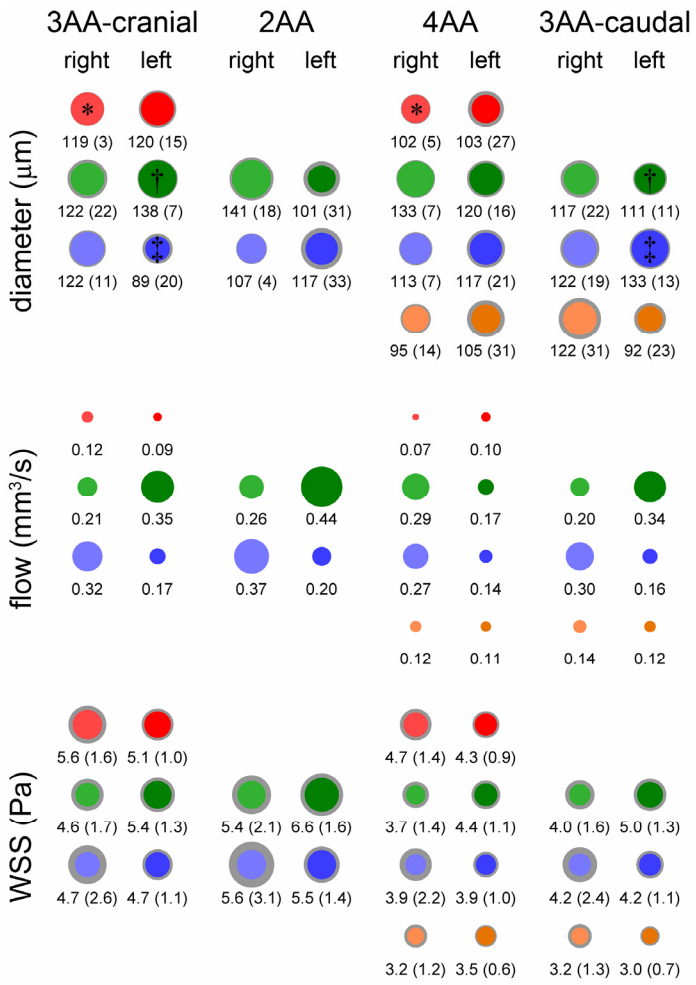

Figure 9. Average (±SD) AA midpoint diameters, cardiac cycle-averaged flows, and spatially-averaged (±SD) cycle-average WSS levels for each of the four configurations present at HH21. AA diameters are scaled, with values given below. Gray boundaries give the SD. *,†,‡ indicate significant differences ($p<0.05$) in AA diameter.

2.3.3 Distribution of cardiac output in the HH21 aortic arches

Figure 9 depicts the cardiac cycle-averaged flow rates and spatially-averaged cycle-averaged WSS values calculated by CFD analysis for all four HH21 configurations. Individual AA flow estimations from CFD agree well with previously published Doppler ultrasound flow measurements reported in the HH24 chick embryo (Hu et al., 2009). Flow through the AA

manifold was laminar, with maximal Reynolds number of less than 20 at the junction between the OT and aortic sac. Womersley numbers were less than 1 in all AA.

For all four configurations, AA III and IV were the most perfused, comprising 45% and 38% of the total cardiac output, respectively. AA II and VI received the least flow in the 3AA-cranial and 3AA-caudal cases, respectively, and were also the least perfused AA in the 4AA case (13% to AA II, 18% to AA VI of total cardiac output). Flow in the 2AA configuration was split almost evenly, with AA III receiving 55% of the total cardiac output compared to 45% for AA IV. For all but the 4AA configuration, cardiac output was split evenly between the right and left laterals; in the 4AA case, the right laterals received 60% of the total cardiac output. In the configurations in which they appear, AA II and AA VI received considerably less flow, though this disparity was less pronounced in the left laterals of the 4AA case. For the left laterals, AA III received the most flow in all configurations, though in the 4AA case flow was more evenly distributed among the left lateral AA. For the right laterals, AA IV received the greatest amount of flow for all but the 4AA configuration, in which AA III and AA IV were nearly equally perfused. Examining each AA pair individually, the right lateral of AA II received 57% of all AA II flow in the 3AA-cranial configuration, a distribution that was reversed in the 4AA case (left lateral AA II received 59% of AA II flow). AA III flow was consistently split 63% to 37%, between the right and left lateral, with the left lateral receiving the larger share for all but the 4AA configuration, in which the right lateral received 63% of the flow. In all cases, the right lateral AA IV received 65% of the cardiac output directed to AA IV. This was the largest difference (65% vs. 35%) between right and left lateral flow distribution for any AA pair. Flow to AA VI was split nearly evenly between its laterals, 52% right vs. 48% left for both configurations in which it appeared.

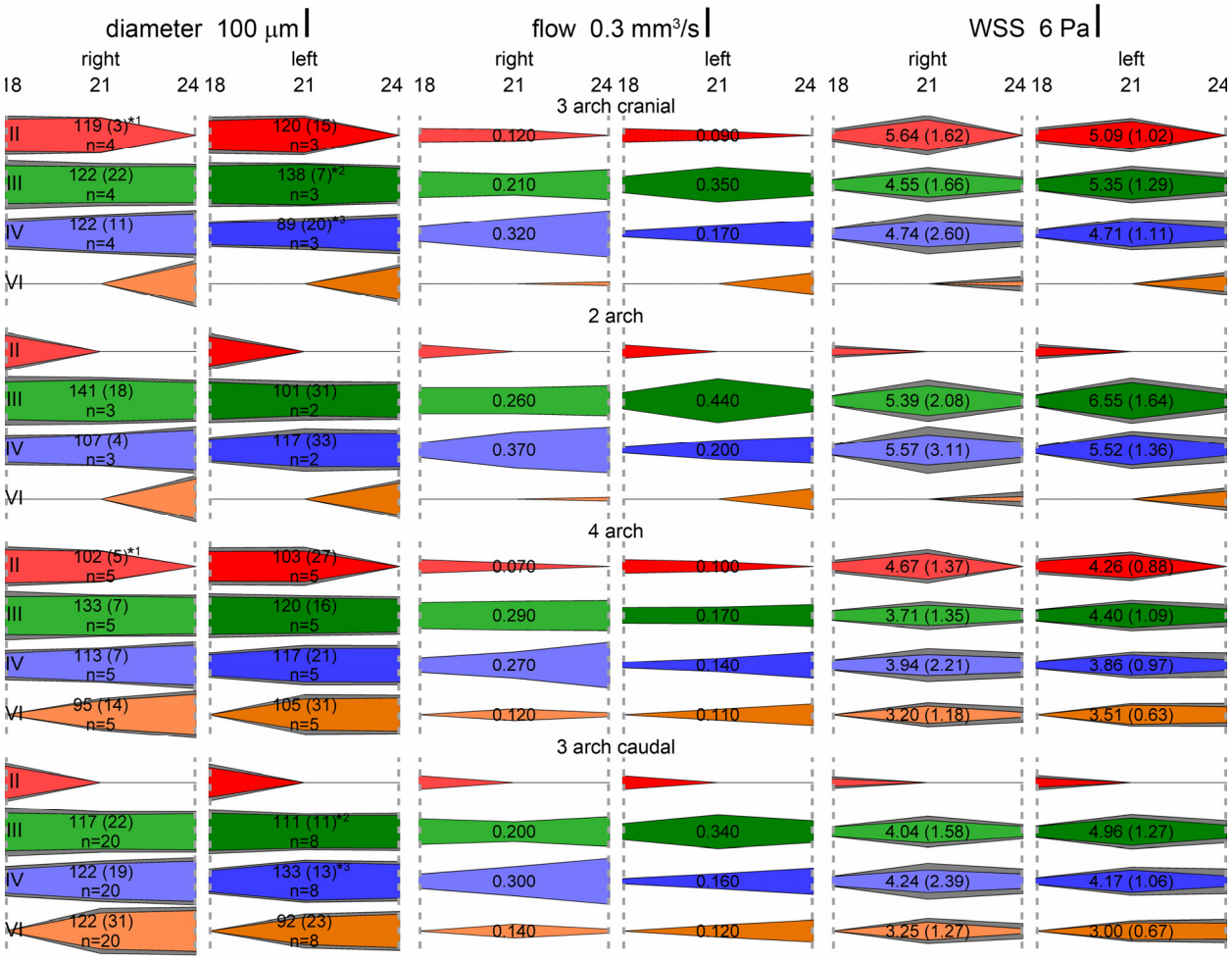

Figure 10. Graphical comparison of average AA midpoint diameter (±SD), cardiac cycle-averaged flow, and spatially-averaged (±SD) cycle-average WSS levels for each of the four configurations at HH21 with the preceding (HH18) and succeeding (HH24) data from our previous work (Wang et al., 2009). Widths of bars are scaled, with values provided for HH21. Gray boundaries give the SD. The rate of change of diameter, flow, and WSS is dependent on the HH21 AA configuration. Significant differences ($p<0.05$) between HH21 diameters are designated with *, where superscripts delineate the statistical pairs.

2.3.4 Distribution of WSS patterns in the HH21 aortic arches

With respect to our previous data (Wang et al., 2009), WSS was elevated in all AA at HH21 compared to the previous (HH18) and later (HH24) time-points (Figure 10). WSS levels at HH18 and 24 were between 1 and 3 Pa, compared to the 3-7 Pa range at HH21. Spatial distribution of WSS, including the acceleration, peak, and deceleration phases of the cardiac cycle, is depicted in Figure 11. The highest WSS zones were located at the junction between the OT and aortic sac, and in the narrow segments of AA III. WSS levels were similar in all AA pairs, though AA VI levels were relatively lower in the configurations where it appears (Figure 9). Examining AA pair by pair, the WSS levels in the right lateral of AA II were always higher than its left lateral (0.5 Pa higher on average). This situation was reversed for AA III, where the left lateral was exposed to higher WSS levels (average of 0.9 Pa higher). As in the flow distribution, AA IV WSS levels were consistently higher in the right lateral, though this difference was less dramatic than the AA II and III WSS (less than 0.1 Pa on average). WSS levels in AA VI were also similar in both laterals, with an average difference of 0.3 Pa.

The increased WSS at HH21 can induce significant changes in AA growth through shear-mediated genetic and signaling pathways. That WSS levels at HH24 are similar to those at HH18 suggests mechanical restoration, a theory introduced for biomechanically-regulated growth (Beloussov, 2008; Taber, 2009). This theory, in which tissues are expected to grow and remodel in an attempt to restore homeostatic or optimal loading conditions, has been demonstrated in limited embryonic applications (Taber and Eggers, 1996; Taber et al., 2001). Additional research is required to determine target stress states in the embryo, which may change over the course of development.

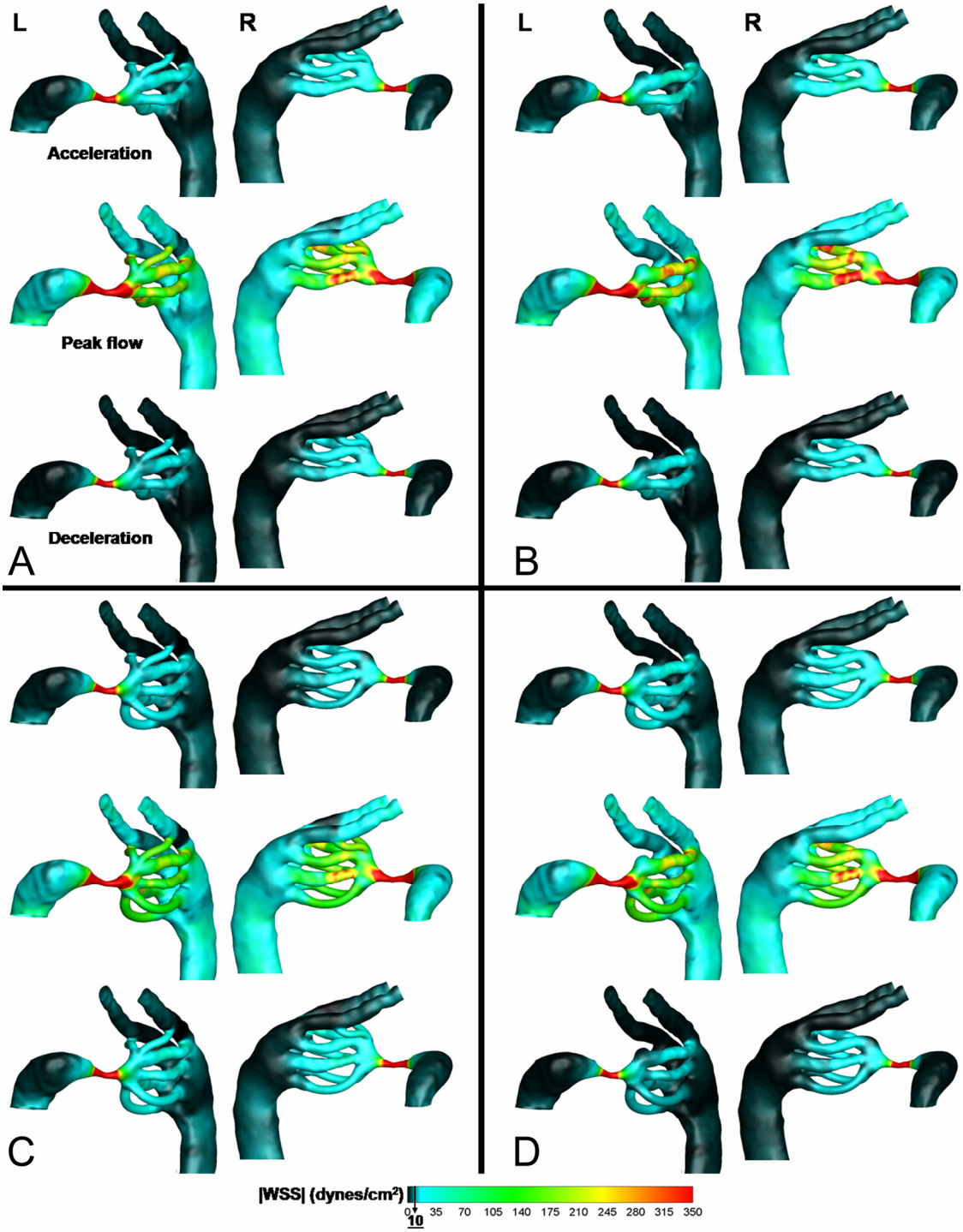

Figure 11. AA WSS distributions computed from CFD simulations for each of the four configurations observed at HH21. Acceleration, peak, and deceleration phases of the cardiac cycle are depicted. (A) 3AA-cranial, (B) 2AA, (C) 4AA, (D) 3AA-caudal.

2.3.5 Correlation between WSS variation and diameter change

In an attempt to further define the relationship between WSS and vascular growth, we determined if a correlation exists between an incremental change in vessel diameter and a change in WSS. We performed a regression analysis on the differences between average left and right lateral diameter and WSS values at HH18 and 21 and HH21 and 24 for AA III and IV. For six of the eight AA vessels, a 2nd-order polynomial function strongly correlated variation in WSS with change in diameter (p=0.002, Figure 12), consistent with hyper-restoration theory. Outliers to this trend included both the right and left lateral of AA III during growth from HH18 to 21. It is noteworthy that the change in WSS must exceed some threshold to produce a significant change in AA diameter, and increases in WSS have a greater effect than decreases. Deviations from this trend (i.e. WSS decreasing and diameter increasing) were observed when comparing each HH21 configuration separately to the HH18 and 24 data (Figure 10) and may be related to cellular heterogeneity within the AA, causing different responses to WSS levels.

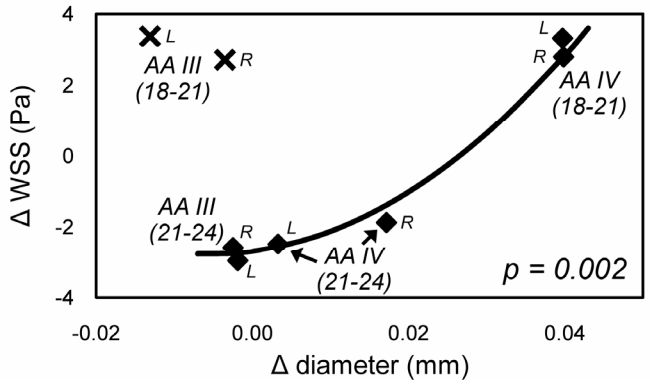

Figure 12. Comparing changes in diameter with changes in WSS from HH18 to 21 and HH21 to 24 for AA III and IV revealed a 2nd order polynomial relationship (p=0.002). Growth of AA IV from HH18 to 21 and growth of both AA III and IV from HH21 to 24 follow this trend.

2.4 Discussion

2.4.1 Inter-embryo variability in aortic arch patterns coincides with increased wall shear stress

Our fluorescent dye injections demonstrate significant variations in AA patterns at HH21, which was not observed at previous (HH18) or later (HH24) developmental time-points. This inter-embryo variability was also noted by Pexieder, who documented similar observations at four hours prior to and after HH21 (Pexieder, 1969). Pexieder's observations underscored the importance of using developmental staging landmarks rather than duration of incubation time in assigning developmental stage to maturing avian embryos. CFD models of all four HH21 AA configurations show a concomitant acute increase in WSS. Compared to our previous study of HH18 AA (Wang et al., 2009), we found an average increase of 3.1 Pa (nearly 2 fold) per AA at HH21; WSS then reduced 2.5 Pa (0.5 fold) by HH24. This escalation in WSS is likely due, in part, to the exponential rise in cardiac output that occurs during development, though more research is needed to determine these effects (Chapter 1, §1.2.1, Figure 4). Based on the coincidence between AA pattern variability and the transient sharp increase in WSS, we hypothesize that HH21 represents a period of dynamic AA growth, regression, and generation events, which attempt to restore normal loading. While many experiments indicate the importance of flow distribution in AA growth and morphogenesis (Hogers et al., 1999; Hu et al., 2009; Rychter and Lemez, 1965), the WSS after intervention remains unknown. Future work to characterize the biomechanical environment in these perturbed flow models is required to test this hypothesis.

2.4.2 Asymmetric cardiac output distribution to the aortic arches

Our CFD results demonstrated clear differences in cardiac output distribution to AA pairs, as well as asymmetric perfusion between the laterals of distinct pairs (i.e. AA IV). Our group recently developed, as detailed in Chapter 3, an optimization-based model for AA growth, where the individual AA diameters were free to alter in response to a global objective function that minimizes the total energy expenditure while maximizing diffusive capacity (Kowalski et al., 2012). This model demonstrated that there was always one dominant (larger diameter) AA, the selection of which was strongly related to the orientation of the OT. The OT orientation acted to preferentially direct flow to one of the AA vessels, which became the dominant AA. This model showed similarities to the classic problem of competing collateral vessels, where small perturbations in the distribution of blood flow cause one vessel to dilate due to increased WSS while the others constrict due to a decrease in WSS, eventually leading to reduction to a single vessel (Hacking et al., 1996; Hudetz and Kiani, 1992; Keenan and Rodbard, 1973). Based on this work, the asymmetry observed in AA IV flow at HH21 (right-lateral dominant, Figure 9) may explain the asymmetric growth of this AA pair, where the left lateral disappears and the right lateral forms a section of the mature arch of aorta. If we consider AA IV as two vessels competing for flow, then this flow asymmetry would predict degeneration of the left lateral. The low flow to AA II may also explain its eventual remodeling to a capillary bed by a similar principle. Asymmetric flow distribution was shown to affect platelet-derived growth factor-A and vascular endothelial growth factor receptor-2 signaling in the asymmetric remodeling of AA VI in the mouse, providing further support for this theory (Yashiro et al., 2007). To date, inherent asymmetry in vascular growth-related gene expression among the AA has not been

documented, suggesting that environmental, epigenetic factors such as WSS may play an important role in this process.

Multiple studies using intervention methods to disrupt normal flow in embryos near HH21 have reported significant subsequent abnormalities in AA growth. Rychter and Lemez (Rychter and Lemez, 1965) tracked the distribution of blood from the vitelline veins in HH13, 15, and 18 chick embryos, demonstrating clear patterns in AA perfusion. Exclusion of these veins by transection or ligation subsequently re-routed flow to AA not normally perfused from the tested location. Using India ink injections, Hogers et al. (Hogers et al., 1999) extended this vitelline ligation model to demonstrate that intracardiac flow patterns were also disrupted. Further, embryos were examined through hatching, revealing multiple defects in AA development, including hypoplastic right brachiocephalic artery, interrupted aortic arch, double aortic arch, and hypoplastic pulmonary artery. Using only video microscopy, Hu et al. (Hu et al., 2009) reported similar anomalies in AA perfusion patterns in the left atrial ligated (LAL) chick embryo. Individual AA flow rates were quantified with laser Doppler velocimetry, and demonstrated a significant reduction of flow in all AA in the LAL embryos, although the flow ratios remained similar to the control group. Examination of LAL embryos to HH27 and 34 revealed defects such as absent AA III and IV and AA hypoplasia.

It is possible to test the effects of altered OT flow patterns using our current CFD models. As described in our CFD methods, the velocity profile at the OT was plug shaped. The plug flow profile at the outlet of the beating ventricle is an established and valid assumption of cardiovascular fluid dynamics modeling (Milnor, 1989), and is therefore employed in this study as well. To examine the effects of other profile shapes, we used the 3AA-cranial model and altered the inlet boundary condition. We prescribed two conditions: 1) a normal parabolic

profile, with the maximum velocity occurring at the centroid of the inlet surface, and 2) a skewed parabolic profile, where the maximum velocity is offset from center. We modeled pulsatile flow, using the same HH21 waveform (Figure 7), and kept the remaining boundary conditions and model parameters unchanged. Neither profile significantly altered the flow distribution, with an average difference of 1% (Table 5, Figure 13). This small effect is likely because the profile rapidly becomes fully developed (parabolic) by the time it reaches the aortic sac, even though we prescribe a plug-flow profile at the inlet. This flow development occurs particularly in the embryonic OT since it has a narrow constriction upstream of our main area interest, the AA vessels. Furthermore, we expect that the narrowing of the OT and the low Reynolds number attenuates (as a function of the constriction diameter) any flow skewness that may be exist due to the looping of the heart. These results seem to suggest that, even if the altered intracardiac flow patterns resulted in a skewed profile at the OT, its effects on AA flow distribution would be small and possibly insufficient to cause morphogenetic abnormalities. However, the OT of the early embryo through HH32 is contractile and changes its shape during the cardiac cycle (Watanabe et al., 1998). As our models do not incorporate this wall motion, the effects of the skewed profile may be underestimated. An AA flow model that incorporates the wall motion of the OT would provide further evidence; however it is not within the scope of the current study.

Table 5. HH21 3AA-cranial flow (mm^3/s) distributions using a plug, parabolic, and skewed parabolic inlet profile.

	plug		parabolic		skewed	
AA	R	L	R	L	R	L
II	0.120	0.090	0.121	0.089	0.121	0.089
III	0.210	0.350	0.210	0.351	0.209	0.351
IV	0.320	0.170	0.311	0.165	0.311	0.165

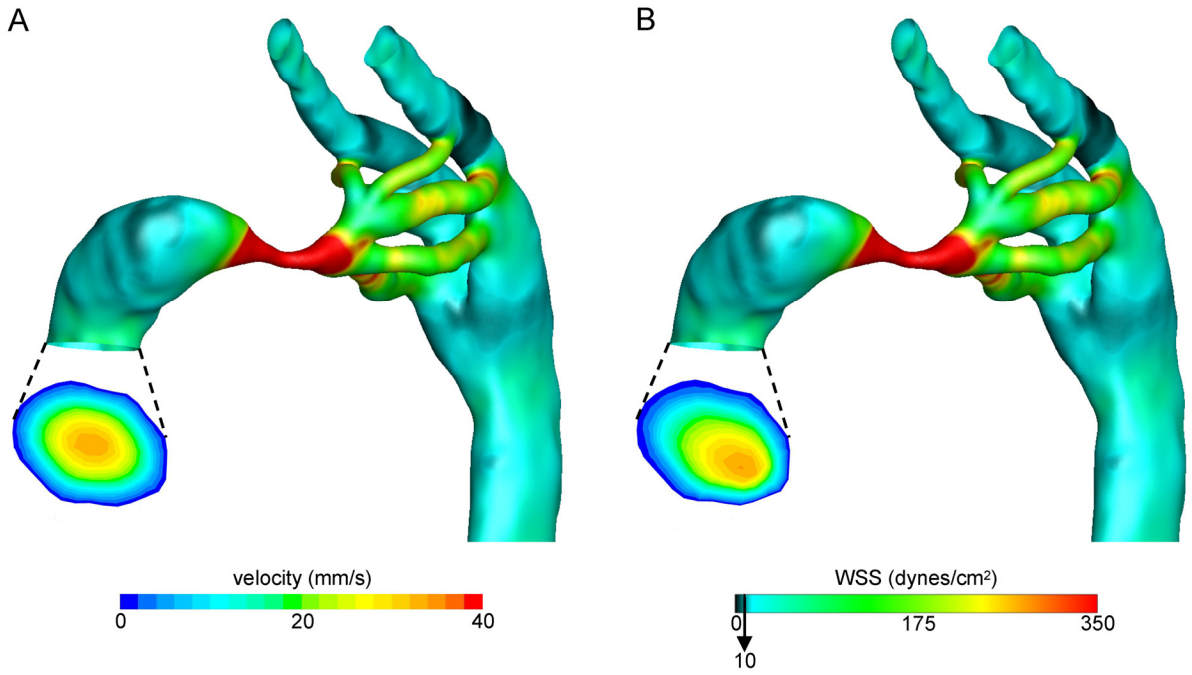

Figure 13. AA WSS distributions at peak flow in the 3AA-cranial configuration with a parabolic inlet profile (A), and skewed parabolic inlet profile (B). The velocity cross section shows the profile shape at the outflow tract. Compare to Figure 11.

2.4.3 Hypothetical model for transitions in aortic arch patterns at HH21

The multiple AA configurations at HH21 led us to propose two pathways by which the transition from the HH18 to 24 AA patterns occurs (Figure 14). Each of the four AA configurations observed at HH21 can represent a discrete snapshot occurring during the disappearance of AA II and emergence of AA VI. The 3AA-cranial configuration maintains the HH18 II, III, IV AA, and can be considered as the immature HH21 AA pattern. Similarly, as the 3AA-caudal configuration contains the same AA as the HH24 embryo, it can be referred to as the mature HH21. The remaining configurations, 2AA and 4AA represent two distinct intermediate HH21 configurations, which, in turn, demonstrate the two possible growth pathways by which AA II degenerates and AA IV becomes patent. To achieve the 2AA configuration, AA II must

degenerate before AA VI emerges; for the 4AA configuration to occur, AA VI must emerge before AA II disappears. While these two pathways can be logically deduced from our fluorescent injection data, the factors governing whether AA morphogenesis proceeds through the 2AA or 4AA pattern is unclear. Based on previous experiments demonstrating the importance of blood flow in AA growth, it is reasonable to propose that hemodynamic loading, such as WSS, has a role in this process. Mechanical restoration theory (Beloussov, 2008; Taber, 2009) may offer some insight: prolonged exposure to WSS above some critical value (WSS_{crit}) may lead to AA generation while WSS far below the normative level (WSS_{eq}) may lead to AA regression in order to restore loading to WSS_{eq} (Figure 14). Variations in the trend of cardiac output increase is one possible explanation for the selection of either the 2AA or 4AA pathway, where a sharp increase would lead to generation of AA VI and a slow increase in cardiac output would lead to regression of AA II. Simultaneous hemodynamic and structural measurements, which are not currently available, are needed to investigate this theory.

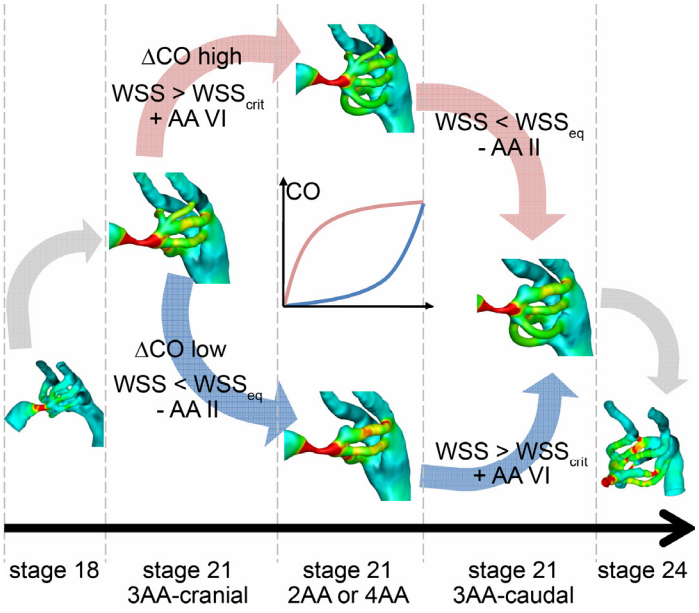

Figure 14. Theoretical growth pathways from HH18 to HH24 AA configurations. The transition can proceed through the 2AA or 4AA pattern depending on the timing of AA II

regression and AA IV generation. WSS may be one factor in selecting the pathway, where levels above a critical value (WSS_{crit}) lead to AA generation and WSS below an equilibrium level (WSS_{eq}) leads to AA regression. The rate of increase in cardiac output (CO) can affect WSS levels.

2.4.4 Relating wall shear stress to biologic events

Several published studies related to the biomechanical regulation of genetic, signaling, and cellular events involved in the normal growth and remodeling of the embryonic AA place the results from our CFD models into context with AA biology. Groenendijk et al. found that levels of high WSS were associated with Krüppel-like factor-2 (*KLF-2*) and endothelial nitric oxide synthase (*NOS-3*) expression, while low WSS areas expressed endothelin-1 (*ET-1*) (Groenendijk et al., 2004). Their 3D reconstructions of these expression patterns qualitatively overlap with the WSS magnitudes predicted by our current and previous CFD models (Wang et al., 2009). Egorova et al. demonstrated that chick endothelial cells have a dose-dependent relationship between WSS and Tgfβ/Alk5 signaling activity (Egorova et al., 2011b). Defective Alk5 signaling in mouse neural crest cells lead to AA hypoplasia and uncharacteristic regression (Wang et al., 2006). The asymmetric WSS in AA pair IV may result in asymmetric Alk5 signaling, leading to persistence of the right lateral and regression of the left lateral. Molin et al. examined *Tgfβ2-/-* mice and found significant defects in AA IV, though some mice had normal AA (Molin et al., 2004). This study indicated that SMAD2 signaling was critical for the development of AA IV and the authors hypothesized that the WSS levels in the unaffected *Tgfβ2-/-* mice were high enough to maintain Tgfβ1/Alk5 signaling for sufficient SMAD2 levels.

More experimental studies are required to link WSS with these molecular mechanisms and our CFD modeling techniques are well suited to determine 3D WSS distributions.

2.4.5 Modeling 3D blood flow in the embryonic aortic arches

As previously described, our 3D AA models were constructed from a library of micro-CT scans and therefore represent an average embryo. We verify the 3D geometries by comparing AA diameter (Table 6) and length (Table 7), both of which were quantitatively similar. Due to the smaller sample size of experimental length measurements, we further examined the influence of AA length using our previously published numerical parametric 2D hemodynamic model of the right lateral AA, described in Chapter 2 (Kowalski et al., 2012). Briefly, this model uses parametrically defined third order Bezier curves to describe the centerlines of the AA and then generates a lumen of uniform diameter by extracting in the normal directions. An OT and DA are incorporated at the proximal and distal ends, respectively. We modified this 2D model to represent the 3AA-cranial HH21 configuration and applied the HH21 cycle average flow rate to model a steady state simulation (only one half of the total flow was used as we only model the right lateral). As in the 3D models, we employed a rigid wall assumption and 90/10 trunk/cranial flow split at the DA. Blood properties remained the same as the 3D models. The parametric geometry allowed us to easily modify AA length and curvature. We performed simulations for 12 distinct geometry cases, varying the lengths and curvatures of each AA individually (Figure 15). We found that when the vessel length varied by 50%, the flow distribution and WSS were maintained within 20% of its original values (Figure 15). Furthermore, when the curvature of the AA was changed such that AA tortuosity increased by 10%, flow distribution and WSS were maintained within 10% of their original values (Figure 15). Therefore, we expect that the small difference between the AA lengths of the 3D models and the experimental measurements (~3%)

does not have a significant effect. While a larger number of experimental length measurements would provide additional evidence, our current data and 2D simulations indicate that even a difference up to 20% in AA length would have little effect on the flow distribution and WSS.

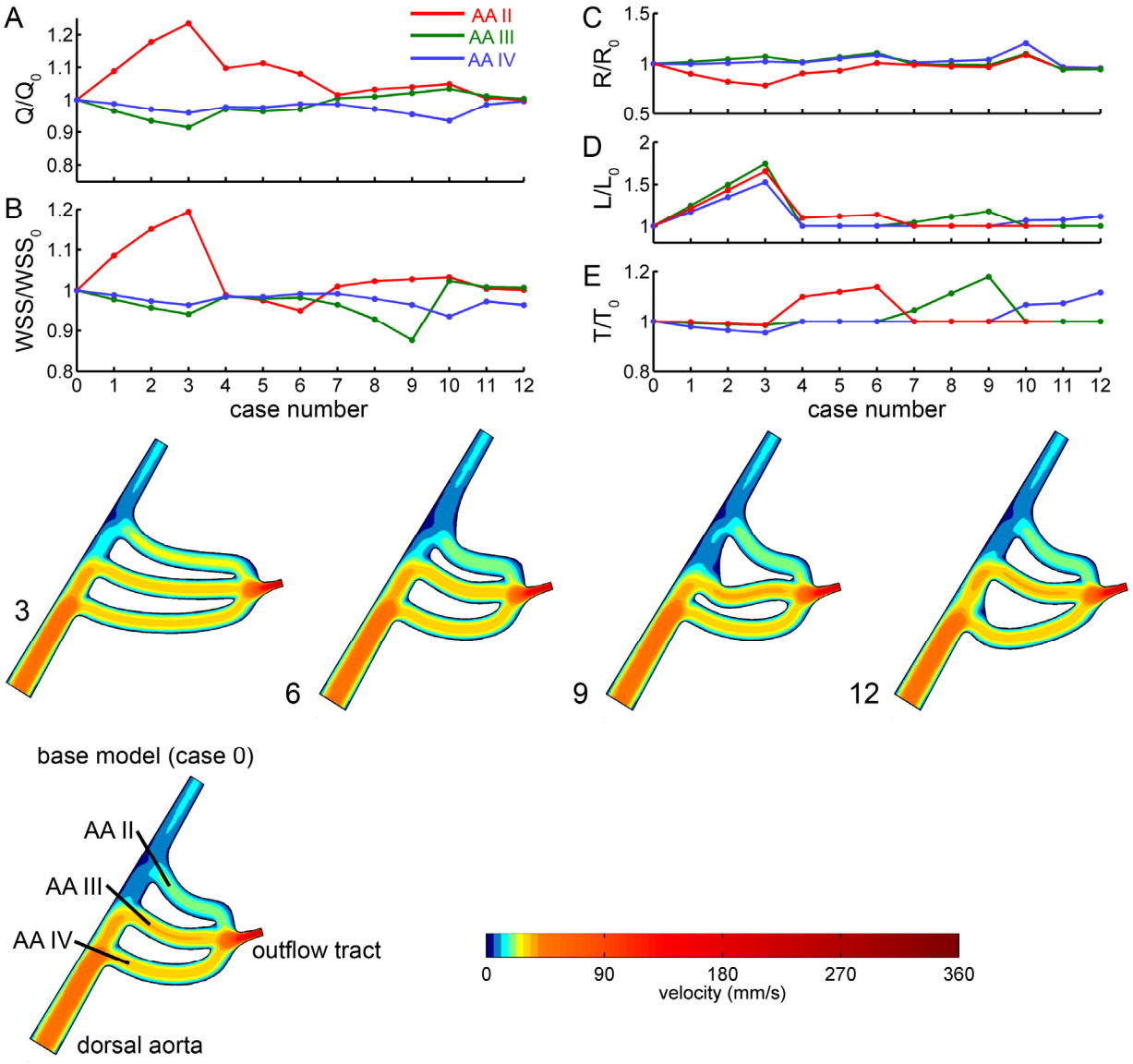

Figure 15. Effect of AA length and curvature on flow distribution and WSS. Our parametric 2D CFD model of the 3AA-cranial HH21 configuration was used to simulate 12 distinct AA geometries, varying the lengths and curvatures of each individual AA. Velocity fields for sample geometries are depicted. The base model (case 0) is shown in the lower left. Panels A-E show

the variation in flow rate (A), WSS (B), resistance (C), length (D), and tortuosity (E) compared to the base model. Resistance is computed as the pressure drop from the outflow tract to the outlet of the AA, divided by the flow through the AA. Tortuosity is the length of the AA divided by the Euclidean distance between its endpoints. Q – flow rate, R – resistance, L – length, T – tortuosity.

We further qualitatively compared our 3D AA models with previous descriptions of the AA at comparable stages including scanning electron micrographs (Hiruma and Hirakow, 1995), schematic illustrations (Waldo et al., 2005a), reconstructions from serial registered histological sections (Groenendijk et al., 2004; Poelmann et al., 2008), and MRM (Smith et al., 1992). Although 3D information is very limited in these reports, all of these studies are in qualitative agreement with the topology of composite 3D reconstructions in the current study. The integrity of the present 3D quantitative morphology of the AA was further verified 1) by overlapping the 3D reconstructions with the large set of 2D fluorescence dye injection recordings at several views, 2) through multiple snap-shots used for vessel diameter measurements, and 3) by the auxiliary micro-CT scans and 3D reconstructions with parametric segmentation and smoothing settings. These checks were previously applied to our HH18 and 24 models (Wang et al., 2009). It is clear from the longitudinal OCT sections that AA diameter is not constant along the vessel length (Figure 5), and this variation is captured by our 3D models. That the smallest diameter appears at the midpoint is consistent with previous reports that show formations of the AA lumens begin at the aortic sac and DA and gradually progress to the midpoint (Anderson et al., 2008; DeRuiter et al., 1993). The strong quantitative and qualitative agreement suggests that our

models provide good estimation of the flow and WSS distribution within the embryonic AA at HH21.

Table 6. Experimentally measured average (±SD) AA diameters compared with those in the 3D models used for CFD simulations. See Table 3 for experimental sample sizes.

AA	lateral	Measured diameter (±SD) (mm)	Model diameter (mm)
II	R	0.109 (0.009)	0.092
	L	0.110 (0.024)	0.086
III	R	0.125 (0.020)	0.123
	L	0.114 (0.019)	0.145
IV	R	0.123 (0.021)	0.148
	L	0.115 (0.021)	0.114
VI	R	0.118 (0.026)	0.122
	L	0.094 (0.027)	0.123

Table 7. Experimentally measured AA lengths compared with those in the 3D models used for CFD simulations. Experimental measurements were taken for a single AA sample (n=1) and one measurement was made per sample.

AA	lateral	Measured length (mm)	Model length (mm)	% difference
II	R		0.408	
	L		0.412	
III	R		0.736	
	L	0.610	0.615	0.89%
IV	R	0.706	0.740	4.78%
	L	0.655	0.725	10.71%
VI	R	0.613	0.596	-2.81%
	L		0.405	
average		0.646	0.580	3.40%

The CFD models used in this study are subject to several assumptions related to boundary conditions. We specify rigid walls, which may over-estimate the WSS values. As we compare these values to our previous HH18 and 24 models (Wang et al., 2009), which also employed a rigid wall assumption, the results related to these comparisons remain valid. While the AA wall is distensible, our experience with the chick embryo indicates that the expansion is small during systole. Our rigid wall models provide a good estimation of the biomechanical forces acting on

the embryonic AA during this critical stage in development. Measuring flow in these vessels using direct experimental techniques such as Doppler ultrasound or micro particle image velocimetry is difficult and prone to errors given their small size and limited access due to their position within the pharyngeal arches. A full fluid-structure interaction model would be necessary to capture the effects of wall compliance and the surrounding tissue. The outlet boundary conditions specify a 90/10 flow split between the trunk and cranial vessels. As the flow split is enforced by the CFD model, it is independent of the AA morphology. This distribution is based on Doppler ultrasound studies in the chick embryo, and is consistent across the investigated timeframe (Hu and Clark, 1989). The ratio of the cranial and trunk peripheral resistances set this distribution *in vivo*. Though the trunk peripheral resistance decreases geometrically from HH12 to 29, the ratio likely remains constant since the 90/10 flow split is maintained (Hu and Clark, 1989). Alterations in the peripheral resistance may change this flow split, leading to variations in AA perfusion and therefore WSS. We examined the effects of a 60/40 flow split using our HH18 model (Wang et al., 2009) and found that the larger cranial perfusion shifted approximately 5% of the cardiac output from the caudal-most AA pair IV to the cranial-most AA pair II (Table 8). Flow to AA pair III remained similar. Thus, peripheral resistance can have an effect on the AA flow distribution and the biomechanical environment. Indeed, increasing the downstream arterial resistance by ligating the right vitelline artery reduced dorsal aortic flow by 38% after one hour, though cranial flow and AA flow was not measured (Lucitti et al., 2005). Future research is required to determine the effects of altered peripheral resistance on AA flow.

Table 8. HH18 AA flow distribution in 90/10 and 60/40 trunk/cranial flow split boundary conditions.

	Flow (mm^3/s)				% Change	
	90/10 split		60/40 split			
AA	R	L	R	L	R	L
II	0.142	0.135	0.149	0.144	4.3	6.4
III	0.265	0.159	0.263	0.156	-0.5	-1.8
IV	0.145	0.055	0.138	0.052	-5.3	-5.4

2.4.6 Limitations

Although limited published data exists on AA dimensions, our data is consistent with these previous studies (Hu et al., 2009; Stewart et al., 1986). The 2D diameter measurements acquired from fluorescent dye images were influenced by both reflected fluorescent light and the volume of injected dye, requiring the large sample numbers. Due to the large size of pharyngeal arch 2, identifying the boundaries of AA II was sometimes difficult. The imaging depth using OCT is limited by the amount of light scattering caused by the sample and is normally 1.5 mm for biological tissue. At HH21, pharyngeal arch 2 causes excessive light scattering due to the thickness of the tissue and obstructs imaging of AA II and occasionally AA III when using OCT. Therefore, we did not measure AA II under OCT and did not attempt to classify AA configurations, as errors were likely to result due to the obscured cranial AA. The obstructed imaging of AA III is the reason for the different n-numbers between AA III and IV in Table 3. Measuring AA diameter with OCT assumes a circular cross-section, which we feel is valid. This technique is limited by observer identification of the AA lumen, which is considerably improved when averaging several B-scans.

The four HH21 AA geometries were created by adding additional AA to the baseline 2AA (III, IV) configuration. We used the same AA vessel geometries in each configuration (i.e. left lateral AA III, 3AA-cranial is the same as left lateral AA III, 3AA-caudal, etc.). This

strategy removes any differences in AA diameter or curvature that may exist among the four HH21 configurations and midpoint AA diameters in the models do not always exactly match those measured experimentally (Table 6). Neglecting these differences when constructing the models may result in an inconsistency between flow rates and WSS levels obtained from CFD and their actual, *in vivo* values. This possible discrepancy may be a reason for deviations in the trend between the change in WSS and change in diameter (Figure 12). A comparison of *in vivo* velocity data at each HH21 configuration would be necessary to determine the degree of this difference, however no such data currently exists. However, given that AA diameters are similar for all the HH21 configurations (see above), we expect that our method in creating the 3D model generated little error when comparing flow and WSS values.

2.5 Conclusions

Our study provides the first comparison between quantitative *in vivo* data and CFD-predicted flow and WSS patterns of the HH21 embryonic AA. We have shown a transient variability in the number and identity of AA present at HH21, creating four possible configurations. We applied multimodal imaging strategies to provide the first quantitative data on AA diameter at HH21, which revealed significant growth in key AA vessels (IV, VI) when compared to our previous data at HH18, and asymmetric growth of AA IV when compared to our HH24 data (right lateral grew significantly, left lateral remained the same). CFD analysis of all four HH21 configurations demonstrated changes in cardiac output distribution and elevated WSS levels compared to HH18 and 24. Our data revealed that changes in WSS and AA diameter are closely correlated, providing further evidence for flow-dependency in embryonic vascular growth. In particular, flow asymmetry in AA IV may relate to its asymmetric growth patterns based on

shear-mediated gene expression and signaling activation. The timing of events such as cardiac output increase and OT migration may have additional roles in the progression of AA growth and remodeling. Understanding the relationship between hemodynamics and the growth of the AA can provide insight into the progression of great vessel defects and other forms of CHD.

Chapter 3

Computational hemodynamic optimization predicts dominant aortic arch selection is driven by embryonic outflow tract orientation in the chick embryo

3.1 Introduction

Defects of the great vessels represent more than 20% of congenital heart disease in the United States (Roger et al., 2011), and can require multiple surgeries and substantial risk to partially restore normal arterial structure and function. While the etiologies of such defects are not yet fully understood, most can be traced back to morphogenetic insults that occur during the growth and early patterning of the embryonic aortic arches (AA), the precursors to the great vessels. These errors in morphogenesis are likely due to the combination of genetic events and environmental or epigenetic insults and embryo survival depends upon adaptive morphogenesis and remodeling. As described in Chapter 1 (§1.1.2, Figure 3), the immature symmetric system of AA arises sequentially in a cranio-caudal fashion and undergoes large-scale asymmetric morphogenesis to form species-specific adult great vessel patterns.

The emergence of AA pairs I-VI coincide with the formation of the cervical flexure, during which the cranio-caudal axis of the chick embryo transforms from a straight line to a U-shape, bending at the level of the pharyngeal arches (Flynn et al., 1991). Previous studies have shown that this process is closely related to cardiac looping (Flynn et al., 1991; Manner et al., 1993; Manner et al., 1995). Additionally, in the final looping events (HH18-24), the outflow tract (OT) undergoes a rotation and migration as it moves from a more rightward to centrally located position (Manner, 2000). Together, these events may change the orientation of the OT

relative to the AA over the course of cardiac looping. The orientation and position of the OT continues to shift as the spiral aortopulmonary septum septates the common trunk into the mature pulmonary artery and aorta (de la Cruz et al., 1977; Dor and Corone, 1985; Thompson et al., 1987). Arresting the migration and rotation of the OT by mechanical (Bremer, 1928; Dor and Corone, 1985; Gessner, 1966) and genetic (Bajolle et al., 2006; Liu et al., 2002; Yashiro et al., 2007) interventions have been shown to produce OT and a variety of AA abnormalities and has been implicated as a possible cause for several congenital defects in humans (Bostrom and Hutchins, 1988; Goor and Edwards, 1973; Lomonico et al., 1988). These studies suggest that the positioning of the OT may be a critical factor in the growth and selection of the AA.

Previous studies revealed that changes in AA perfusion by occlusion of a vitelline vein (Hogers et al., 1999; Rychter and Lemez, 1965), left atrial ligation (Hu et al., 2009), manipulation of the OT (Gessner, 1966), or ligation of individual AA (Rychter, 1962) generated abnormal AA growth and defects in AA derivatives. Though the exact molecular mechanisms involved in the relationship between AA hemodynamics and morphogenesis are not yet fully understood, wall shear stress (WSS) is believed to be the primary mechanical stimulus for vascular remodeling (Culver and Dickinson, 2010; Rodbard, 1975), clinically referred to as the "flow-dependency principle" (Kamiya and Togawa, 1980; Lu et al., 2001; Rodbard, 1975). The temporal and spatial events associated with flow sensitive altered AA morphogenesis (at the first AA) in the Akl-1 mutant zebrafish model can be more complex as illustrated by recent studies (Chen et al., 2011; Corti et al., 2011; Patrick et al., 2011).

Prolonged exposure to altered blood flow results in the normalization of WSS via an increase or decrease in vessel caliber (Bayer et al., 1999; Girerd et al., 1996; Langille and O'Donnell, 1986). This phenomenon has been explained by the mechanical hyper-restoration

theory, which postulates that biological systems tend to grow and remodel to return to a homeostatic state (Beloussov, 2008; Beloussov and Grabovsky, 2006; Taber, 2009). A variety of numerical studies have employed this theory to formulate restorative stress-based growth laws to model vascular growth and remodeling (Alford et al., 2008; Fung, 1990; Rodriguez et al., 1994; Taber and Humphrey, 2001; Valentin et al., 2011). These studies have been primarily performed in adult, diseased states (Figueroa et al., 2009; Watton et al., 2009) and postnatal growth of the aorta (Wagenseil, 2010). Limited embryonic applications (Taber and Eggers, 1996) were decoupled from the hemodynamic environment and only examined a straight, axisymmetric vessel segments.

Lack of sufficient data on the micro-structural and mechanical properties of the embryonic AA has limited the direct application of available growth rate laws (Rodriguez et al., 1994; Taber, 1998b) and micro-structurally motivated phenomenological models (Gleason and Humphrey, 2004; Humphrey, 1999) to AA morphogenesis. An alternative approach is to employ an *optimization-based* growth strategy to model vessel growth in complex cardiovascular morphologies in response to secondary anatomical alterations and sustained flow and pressure perturbations. Theoretical (Sherman, 1981; Taber, 1998c; Zamir, 1977) and experimental (Gruionu et al., 2005; Kassab and Fung, 1995; LaBarbera, 1990) studies have provided strong evidence that vascular morphology is governed by a set of physiological principles that tend to optimize cardiovascular performance. The most widely regarded is Murray's law, which states that minimization of the total energy to drive blood flow and maintain the metabolic cost of blood volume determines vascular morphology (Murray, 1926). Previous research has shown that minimization of energy is achieved through restoration of an optimal WSS (Kassab and Fung, 1995; Zamir, 1977), which is dependent on local pressure (Pries et al., 1995; Taber,

1998c). This relationship suggests that perturbed hemodynamic loading drives vascular remodeling, potentially resulting in diseased conditions. While Murray's law generally holds for the patterning of vascular trees involved in bulk transport, other models have been proposed for the optimal design of microvasculature, which seek to balance energy utilization with diffusive capacity (Kamiya et al., 1987; Kamiya et al., 1993; Khanin and Bukharov, 1994). Although these models have hinted the feasibility of a predictive optimization-based growth numerical framework, their zero- or one-dimensional formulation inherently lacked the capability for accurate evaluation of the hemodynamic loading, effect of dynamic anatomical variations, and functional requirements of neighboring vasculature, which may also dictate the local vessel growth (Zamir, 1977).

Our previous CFD models of flow in the AA (described in Chapter 2), based on micro-computer tomography (micro-CT) 3D reconstructions of HH18, 21, and 24 chick embryos, demonstrated that the distribution of cardiac output to the individual AA vessels shifts significantly between HH18 and 24. (Figure 16) (Kowalski et al., 2013; Wang et al., 2009). Qualitative assessments based on the 3D reconstructions reveal a change in the angle of the OT relative to the AA across developmental time points, consistent with the studies described above (de la Cruz et al., 1977; Flynn et al., 1991; Manner, 2000; Manner et al., 1993; Manner et al., 1995). These results suggested that the change in position of the OT may redistribute cardiac output, leading to differential growth of the AA due to hemodynamic loading.

In the present study, we tested the hypothesis that the angle of the OT relative to the aortic sac dictates the local hemodynamic environment of the individual AA vessels and drives differential growth and selection by an optimization principle. We performed *in vivo* measurements of the intraluminal angle between the OT and aortic sac in HH18, 21, and 24

chick embryos. We then investigated the influence of this angle on the growth of the HH18 AA using an optimization-based vascular growth model based on idealized anatomy of the three right lateral AA vessels. To accomplish this goal, we developed an inverse CFD coupled shape optimization framework to predict the great vessel vascular morphology *in silico* by evaluating multiple objective functions: hydraulic energy budget and particulate diffusive capacity. Integrating the *in vivo* AA morphometry data and computational modeling, we forecasted the progression of the embryonic AA development subsequent to HH18 and compared with the normal progression of AA development. We then evaluated the predicted AA geometries with reference to observed *in vivo* data and explored the implications of our model for investigating normal and aberrant cardiac morphogenesis. We finally proposed a theoretical model in which the change in OT orientation and a shift in objective function during development can guide the selection and growth of the AA.

3.2 Methods

3.2.1 *In vivo* measurement of the outflow tract-aortic arch angle

3.2.1.1 Fluorescent dye micro-injection

Fertilized white Leghorn chick eggs were incubated blunt end up at 37°C and 50-60% relative humidity to HH18, 21, and 24 (3, 3.5, and 4 days of incubation, respectively) (Hamburger and Hamilton, 1951). Between HH18 and 24, the cranial AA pair II gradually disappears and the more caudal AA pair VI emerges (Hiruma and Hirakow, 1995; Wang et al., 2009). Additionally, between these stages, cardiac looping progresses and the OT moves from a more rightward to a central position (Manner, 2000). As the OT is oriented cranially and towards the right of the

embryo during the investigated stages, only right side up embryos were utilized and all measurements were performed for the right lateral AA.

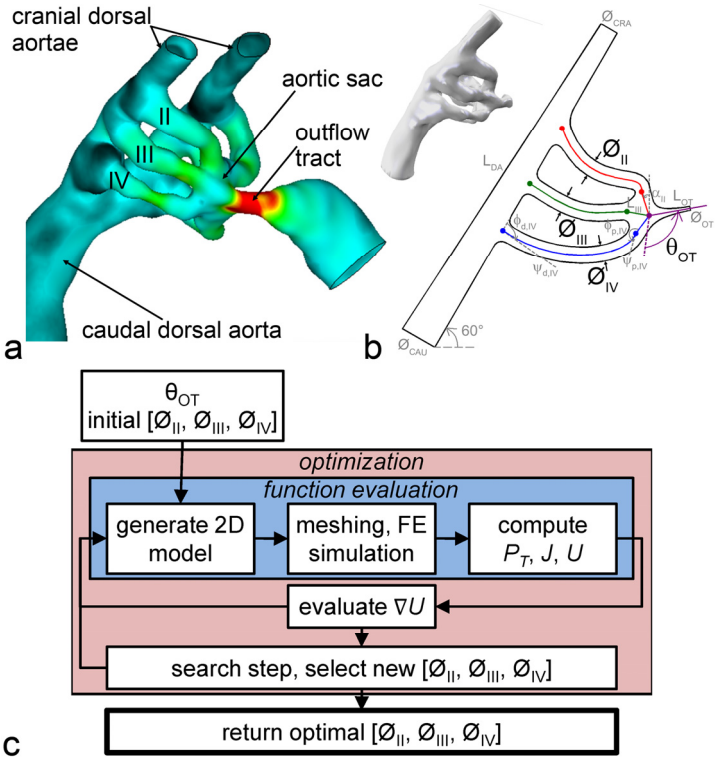

Figure 16. The model geometry used in the CFD-coupled optimization. (a) 3D polymeric cast of the HH18 AA, viewed from a dextro-ventral perspective. Right lateral AA are labeled II, III, and IV. Color indicates the WSS magnitude at peak flow velocity, ranging from 0 (deep blue) to 36 (red) Pa. Adapted from (Wang et al. 2009). (b) Parameterization of the HH18 right lateral AA model geometry. A 2D representation of the right lateral AA was generated from fluorescent dye microinjection and micro-CT reconstructions. AA diameters ($Ø_{II}$, $Ø_{III}$, $Ø_{IV}$) served as the optimization shape variables, with θ_{OT} as an additional anatomical parameter. The inset is a right lateral perspective of the 3D reconstruction for comparison with the 2D model. (c) A flow chart of the CFD coupled optimization framework used in this study. The framework returns the optimal diameter set for the θ_{OT} specified at the start. Abbreviations are defined in the text.

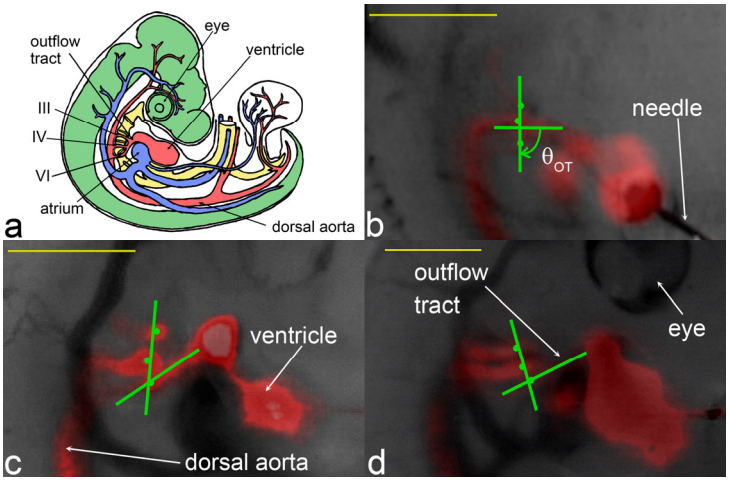

Figure 17. The angle of the OT relative to the aortic sac was measured using fluorescent dye injection. (a) Sketch of a HH24 chick embryo. Arterial vasculature is red and venous vasculature is blue. Green represents neuronal structures, yellow digestive. Adapted from (Patten 1920). (b), (c), and (d) Representative fluorescent dye injection and angle measurement of HH18, 21, and 24 chick embryos, respectively. Embryos are viewed from the right lateral, cranial is oriented toward the top. The proximal end of OT shifts cranially during these stages of embryonic development, increasing the angle. Scale bars are 1 mm.

Eggs were positioned under a stereomicroscope (Leica MZ16F and M165FC, Leica Microsystems GmbH, Germany) and the embryo was exposed by windowing the shell and removing the overlying membranes. Embryos that were dysmorphic or exhibited overt bleeding were rejected. Fluid microinjection was performed using a pulled and beveled glass capillary pipette (35 µm inner diameter, 30° bevel) connected via Silastic tubing to a disposable 22-gauge needle and a 10 µl glass Hamilton syringe, mounted on a three-axis micromanipulator. Fluorescent dye was injected at the ventricular apex and visualized using an external fluorescent light source (Leica EL6000, Leica Microsystems GmbH, Germany). Water soluble dyes Cy3.18 (excitation wavelength 550 nm, emission wavelength 565 nm) and Cy5-diethyl (excitation

wavelength 646 nm, emission wavelength 666 nm), diluted in phosphate buffered saline were chosen as most suitable to visualize flow streams (Mujumdar et al., 1993). Typical microinjection volumes ranged from 0.4 to 2 μl. Time-lapse movies of the flow streams through the OT and AA were recorded using a low light monochrome digital camera (Figure 17, Leica DFC 350FX, Leica Microsystems GmbH, Germany).

3.2.1.2 Measurement of the outflow tract-aortic arch angle

Still images were extracted from the fluorescent injection movies to measure the angle between the centerline of the distal region of the OT and the plane of the aortic sac. Using an *ad hoc* image processing tool developed in MATLAB (Mathworks, MA), the centerline of the OT was established by tracing the course of dye and the plane of the aortic sac was determined by fitting a line to the points of brightest intensity at the branching of the AA (Figure 17). The OT angle was defined as the caudal-most angle formed by the two intersecting lines. A total of 63 injections and measurements were performed (n = 23 HH18, n = 23 HH21, and n = 17 HH24). A student t-test was performed to determine the statistical significance of the variation in the OT position between the stages.

We performed a detailed analysis of micro-CT 3D reconstructions to justify the use of fluorescent injection and validate our methodology used to measure the OT angle. All fluorescent dye injections were performed *in ovo*, and although embryos were viewed from the right lateral, the orientation of the dorso-ventral and cranio-caudal axes may not be parallel to the microscope stage. The position of the OT, aortic sac, and AA was therefore not uniform across all samples. To determine an acceptable method for measuring the OT angle relative to the AA, we performed an analysis using 3D reconstructions of the HH18 AA manifold. A 3D polymeric cast of the HH18 AA was created and scanned using micro-CT as previously described (Wang et

al., 2009). The 3D cast was imported into Geomagics (Geomagic Inc., Durham, NC) and snapshots were obtained at various dorso-ventral and cranio-caudal orientations. A reproducible measurement of the OT to AA angle could be obtained by representing the aortic sac as a plane and calculating the relative angle of the OT. The aortic sac plane could be successfully established by connecting the branch points of the AA. Using this measurement method, we found that the range of measurement was within one standard deviation of the *in vivo* angle, supporting the independence of our measurement technique from the *in ovo* orientation of the embryo (Figure 18).

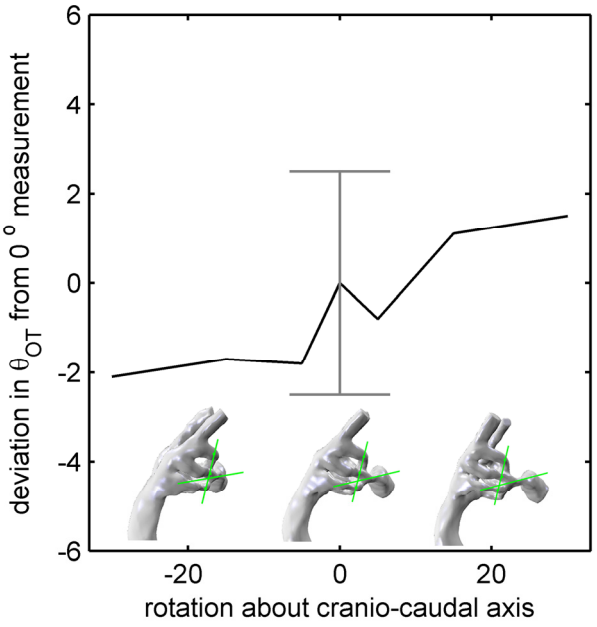

Figure 18. Test of the θ_{OT} measurement technique for various possible *in ovo* rotations about the cranio-cadual axis of the embryo. A 3D cast of the HH18 AA was positioned at different rotation angles and used to measure θ_{OT}. A 0° rotation was defined as a direct right lateral perspective. As the rotation angle changed, the measured θ_{OT} was slightly affected. However, this error was within ±1/2 the average standard deviation during experiment, indicated by error bars. This analysis demonstrates that distortion due to *in ovo* orientation of the embryo has a

negligible effect on our θ_{OT} measurement technique. Figure insets depict the 3D model at three rotation angles.

3.2.2 CFD coupled inverse shape optimization

3.2.2.1 Model construction and parameterization

Our CFD-coupled shape optimization framework was applied to an idealized 2D representation of the right lateral HH18 AA (II, III, and IV). The bulk shape and dimensions were extracted from the previous fluorescent dye injections and 3D micro-CT reconstructions and represented as a parametric geometry, extending from the distal region of the OT through to the dorsal aorta (DA) (Figure 16) (Wang et al., 2009). The OT was modeled as a straight tube with length (L_{OT}) and diameter ($Ø_{OT}$) of 250 μm and 50 μm, respectively. The DA was modeled a straight, tapered tube with length (L_{DA}), cranial diameter ($Ø_{CRA}$) and caudal diameter ($Ø_{CAU}$) of 2195 μm, 112.5 μm, and 225 μm, respectively, with the ventral wall at an angle of 60° to the horizontal. From the distal most point of the centerline of the OT, the branch point of each AA was defined by a vector with length (L_{II} = 150 μm, L_{III} = 135 μm, L_{IV} = 134 μm) and angle (α_{II} = 18° α_{III} = 80° α_{IV} = 143°), measured with respect to the vertical. The branch point is the most proximal point on the centerline of the AA, and together the three AA branch points define the plane of the aortic sac, as in the *in vivo* measurement. The end point of each AA, defined as the distal most point of the AA centerline, was chosen such that the distance from branch point to end point of AA III was 610 μm, and the line connecting these two points formed an angle of 100° with respect to the plane of the aortic sac. These values were determined based on measurements from the fluorescent dye injections and micro-CT reconstruction. The end points of AA II and IV were

defined by their distance from that of AA III, measured along the line of the ventral side of the DA.

Third order Bezier curves were used to connect AA branch points to end points, creating the centerline of each AA. The proximal anastomosis angle (φ_p) and length (ψ_p) defined the tangent vector at the aortic sac ($\varphi_{p,II} = 155°$, $\varphi_{p,III} = 190°$, $\varphi_{p,IV} = 200°$, $\psi_{p,II} = 150$ μm, $\psi_{p,III} = 200$ μm, $\psi_{p,IV} = 150$ μm) and the distal anastomosis angle (φ_d) and length (ψ_d) defined the tangent vector at the DA ($\varphi_{d,II} = 130°$, $\varphi_{d,III} = 95°$, $\varphi_{d,IV} = 95°$, $\psi_{d,II} = 450$ μm, $\psi_{d,III} = 400$ μm, $\psi_{d,IV} = 400$ μm). Angle φ_p was measured with respect to the line connecting the distal most point of the centerline of the OT to the AA branch point and angle φ_d was measured with respect to the line of the ventral side of the DA. The AA lumen was formed by extruding the vessels walls in the normal directions along the centerline. Third order Bezier curves were used to make smooth connections to the OT, DA, and between the AA. Values for the fixed shape parameters described here were manually determined by trial and error to obtain a qualitative agreement with right lateral views from the fluorescent dye injections and micro-CT reconstructions. $Ø_{OT}$ was chosen to maintain an inlet Reynolds number (Re) of 4, as observed in our previous HH18 CFD simulations (Wang et al., 2009). The 2D model in Figure 16 can be compared to the inset right lateral view of the micro-CT reconstruction in the same figure and to the images from the fluorescent dye injections presented in Figure 17 to observe its similarity to the right lateral AA.

During the shape optimization, the individual AA diameters, $Ø_{II}$, $Ø_{III}$, and $Ø_{IV}$, served as the inverse shape design variables. The angle of the OT relative to the aortic sac (θ_{OT}) was an additional input parameter. The generation of the geometric models was automated using an in-house subroutine that accepts the design variables as inputs. The geometry was created using FEMLAB (COMSOL Inc., Burlington, MA) internal shape commands, which allowed for

seamless interaction between the model construction, meshing, and flow simulation. To translate the 3D tubular geometry to 2D, the input diameters were treated as hydraulic diameters, and the corresponding width of a rectangular channel was assigned as the model diameter. Model parameterization and translation of a 3D geometry to 2D has been implemented previously by our group (Dur et al., 2011). Limitations of our model related to the simplification to 2D are discussed later (§3.4.6).

3.2.2.2 Numerical simulation of blood flow and species transport

The 2D incompressible Navier-Stokes and passive-scalar transport equations were modeled over the right lateral AA domain using the commercial finite element (FE) solver FEMLAB (COMSOL Inc., Burlington, MA). This solver uses the Petrov-Galerkin formulation and has been validated for 2D flow (Hanke, 2004). A steady-state solution was chosen as our previous pulsatile CFD simulations revealed that the Womersley number was less than 1 within the AA, suggesting that a steady solution is sufficient (Wang et al., 2009). Flow was modeled using a rigid walls assumption, and blood was treated as a non-Newtonian power-law fluid, $\mu = m\dot{\gamma}^{n-1}$, where μ is the apparent viscosity, $\dot{\gamma}$ is shear rate, m = 0.017 Pa^n, and n = 0.708 (Shibeshi and Collins, 2005). Although the AA may distend during flow, our past experience indicates that wall motion is minimal and would be a negligible factor in this study. We use viscosity parameters for adult blood as there is limited data for the embryo. A steady parabolic flow profile was specified as the inlet boundary condition, with the average velocity corresponding to one-half the average flow rate over the cardiac cycle for the HH18 chick (0.44 mm^3/s) (Yoshigi et al., 2000), since only one side of the symmetric AA was modeled. The OT diameter and velocity profile maintain an inlet Re of 4, which was measured from our previous work (Wang et al., 2009). A pressure boundary condition was specified at both the cranial and caudal DA

outlets. The reference pressure at the caudal end was 120 Pa (0.9 mm Hg), equal to measured DA pressures (Hu and Clark, 1989; Yoshigi et al., 2000). The cranial pressure was then adjusted during the each inner iteration automatically to provide the desired physiological caudal/cranial flow split of 90/10.

Diffusion of a passive species (generic paracrine factors or oxygen) was subsequently modeled, using the velocity field from the flow simulation to solve the convective diffusion equation. A unit normal concentration of 1 mm^{-3} was supplied as a boundary condition along the walls of the AA vessels, with zero concentration at the OT and a zero diffusive flux boundary condition on all other boundaries. A diffusion coefficient (D) of 1.0 x 10^{-4} cm^2/s was set as constant. This large diffusivity was chosen so that both energy and diffusion were of the same order of magnitude to simplify the optimization routine. The geometry was discretized using an unstructured tetrahedral mesh, consisting of approximately 4000 elements for grid independency with a minimum quality > 0.5. Six levels of grid refinement were used to verify grid independency of the objective functions.

The model construction, meshing, CFD simulation, and post-processing were all automated in a single modularized function, which accepts inputs of the design variables and outputs the objective function. The utility of coupling CFD to inverse shape optimization was demonstrated previously by our group as a pre-surgical planning tool to improve patient-specific coronary artery bypass graft designs (Dur et al., 2011).

3.2.2.3 Multi-objective optimization problem

The automated CFD framework described above was coupled to a multi-objective shape optimization algorithm to achieve the optimum set of AA diameters over a range of θ_{OT}. The two-element objective vector consisted of the total power to sustain blood flow (P_T) and the total

diffusive exchange capacity (J) of the AA domain. Minimization of energy is an established principle of vascular form (Gruionu et al., 2005; Kassab and Fung, 1995; LaBarbera, 1990; Murray, 1926; Pries et al., 1995; Sherman, 1981; Taber, 1998c; Zamir, 1977), while maximizing diffusive capacity is derived from the homology of the AA in lower order vertebrates where terminal AA pairs are the precursor of gill vasculature (§ 3.4.4).

The total power to sustain blood flow in the system (Eq. 1) is comprised of the linear combination of three components: the power to 1) drive the flow of blood (P_f), 2) maintain the metabolic cost of blood volume (P_b) and 3) maintain the metabolic cost of the vessel wall (P_w) (Taber, 1998c). Formulas for these three components are given in (Eqs. 2, 3, and 4), respectively, where u is the velocity field, p is the pressure, ρ is the density, Ø is the vessel diameter, L is the vessel length, and T is the wall thickness. The subscripts *ot*, *cra*, and *cau* stand for the OT inlet and cranial and caudal DA outlets, respectively.

$$P_T = P_f + P_b + P_w \tag{1}$$

$$P_f = \int_{ot}\left(p + \frac{\rho \boldsymbol{u}^2}{2}\right) * \boldsymbol{u} \cdot \hat{n} dS - \left(\int_{cra}\left(p + \frac{\rho \boldsymbol{u}^2}{2}\right) * \boldsymbol{u} \cdot \hat{n} dS + \int_{cau}\left(p + \frac{\rho \boldsymbol{u}^2}{2}\right) * \boldsymbol{u} \cdot \hat{n} dS\right) \tag{2}$$

$$P_b = \pi \frac{\varnothing^2}{4} L \alpha_b \tag{3}$$

$$P_w = 2\pi \frac{\varnothing^2}{4} L\left(\alpha_w \frac{T}{\varnothing} + \beta_w fp_{walls}\right) \tag{4}$$

In (Eq. 3), α_b is a metabolic constant for blood, while α_w and β_w in (Eq. 4) are the passive and active metabolic constants for the wall, respectively. Values for these constants vary significantly among species and vessel types; in (Zamir, 1977), α_b has a range of 5 to 5000 W/m^3. For all calculations in this study, values of 1700 W/m^3, 4000 W/m^3, and 0.433 s^{-1} were

used for α_b, α_w, and β_w, respectively. In (Eq. 4), f, the active fraction of the total fiber stress, was assumed to be 1 and $T/Ø$, the ratio of wall thickness to diameter, was fixed at 0.05.

Diffusive capacity was quantified as the total diffusive uptake between the inlet at the OT and DA outlets (Eq. 5), where c is the concentration and other notations are as above. As a unit normal concentration was applied along the AA walls, J has a maximum value of 1.

$$J = \left(\int_{cra} c * \boldsymbol{u} \cdot \hat{n} dS + \int_{cau} c * \boldsymbol{u} \cdot \hat{n} dS \right) - \int_{ot} c * \boldsymbol{u} \cdot \hat{n} dS \tag{5}$$

Optimization was performed using the sequential quadratic programming (SQP) method (MATLAB, Mathworks, MA). SQP achieves efficient evaluation of constrained optimization problems by attempting to solve for the Lagrange multiplier directly (Schittowski, 1985). At each major iteration, the search direction is obtained by solving a quadratic sub-problem based on quadratic approximation of the Lagrangian. The following optimization problem was posed:

$$\min U\left(\boldsymbol{F}\left(\boldsymbol{G}(\boldsymbol{s}), \boldsymbol{s}\right)\right) \tag{6}$$

where:

$$U(\boldsymbol{F}) = \left(w_1^2 \left| \frac{P_T - P_T^o}{P_T^o} \right|^2 + w_2^2 \left| \frac{J - J^o}{J^o} \right|^2 \right)^{1/2} \tag{7}$$

$$P_T^o = \min P_T\left(\boldsymbol{G}(\boldsymbol{s}), \boldsymbol{s}\right) \tag{8}$$

$$J^o = \max J\left(\boldsymbol{G}(\boldsymbol{s}), \boldsymbol{s}\right) \tag{9}$$

$$w_1 + w_2 = 1 \tag{10}$$

$$\boldsymbol{F}\left(\boldsymbol{G}(\boldsymbol{s}), \boldsymbol{s}\right) = \begin{bmatrix} P_T\left(\boldsymbol{G}(\boldsymbol{s}), \boldsymbol{s}\right) \\ J\left(\boldsymbol{G}(\boldsymbol{s}), \boldsymbol{s}\right) \end{bmatrix} \tag{11}$$

$$\boldsymbol{G}(\boldsymbol{s}) = \begin{bmatrix} \boldsymbol{u}(\boldsymbol{s}) \\ p(\boldsymbol{s}) \\ c(\boldsymbol{s}) \end{bmatrix} \tag{12}$$

$$\boldsymbol{s} = \begin{bmatrix} \varnothing_{II} \\ \varnothing_{III} \\ \varnothing_{IV} \end{bmatrix} \tag{13}$$

subject to:

$$\rho(\boldsymbol{u}\cdot\nabla)\boldsymbol{u} = \nabla\cdot\eta\left(\nabla\boldsymbol{u} + (\nabla\boldsymbol{u})^{T}\right) - \nabla p \tag{14}$$

$$\nabla\cdot\boldsymbol{u} = 0 \tag{15}$$

$$D\nabla^{2}c = \boldsymbol{u}\cdot\nabla c \tag{16}$$

$$\boldsymbol{s}_{l} \le \boldsymbol{s} \le \boldsymbol{s}_{u} \tag{17}$$

In the above problem, ***s*** denotes the shape design variables (the AA diameters) and ***G(s)*** and ***F(G(s),s)*** refer to the CFD solution (where ***u*** is the velocity field, p is pressure and c is concentration) and multi-objective functions, respectively. Weighted global criterion scalarization (Collette and Siarry, 2003; Marler and Arora, 2004) was used to solve the multi-objective problem (Eq. 7), where $U(\boldsymbol{F})$ represents the scalar objective function and the reference point $\left(P_T^o, J^o\right)$ was chosen such that P_T is minimized and J maximized. Optimization is subject to upper and lower bound constraints on the design variables, denoted as $\boldsymbol{s}_u$ and $\boldsymbol{s}_l$, respectively. A lower bound of 10 μm AA diameter was enforced rather than implementing AA disappearance in order to maintain a continuous objective function and an upper bound of 180 μm was given to avoid errors in overlapping AA vessels. We interpret an AA converging to the minimum allowed diameter as disappearing.

3.2.3 Framework algorithm

The framework algorithm is summarized in Figure 16. First, θ_{OT} and the initial state ***s*** are used to generate the starting geometry. Model construction, meshing, FE simulation, and post-processing are run in series to evaluate the objective functions at the current diameter set ***s***. This function evaluation loop is executed for sequential changes in each diameter to determine the gradients of the scalar objective function U. Gradients are used to compute the step size, and the updated diameters are fed to the function evaluation loop, repeating the above process. The optimization loop terminates when a minimum is located, returning the optimal diameters for the θ_{OT} defined at the start. For the present study, a ∇U of less than 10^{-7} was sufficient for optimization. The entire process was repeated for each θ_{OT}.

To assess the effects of the relative contributions of energy and diffusion on AA morphology, optimizations were performed for three P_T/J weighting ratios: 50/50, 65/35, and 100/0. The final ratio, 100/0, refers to a mono-objective optimization, where only total energy utilization is minimized. In the remaining text, we refer to the multi-objective cases as "power + diffusion optimization" and the mono-objective as "power – only optimization". We also tested the effect of the caudal/cranial outlet flow split by conducting the 65/35 case with a 50/50 prescribed split. The simulations with different flow splits did not produce significantly different results (data not shown).

We performed preliminary simulations to examine the behavior of each objective function and determine our initial condition. The diameter of one AA was systematically incremented while keeping the other two at a fixed, equal value. Five diameters were tested, ranging from 10 to 150 μm, and the process was repeated for the same five diameters applied to the two fixed AA (Figure 19). The P_T gradient was steep for small diameters, but quickly

decayed to approach a shallow minimum. This minimum is the result of the inverse relation between the gradients for P_f and P_b and P_w; the larger P_f gradient at small diameters drives an increase in AA caliber, which is eventually suppressed due to the larger blood and vessel wall volume. Over the [$\boldsymbol{s_l}$, $\boldsymbol{s_u}$] interval in this study, the effects of P_f dominate and AA vessels approach or reach the maximum allowed diameter to achieve minimum energy. The gradient for J behaved similarly, though not as steep as P_T. The maximum value of J is limited to 1, given the unit normal concentration at the AA walls, which is approached as all three AA diameters near zero. Thus, no maximum is obtained on the given [$\boldsymbol{s_l}$, $\boldsymbol{s_u}$] interval, and J acts to reduce vessel caliber. We ran a single variant optimization, with all AA diameters equal, for θ_{OT} of 97° and P_T/J of 50/50 and used the resulting diameter (95 μm) as the initial condition for all AA. We tried several other initial conditions, including two small caliber AA and one large and two large AA and one small, and found that starting with three AA of equal diameter consistently converged to a global optimum, and that the 95 μm uniform AA diameter tended to converge with the fewest function evaluations. In addition, several tolerances for the ∇U required for termination of the optimization were tried, and we found that stricter values (i.e. $< 10^{-7}$) did not significantly influence the final diameters.

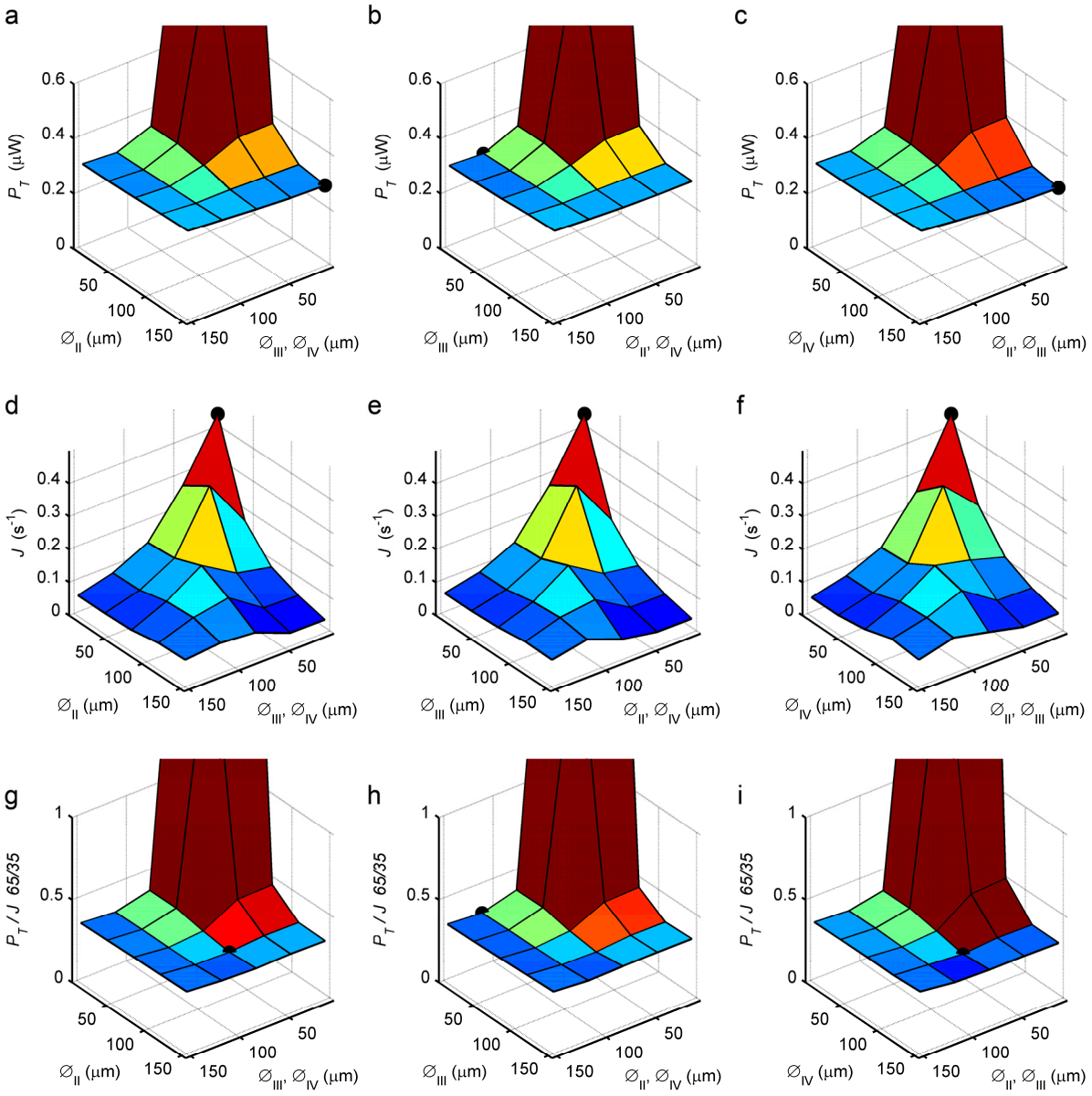

Figure 19. Behavior of objective functions P_T, J, and U with respect to a single diameter change. One AA diameter was systematically increased with the remaining two held constant. (a, b, c) Variation in P_T for increasing AA II, III, and IV, respectively. (d, e, f) Variation in J for increasing AA II, III, and IV, respectively. (g, h, i) Variation in scalar objective function U for P_T/J = 65/35 for increasing AA II, III, and IV, respectively. Black markers indicate the minimum P_T, maximum J, or minimum U. θ_{OT} of 97° was kept constant.

3.3 Results

3.3.1 *In vivo* angle measurements

Embryonic heart looping can significantly alter the distribution of blood flow through the multiple pairs of AA vessels. Quantification of the orientation of the OT relative to the AA using fluorescent dye injection revealed an increase in the angle as the proximal end shifted cranially (Figure 17). Mean angles ± standard deviation were calculated as 96° ± 3° for HH18, 116° ± 6° for HH21, and 117° ± 6° for HH24. A student t-test indicated a statistically significant difference ($p < 0.001$) between HH18 and 21, but not between HH21 and 24 (Figure 17), consistent with the fact that the cardiac looping process is largely completed by HH21.

Morphogenetic events from HH18 to 24 include movement of the OT from a right lateral to a more centrally located position (Manner, 2000; Patten, 1920). Our measurements indicate that this motion causes a further shift in the OT-AA angle as the proximal end of the OT moves toward the cranial pole of the embryo (Figure 17), as was qualitatively observed earlier in polymeric casts of the embryonic AA system (Wang et al., 2009).

3.3.2 Aortic arch patterning for power and diffusive capacity objective functions

Adaptive growth of the AA was explored using the power + diffusion optimization based on the ratio between P_T and J; analyses were conducted for two P_T/J ratios: 50/50 and 65/35. Both cases indicated that three patent AA vessels provide a balance between reducing energy consumption and increasing diffusion. For the P_T/J = 65/35, θ_{OT} was a determining factor in selecting which of the three AA had the largest diameter, i.e. the dominant AA. For smaller θ_{OT} the dominant AA is predicted as AA II, whereas for larger θ_{OT} AA IV was dominant (Figure 20). When the contribution of P_T and J were equivalent, AA configuration showed minor dependence on θ_{OT}, with similar AA diameters predicted for each angle (Figure 21). The dependence of AA

patterning on θ_{OT} suggests that the orientation of the OT has a significant role in directing the growth of that specific AA which is in line with the centerline of the OT.

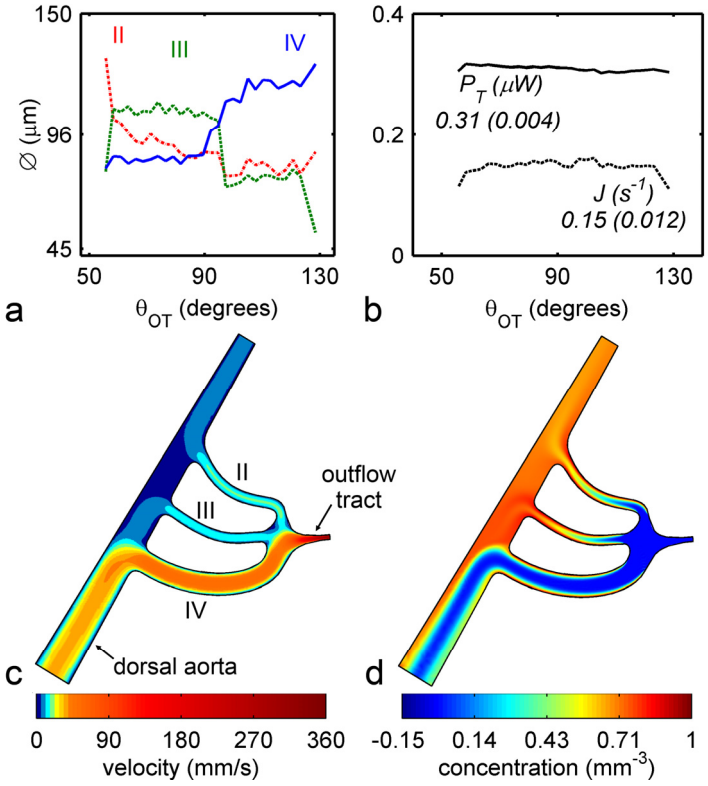

Figure 20. Power + diffusion optimization with P_T/J of 65/35 converged to a multiple AA configuration, however the dominant AA was highly dependant on θ_{OT}. (a) The optimal diameter set for each θ_{OT} for P_T/J of 65/35. AA dominance changed from the AA II for θ_{OT} < 58°, to the AA III for 58° < θ_{OT} < 95°, to AA IV for θ_{OT} >95°. All AA remained patent. (b) Behavior of P_T and J over all optimizations. Labels indicate the mean (standard deviation). (c) and (d) The velocity and concentration fields, respectively, for θ_{OT} of 102° and P_T/J of 65/35.

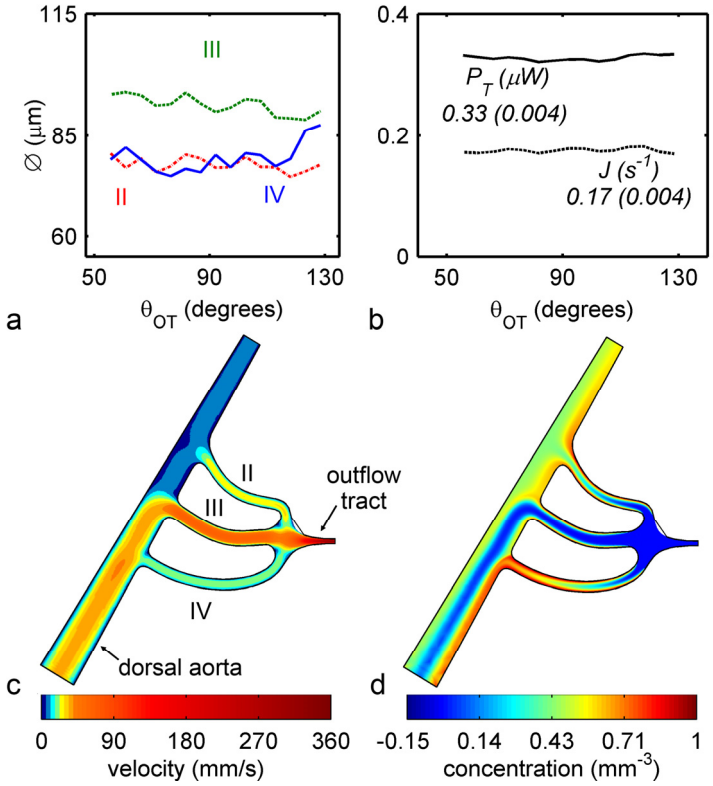

Figure 21. Power + diffusion optimization with P_T/J of 50/50 revealed that three AA vessels balance energy utilization with diffusive capacity. (a) The optimal diameter set for each θ_{OT}. AA III remained dominant for all angles, with AA II and IV remaining patent. (a) Behavior of P_T and J over all optimizations. Labels indicate the mean (standard deviation). (c) and (d) The velocity and concentration fields, respectively, of the optimal geometry for θ_{OT} of 97°.

3.3.3 Aortic arch patterning for power minimization only

We also examined the case where minimization of power acted as the sole objective function (P_T/J = 100/0). Unlike the multi-AA configurations resulting from a balance between P_T and J, minimization of P_T alone transformed the multi-AA manifold to a single AA geometry, where the remaining two AA converged to the minimum allowed diameter (10 μm). Further, the selection of the single AA displayed strong dependence on θ_{OT} (Figure 22), similar to the effect

of θ_{OT} in the power + diffusion case (§3.3.2). Total energy utilization was reduced by 10% compared to the 65/35 P_T/J ratio.

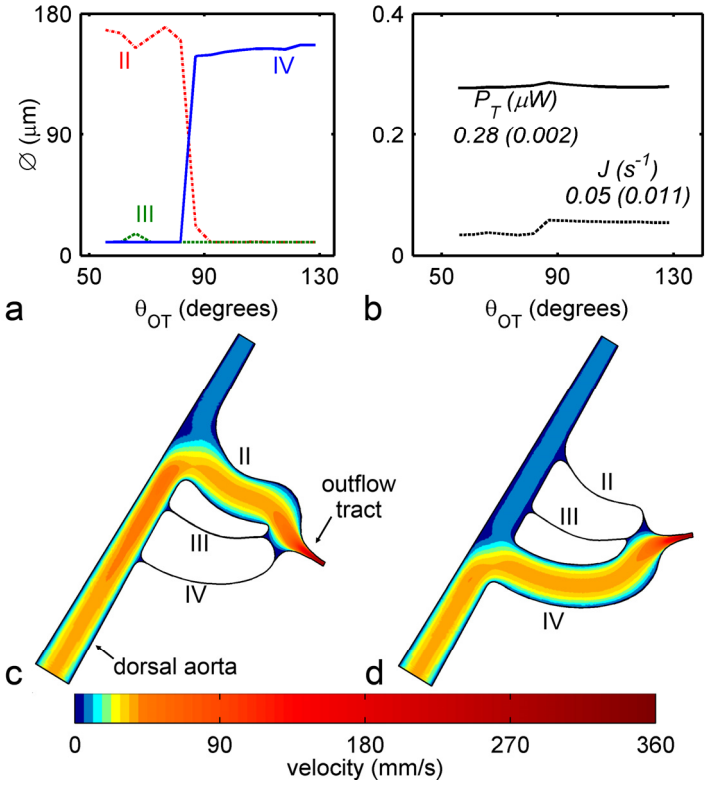

Figure 22. Power – only optimization (P_T/J = 100/0) converged to a single AA geometry. θ_{OT} was influential in selecting the dominant single AA. (a) The optimal diameter set for each θ_{OT}. Two configuration zones were observed: AA II dominant and AA IV dominant, with the transition occurring at θ_{OT} = 84°. (b) Behavior of the sole objective function, P_T and J over all optimizations. Labels indicate the mean (standard deviation). (c) and (d) Velocity fields for AA II dominant, θ_{OT} = 66,° and AA IV dominant, θ_{OT} = 108°, zones, respectively.

To verify that global minima of the total energy expenditure was achieved at the single AA state, independent of the initial AA configuration, two single-variant optimization problems were conducted with 1) three AA of the same diameter, and 2) a single AA. For the single AA

configuration, the design parameters and variables remained unchanged, with the exception that the diameters of AA II and IV were held to 0. Thus, the geometry of AA III was used to model the single AA configuration. A single variable, $s = \emptyset_{AA}$ in (Eq. 13), was used to model two cases. Minimizing total energy (P_T/J = 100/0) demonstrated that, while both cases led to the same total cross sectional area, the optimal single AA case reduced energy utilization by 12% compared to the optimal multi AA case (Figure 23). This relation is consistent with fluid mechanics, which indicates that for equal cross sectional area, the total resistance of three vessels in parallel is greater than that of a single vessel, leading to larger pressure drops.

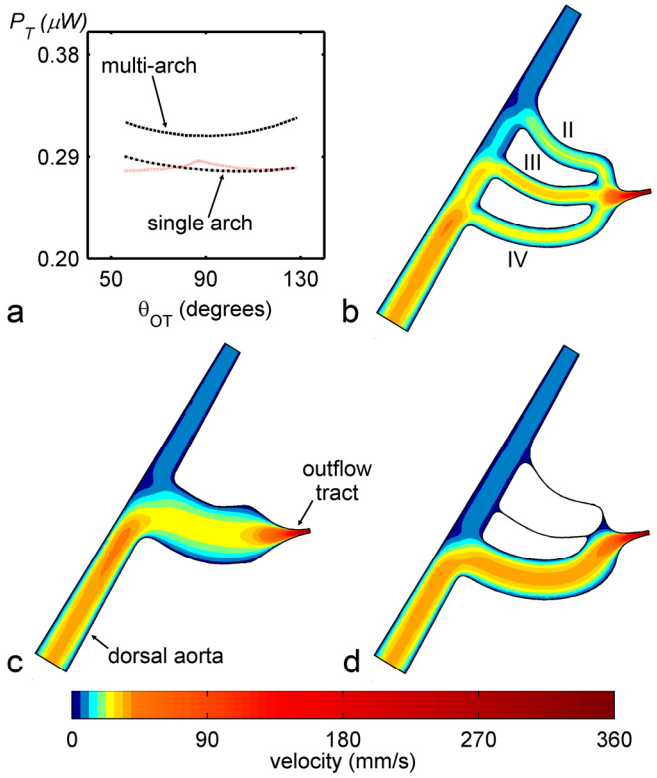

Figure 23. Results of the single-variant, power – only optimization. (a) Total energy for the optimized geometries. The energy utilization of uniform diameter multi AA case was 12% higher that that for the single AA case, confirming that a single AA vessel connecting the OT to the DA is the most energy efficient. The red dashed line represents the results of the multi-

variant optimization. The total energy is similar to the single AA case, again supporting convergence to a single vessel. (b) and (c) The velocity fields for the uniform diameter multi AA (b) and single AA (c) cases, respectively, $\theta_{OT} = 108°$. (d) Velocity field from the muti-variant optimization.

The optimization histories for sample 65/35 and 100/0 P_T/J ratios are shown in Figure 24. In both cases, there was an initial period of large diameter changes, lasting for 30-40 iterations. After this period, the diameters tended to stabilize remaining relatively constant. The initial period can be characterized as a search for the dominant AA, with the later iterations determining its optimal diameter. Although the final minimum is shallow, the initial search is associated with steeper gradients, which only level off once the dominant AA is found. This trend suggests that selection of the dominant AA is a strong impulse, while subsequent changes to its diameter are less well defined. Given the SQP method used, it is possible that the dominant AA selected by our model was a saddle point and not the true global minimum. Based on our results, we expect three such saddle points, with each AA as being dominant. To verify independence from the initial condition we also performed optimizations for a subset of θ_{OT}, where we began with an initial condition of one AA at the maximum diameter and the remaining two at the minimum. The largest AA was varied so that all three possible initial conditions were tested. In most cases, the geometry converged to the same as our original results. There were a few cases, however, where the initialized dominant AA did not change. Comparing to our original results revealed these to be saddle points, and in all cases, our original initial condition converged to the global optimum.

The results of the power + diffusion and power – only optimizations demonstrate that maximizing diffusive capacity drives smaller and smaller diameters, while minimizing power results in one large vessel. Imposing both objectives produces a compromise configuration as the influence of diffusive capacity prevents any AA from constant enlargement and energy expenditure inhibits diameter reduction. As the relative importance of one objective increases, its effects are amplified, as seen in the 50/50 and 65/35 P_T/J cases. We also performed power + diffusion optimizations for 70/30, 75/25, and 80/20 ratios for a subset of θ_{OT}. We found that, for the vast majority, the single AA configuration was optimal. These additional ratios demonstrate that a single AA is required to reduce the total power below a certain value. We performed optimizations only for these specific P_T/J ratios to maintain a manageable number of FE simulations. The 65/35 ratio was reached by manual trial and error to match our previous HH18 diameter data (Wang et al., 2009).

Both the power + diffusion and power – only optimizations converged to within a small range of P_T and J for each θ_{OT} (Figure 20, Figure 22). This trend suggests that a global optimum may exist, and that the AA morphology attempts to reach this value by re-patterning the AA diameters as θ_{OT} changes. The adaptive growth as a response to hemodynamic perturbations in order to restore a preferred (optimal) state is previously described as the hyper-restoration theory (Beloussov, 2008; Taber, 2009). These findings therefore support the idea that a change in the angle of the OT can provide a stimulus for AA development.

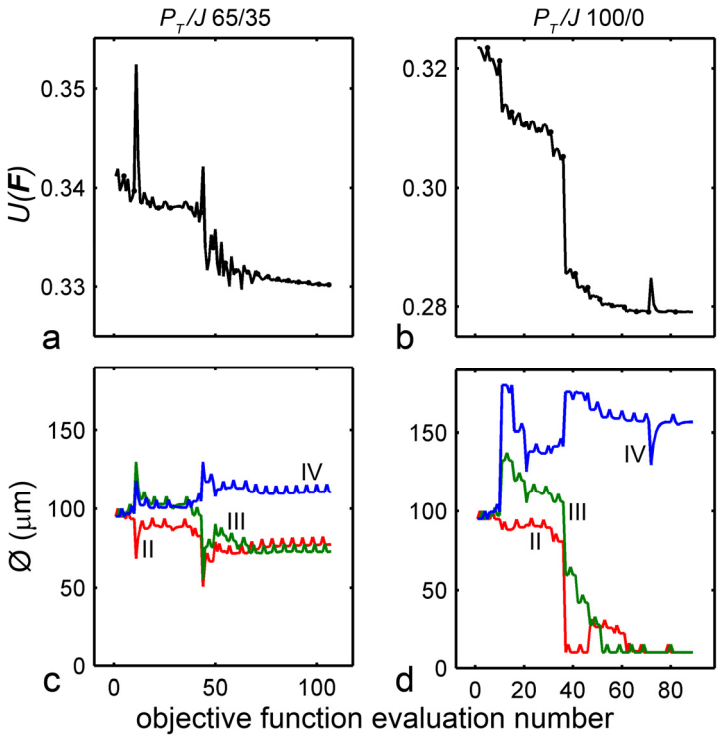

Figure 24. Optimization history of scalar objective function *U(F)* and diameter variables for P_T/J 65/35, θ_{OT} 97° (a and c) and P_T/J 100/0, θ_{OT} 123° (b and d). Once the optimal dominant AA is found, AA diameters stabilize as the minimum is approached.

3.4 Discussion

3.4.1 Orientation of the outflow tract determines the dominant aortic arch in the developing embryo

We found that, for all optimal AA configurations, one AA vessel must be larger in diameter than the other two, which we designate as the dominant AA (Figure 20, Figure 22). Further, the selection of the dominant AA was dependent on θ_{OT}, suggesting a significant role of vessel orientation in AA patterning. According to our previous (Wang et al., 2009) and current *in vivo* measurements and optimization based growth predictions, a P_T/J ratio of 65/35 allows good correlation between the model and observed AA morphogenetic events, with predicted AA

diameters within one standard deviation of the *in vivo* data reported in our previous work (Wang et al., 2009). AA dominance changed from AA II to AA III and finally to AA IV as θ_{OT} increased (Figure 20). The dominant AA III predicted for θ_{OT} near the measured angle of HH18 (96 ± 3°) is consistent with our previous *in vivo* measurements (Wang et al., 2009). Minor deviations from quantitative agreement between measured diameters and angles may be associated with modeling the 3D symmetric anatomy in one lateral (§ 3.4.6). As θ_{OT} increased during development, the dominant AA shifted to AA IV, which is supported by previous studies on AA growth (Hiruma and Hirakow, 1995) (Figure 20). Transitions in AA dominance occurring across the HH18, 21, and 24 angles is consistent with the dynamic AA patterns observed at HH21, the intermediate stage between the II, III, IV configuration of HH18 and III, IV, VI state of HH24, as discussed in Chapter 1. The excellent correlation between the model and experimental data for the P_T/J ratio of 65/35 suggest that at HH18, the AA balance energy utilization and diffusive capacity, similar to the optimized capillary tree network structure of microcirculation (Kamiya et al., 1987; Kamiya et al., 1993).

When minimizing energy alone (P_T/J = 100/0), the change in AA dominance as a function of angle change was sharper, creating a single AA geometry as the remaining two vessels regressed completely (Figure 22). In this trend two configurations were observed: AA II dominance and AA IV dominance, with the transition occurring at around θ_{OT} = 84° (Figure 22). The dependence of the dominant AA on θ_{OT} seems to be influenced mainly by the minimization of energy, consistent with the hypothesis that energy dissipation at the aortic sac drives the selection of the dominant AA. From the fluid mechanics perspective, the rapid expansion of the narrow OT into the aortic sac generated a jet flow regime that propagates several vessel diameters downstream towards the AA (Figure 20, Figure 22) (Wang et al., 2009). The angle of

the OT may dictate the pathway of the jet flow within the aortic sac and direct cardiac output preferentially towards one of the AA. This jet direction can result in selection of the dominant AA that lies on the flow pathway and thus dissipates the minimum energy. Although flow should be directed towards AA III for $\theta_{OT} \sim 90°$, a dominant AA III is never observed when minimizing energy alone. This may be due to the low Reynolds flow (inlet Re = 4) that creates a tendency for blood to adhere to the walls of the OT and aortic sac and thus flowing toward the outermost AA II and IV. Studies at higher Re numbers are needed to verify this idea.

3.4.2 Change in objective function, competition among parallel aortic arches may drive convergence to a single aortic arch

The results of the power + diffusion and power – only optimization pathways reveal that embryonic AA selection can be characterized similar to the competing collateral arterial vessels. Examining a simple network of two parallel vessels, Keenan and Rodbard demonstrated that vascular adaptation to WSS alone causes one vessel to enlarge and the other to disappear (Keenan and Rodbard, 1973). In their model, vessel caliber increased or reduced to restore "optimal" WSS conditions, effectively minimizing total energy. Small perturbations in the distribution of blood flow leads to the dilation of one vessel due to increased WSS and constriction of the other due to reduced WSS. The change in resistance caused more flow to the larger vessel and less flow to the smaller, creating positive feedback loop, which eventually led to a single vessel. This dynamic vessel competition has also been demonstrated in the adaptation of larger microvascular networks, where WSS maintenance led to rarefaction to a single vessel (Hacking et al., 1996; Hudetz and Kiani, 1992). Our methodology for the power – only optimization follows these previous models, as the number of AA reduces to one. In our model,

the change in θ_{OT} is the source of the flow perturbation, preferentially selecting the dominant AA.

Other dynamic models of microvascular adaptation have shown that applying metabolic controls in addition to WSS can result in stable, multi-vessel networks that closely match the *in vivo* topology. Using a 1D mathematical model, Pries et al. introduced metabolic demand for O_2 as an additional parameter for the control of vessel diameter (Pries et al., 1998). When applying both WSS and metabolic controls, a stable network was achieved, whereas WSS alone again resulted in instability and rarefaction. The target WSS level in this model was not constant as in (Keenan and Rodbard, 1973), but varied according to transmural pressure, as suggested by (Pries et al., 1995) and incorporated into our model through vessel wall maintenance (Taber, 1998c). Applying their model to more complex networks demonstrated that convergence to the *in vivo* topology could only be obtained by enforcing both WSS and metabolic controls (Pries et al., 2001). Their results indicated that the functional requirements of vascular systems are of equal, and possibly greater, importance as WSS in regulating vessel diameter. This multi-stimuli approach is similar to our power + diffusion model, which generated a stable, multi-AA configuration. Our CFD-coupled optimization also revealed that the higher dimensional geometry and flow field can influence vessel morphology.

Minimization of energy accurately predicted that the multi-AA geometry will converge to a single vessel, derived from AA IV (Barry, 1951; Hiruma and Hirakow, 1995). While the reduction to a single vessel to reduce energy is a well-established phenomenon (Keenan and Rodbard, 1973), our novel CFD-coupled optimization based model demonstrates that θ_{OT} is an important factor in selecting the dominant AA due to its role in distributing blood flow. Our power + diffusion simulations suggest that the multi-AA configuration is due to functional

objective functions such as metabolic demand. Based on these results, we propose a theoretical model in which the change in OT orientation and a shift in objective function during development guide the selection and growth of the AA (Figure 25). However, it is also possible that the emergence of multiple AA is the result of phylogenetic selection, driven by the genetic code. Later convergence to the single vessel may then simply be the adaptation of the AA network to minimize energy. As new AA arise due to inherent genetic expression, those that are placed in a more advantageous position due to θ_{OT} (i.e. AA IV) enlarge at the expense of the already existing AA. This type of dynamic instability is characteristic of a competition among the AA, with θ_{OT} dictating the "winner". Additional research into the formation of new AA will be required to address these issues.

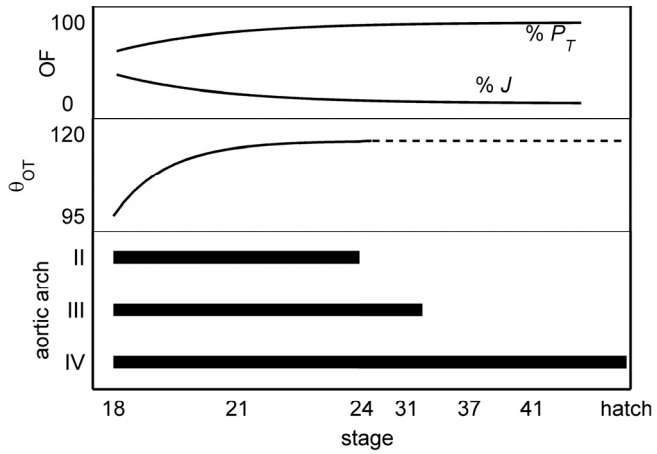

Figure 25. Proposed model for the behavior of AA objective functions over development and the effect on AA growth. The relative importance of energy (% P_T) increases, while that of diffusion (% J) reduces, as the foundations for aerial respiration develop. The bottom panel shows the time for which each AA exists as a connection to the descending aorta. The increase in θ_{OT} selects the dominant single systemic AA. The combination of both the variation in objective function and change in OT orientation leads to the AA IV derived adult arch of aorta.

The time axis is skewed to highlight the early stages of development investigated in the current study.

3.4.3 Abnormal orientation of the outflow tract may lead to defects in aortic arch growth and selection

Classical descriptive morphologic studies have long suggested that the migration and rotation of the OT is a critical factor in great vessel development (Bremer, 1928; Congdon and Wang, 1926) and errors in OT location and orientation are frequently associated with congenital heart disease. In his experiments on chick embryos, Bremer speculated that the "descent" of the heart into the thorax results in significant torsion of the OT, which is translated to the AA, causing obliteration of some AA due to mechanical force (Bremer, 1928). This torsion was explicitly implicated in the growth of AA pair IV, where the counter-clockwise axial rotation of the OT causes twisting and bending of the left lateral AA IV, leading to its obliteration. Disruption of the normal leftward rotation of the embryo and dextral looping of the heart by various surgical manipulations resulted in abnormal patterning of the AA, including a persistent left AA IV and aberrant derivatives of AA III. Similar results were obtained by Gessner (Gessner, 1966), where the OT in HH19 chick embryos was displaced and made immobile by inserting a surgical wire. AA defects involved deviations from the normal AA derivatives, such as disappearance of AA IV and the definitive arch of aorta formed by AA III (both laterals were observed), absence of the left lateral of AA VI with the left pulmonary artery formed from the right lateral, and a double aortic arch. Our proposed model is consistent with these findings in the literature and further establishes the role of OT orientation in selecting the dominant arch of aorta. We

anticipate such surgical manipulations of OT position to alter the hemodynamic environment and selection of the optimal dominant AA, generating these abnormal patterns.

While substantial progress has been made in defining critical genes and proteins associated with normal OT and AA morphogenesis, the molecular mechanisms that determine changes in cell proliferation, differentiation, and matrix remodeling involved in asymmetric AA selection and remodeling have yet to be identified Targeted gene studies in mice have shown that *splotch* and *Pitx2* are necessary for normal OT rotation (Bajolle et al., 2006; Liu et al., 2002). Defects in these genes result in arrested rotation and produce AA phenotypes similar to those observed by Bremer, including double aortic arch and randomization in laterality of the dominant arch of aorta. However, *Pitx2* positive cells are not found in the AA themselves, indicating that it does not have a direct role in asymmetric AA morphogenesis (Liu et al., 2002; Yashiro et al., 2007). Rather, it is believed that the arrested OT rotation in *Pitx2* mutants disrupts the distribution of cardiac output to the AA, leading to abnormal hemodynamics that alter WSS sensitive signaling pathways such as PDGFR and VEGFR2 (Yashiro et al., 2007). While these studies have primarily examined the lateral asymmetry of AA pair IV, our model suggests that a similar mechanism may exist in the selection of the dominant AA from the set of all six AA pairs.

Though not directly related to OT orientation, several other studies have validated the effects of altered flow patterns on AA malformations and growth. Unilateral vitelline vein ligation in the chick embryo results in abnormal intracardiac flow patterns, incomplete looping resulting in double outlet right ventricle, and redistributes flow to the individual AA vessels (Hogers et al., 1999; Rychter and Lemez, 1965). These changes in blood flow are associated with a variety of AA defects, including hypoplastic right brachiocephalic artery, interrupted

aortic arch, double aortic arch, and hypoplastic pulmonary artery (Hogers et al., 1999). Reducing left ventricle volume by left atrial ligation also causes abnormal perfusion of the AA vessels (Hu et al., 2009). AA anomalies such as absent AA III and IV, and AA hypoplasia have been described. These studies provide ample evidence that irregularities in the OT-AA angle generate altered flow patterns in the embryonic AA and cause defects in the formation of the great vessels.

Many of the aberrations observed in these studies are relevant to known congenital defects. It is worth noting that tetralogy of Fallot, transposition of the great arteries, and double outlet right ventricle associated with heterotaxy syndrome can be associated with an abnormal aortic-to-pulmonary valve axis, which occurs as the result of morphogenetic errors in OT orientation (Bostrom and Hutchins, 1988; Lomonico et al., 1988). Aortic arch hypoplasia is normally associated with hypoplastic left heart syndrome, a severe defect requiring multiple palliative surgeries over the patient's lifetime and has the highest mortality rate of any birth defect in patients less than one year of age (Roger et al., 2011). Fetal intervention in humans attempts to restore normal biomechanical loading to recover normal growth and remodeling of the developing fetal heart and vasculature, but the optimal timing for such intervention to remains unknown (McElhinney et al., 2010; Pekkan et al., 2008a; Pekkan et al., 2008b; Pekkan et al., 2008c).

3.4.4 Diffusive capacity as an objective in early development is supported by comparative anatomy of the aortic arches

Imposing diffusive capacity as an early primary objective function for AA growth may not be apparent as all diffusion activity occurs through the skin during early embryo development. Additionally, the size of the AA, each on the order of 100 μm at HH18, 21, and 24 (Wang et al.,

2009) is too large to allow substantial diffusion and implicates these vessels as conduits for bulk transport. However, our analysis of diffusive capacity as an optimization objective relates to the morphogenesis of the gill arches in lower order vertebrates rather than to suggest a diffusion function for the avian AA at HH18.

The ontogeny of the AA has long been a hallmark of comparative anatomy, demonstrating clear phylogenetic patterns and illustrating the evolution of the arterial system as the gas exchange medium transitioned from water to air (Kardong, 2009; Liem et al., 2001). Unlike the chick and human, in fish the embryonic symmetric pattern of the AA persists into adulthood as these vessels form the afferent and efferent branchial arteries that feed and drain the gills (Evans et al., 2005; Hughes and Morgan, 1973). The resulting pattern of multiple branchial arteries, each feeding several hundred filaments creates a gas exchange organ highly efficient in extracting oxygen from the surrounding water (Hughes and Morgan, 1973; Piiper, 1982). It is speculated that hypoxic environments drove the transition from water to air as the external gas exchange medium; a transition, which produced changes in AA growth (Evans et al., 2005; Kardong, 2009; Liem et al., 2001). It is worth noting that the number of persistent AA as well as gill surface area is reduced in fishes that are obligate air breathers (Brauner et al., 2004; Hughes and Morgan, 1973). In addition to gas exchange, the gills provide other vital functions including ionoregulation, acid-base regulation, and the removal of metabolic waste (Evans et al., 2005).

These diffusion-dependent functions of piscine AA derivatives suggest that the pattern of these vessels is meant to maximize diffusive capacity by increasing the number of capillary beds between the heart and DA. Although the AA vessels themselves do not actively participate in diffusive exchange, the stimulus to grow and remain patent may be driven by an optimization principle. This same stimulus would then be present in the early embryonic chick AA vessels,

decreasing during the course of development as the foundations for aerial respiration form. Thus, the emergence of multiple AA early in development is driven by a balance between energy budget and diffusive capacity, while the later development of the single systemic arch of aorta is the result of minimization of energy alone (Figure 25). This evidence from comparative anatomy initiated our choice of diffusive capacity as an objective function and seems to support our model of optimization-based AA growth.

3.4.5 Utility of optimization-based growth models

While principles such as Murray's law of energy minimization during vasculogenesis seem to correlate well with observed anatomy, the fundamental relations that govern embryonic morphogenesis, or more generally biological systems, have not been completely determined (Taber, 2009). With regards to the vascular system, it is well established that the local mechanical environment is sensed by multiple cell lineages including endothelial cells, but the translation of this local information with respect to complex, global 3D vascular lumen shape adaptation and cellular responses remains under investigation. Both biomolecular pathways and mechanical factors play an important role in this process, likely governed through complex mechano-genetic feedback. The underlying cardiovascular biology that drives the topological and structural alterations is significantly different in disease, normal embryonic growth/development, and acute/chronic adaptation. For each case, once the governing biology is well understood, the computational framework to predict fluid-tissue interaction can quantify the relative degree of mechanical and genetic contributions to the observed modes of vascular shape alterations. Recently, a number of such growth models with varying degrees of complexity have been applied to predict diseased cerebral aneurysm development (Li and Robertson, 2009; Watton et al., 2009) and angiogenesis (McDougall et al., 2002; Sun et al., 2005), but limited

studies are devoted to normal embryonic growth response. Local growth rules proportional to the various fluid-induced loading indices, including the WSS sensitivity, need to be tested and compared to the *in vivo* measured 3D surface reconstructions. Linear vessel diameters can be statistically correlated with WSS indices (Dur et al., 2009), and would be a starting point to quantify complex 3D association.

Through the present optimization-based growth modeling approach presented here and substituting CFD-coupled applied shape optimization for integrative growth laws (Alford et al., 2008; Taber, 1998b; Taber and Eggers, 1996), we are able to determine gross morphologic variations. Unlike dynamic models of vascular adaption (Pries et al., 1998) and solid mechanics based growth and remodeling simulations (Gleason and Humphrey, 2004; Taber, 1998b), our method cannot determine the intermediate steps of the growth pathway. *In vivo* information of microstructural architecture or employing constitutive biomechanical relationships (Holzapfel et al., 2000; Holzapfel and Ogden, 2010) would augment the present approach. The present modeling strategy can also be adapted to incorporate other structurally motivated growth and remodeling principles by posing new objective functions and can incorporate variations in cardiac function through the fluid boundary conditions. Based on established physiologic optimization principles (Baba et al., 1995; Kamiya et al., 1987; Kamiya et al., 1993; Murray, 1926; Taber, 1998c), our model was able to predict AA lumen diameters within one standard deviation of reported values (Wang et al., 2009) and forecast future morphogenetic events including dominant AA selection remarkably well. The performance of our model represents an encouraging first step towards an alternative paradigm in fluid-coupled arterial growth and remodeling.

3.4.6 Study Limitations

3.4.6.1 Energetic cost of metabolic maintenance

When computing the total energy expenditure, calculating both the metabolic cost of blood volume and the metabolic cost of the vessel wall involve the use of metabolic constants (Eqs. 3 and 4). Reported values for these constants vary greatly for different species (Taber, 1998c; Zamir, 1977). Although some trends do exist, such as an inverse relation with animal size (Taber, 1998c), the choice for the values of these constants was hindered by available literature data. Limited information on the composition and metabolic requirements of embryonic blood and energetic cost of vascular growth prohibit sufficient estimation of these parameters. The values used in our model are within the reported physiologic range, however future studies would be required to determine precise values.

3.4.6.2 2D geometry vs. 3D aortic arch manifold

Although the model geometry used in this study is based on reconstructions of the HH18 AA, the simplification to 2D neglects the complex 3D flow and pressure fields of the true anatomical shape (Wang et al., 2009). For example, in the embryo, the AA emerge as paired structures surrounding the foregut, with large AA curvatures, which are not captured in our planar model. Additionally, while we have examined the effects of the cranio-caudal shift of the OT, the lateral movement and axial rotation cannot be investigated in 2D and may play a similar role in shaping the AA (Bremer, 1928). Extending our optimization framework to 3D would improve the predictive capabilities and allow further investigation into AA development. However this will also increase the computational cost quite significantly.

3.5 Conclusions

We have shown that hemodynamic changes associated with OT orientation due to cardiac looping can influence the growth and selection of the embryonic AA. Measurement of the angle of the OT relative to the aortic sac revealed a statistically significant shift between HH18 and 21, a critical point during cardiovascular development. The optimization-based growth model demonstrated that this change in angle re-patterns the individual AA diameters and accurately predicts the mature AA IV dominance over development. A multi-objective optimization that balances energy utilization with diffusive capacity modeled the physiologic HH18 AA diameters well, while a minimization of energy alone converged to the adult single systemic aortic arch. Additional research will require extension to 3D modeling and investigation of the cellular and molecular mechanisms responsible for maintaining/achieving optimal function.

Chapter 4

Quantification of global and local vascular morphogenesis using long-term OCT imaging of the chick embryo

4.1 Introduction

Over the past half-century, the advancement of imaging technology and explosion of computer resources have made imaging one of the most important tools in medical diagnosis and scientific research. In embryology, these tools have enabled detailed studies of tissue and organ morphogenesis, providing a greater understanding of these events. Techniques such as traditional microscopy, serial tissue sections, and scanning electron microscopy (SEM) have been used to produce various 2D and 3D descriptive atlases of cardiovascular development in the chick (Al Naieb et al., 2012; Manner, 2000; van den Berg and Moorman, 2011). However, quantitative imaging is lacking, and as more techniques are created to intervene in cardiovascular development and generate defects, the morphometric consequences remain difficult to discern. Some modalities, such as tissue sections and SEM, may not provide reliable quantitative data as they require dehydration of samples, which can shrink and distort tissues. Imaging studies using micro-computed tomography (micro-CT) introduced polymeric casting of the cardiovascular system and the contrast agent osmium tetroxide, both of which were suggested to result in minimal to no disruption of tissue morphology (Butcher et al., 2007; Kim et al., 2011). These techniques required fixing the embryo and therefore only obtained static 3D images. Live micro-CT of chick embryos has been demonstrated, but has had limited use to date (Henning et al., 2011). Magnetic resonance microscopy (MRM) has been used to image live quail embryos and chick embryos HH24 or greater *in ovo*, though the large cost of this technique has prevented

widespread implementation (Bain et al., 2007; Holmes et al., 2009). In recent years, optical coherence tomography (OCT) has emerged as a preferred method for live imaging of the chick embryo (Davis et al., 2008; Manner et al., 2008; Yelbuz et al., 2002). OCT is non-invasive and the 4 μm resolution is on the scale of micro-CT (1-25 μm) and greater than MRM (30 μm) (Kim et al., 2011; Yelbuz et al., 2002; Zhang et al., 2003). The imaging depth of OCT is limited to approximately 1 mm in the chick embryo, which makes it unsuitable for applications beyond HH18; even at HH18, OCT gives an incomplete view of the heart.

Live imaging of the embryo offers several advantages, including: 1) it avoids damage to the tissue caused by fixation methods, 2) it allows observation and quantification of dynamic structures, such as the beating heart, and 3) the same embryo can be imaged multiple times to quantify tissue morphogenesis or track cell populations. Several studies have used the live imaging capabilities of OCT to examine the dynamics of the embryonic heart using 4D reconstructions (Gargesha et al., 2009; Manner et al., 2008; Rugonyi et al., 2008) and obtain blood flow velocity with Doppler-OCT (Davis et al., 2009; Ma et al., 2010). Many of these studies were conducted at room temperature, which can affect cardiac function in the embryo (Davis et al., 2009; Manner et al., 2008; Rugonyi et al., 2008). Early research demonstrated that the embryonic heart rate is highly dependent on temperature (Pickering, 1893). Therefore, several researchers have constructed incubation chambers to maintain physiologic environmental conditions while imaging (Al Naieb et al., 2012; Gargesha et al., 2009; Happel et al., 2011; Kulesa et al., 2010; Ma et al., 2010; Orhan et al., 2007). Most live imaging studies have been performed at a single time-point (Davis et al., 2009; Gargesha et al., 2009; Ma et al., 2010) or at several discrete time-points over a long duration (Bain et al., 2007; Henning et al., 2011; Holmes

et al., 2009). The incorporation of environmental chambers allows continuous or near-continuous long-term imaging (>5 hours) to capture morphogenesis in real-time.

Long-term imaging of the chick embryo has been combined with both confocal microscopy to track moving cell populations over a period of more than 26 hours, in 1.5 minute intervals (El-Ghali et al., 2010; Kulesa et al., 2010) and OCT to measure cardiac function over a 6 hour period, in 60 minute intervals (Happel et al., 2011). A confocal system has been developed for long-term imaging of the zebrafish embryo as well, capable of a 5 day period, in 10 minute intervals (Kamei and Weinstein, 2005). None of these time-lapse, long-term studies have performed quantitative analysis of morphogenesis. Shell-less or *ex-ovo* culture systems are often used in long-term studies (El-Ghali et al., 2010; Happel et al., 2011; Teddy et al., 2005), though an *in ovo* confocal protocol has been proposed (Kulesa et al., 2010). In the case of zebrafish embryos, immobile mutants or tricaine anesthetized embryos are used (Kamei and Weinstein, 2005). Shell-less culture has been associated with changes in heart rate and developmental delay compared to *in ovo* embryos (Auerbach et al., 1974; Yelbuz et al., 2000). To address these issues and provide morphometric data of the developing vascular system at high temporal resolution, we have created a time-lapse, long-term imaging system, based on OCT, with environmental control for quantitative morphogenetic analysis of the chick embryo *in ovo*.

We applied our system to quantify the growth of a vitelline artery over a 10 hour period beginning at HH16, acquiring a 3D volume scan every 60 minutes. Our results demonstrate that the artery cross section is elliptical and tapers slightly over its length. Mean radial growth increased linearly over the 10 hour period. We further computed local radial growth, which revealed areas of outward growth (enlargement) and inward growth (reduction), demonstrating that the radius does not change uniformly. The remainder of this chapter describes our

environmental chamber and OCT system, the 3D reconstruction method, extraction of vessel parameters, and computation of local growth vectors. Finally, we discuss how our technique can be used to understand the regulatory mechanisms and principles of vascular morphogenesis.

4.2 Methods

4.2.1 Embryo preparation

Fertile white Leghorn eggs were incubated at 37°C and 60-70% relative humidity to HH16 (2.3 days). Eggs were then windowed to gain optical access to the embryo. Prior to beginning the time-lapse OCT imaging, we inspected embryos under a stereomicroscope for bleeding and dysmorphic features. At the conclusion of the 10 hour imaging period, we again examined the embryo for abnormalities (Figure 26).

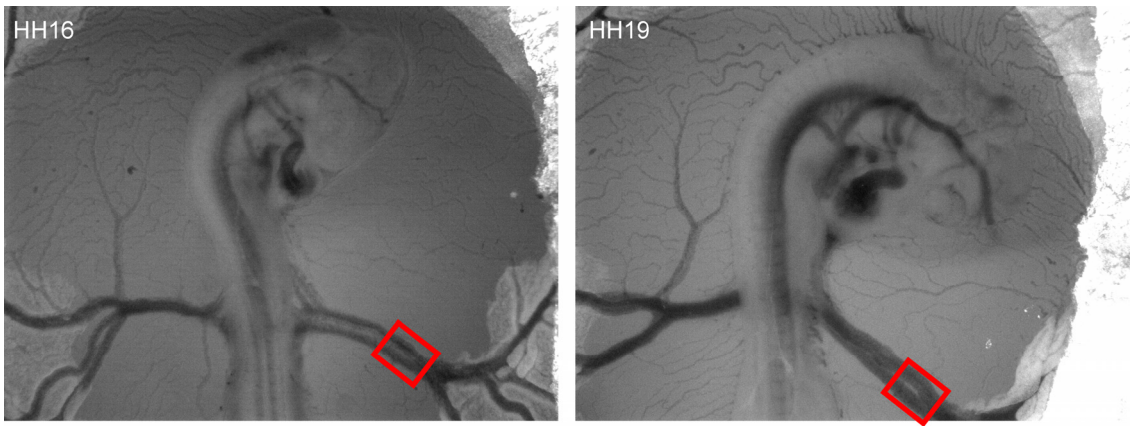

Figure 26. The embryo before (HH16) and after (HH19) the 10 hour imaging period. The scan location of the vitelline artery is shown in the red box.

4.2.2 Environmental chamber

For long-term live imaging of chick embryos, we constructed an environmental chamber around our OCT system to maintain physiologic temperature and humidity conditions (Figure 27). The

chamber was custom built by our lab. We used acrylic to form the basic chamber structure, fastened together with aluminum angle brackets. Sealant was applied to the internal junctions of the chamber walls and ceiling. Two doors provide access to position the embryo or move the OCT probe. Adjustable circular vents were placed on the lower right and upper left walls to provide airflow. A 150 mm computer fan was mounted to the inner right wall to circulate air within the chamber. We selected a 250 W heat lamp as the heat source after ceramic heaters proved unreliable and disruptive. The heat lamp was connected to a digital thermostat controller, which measured temperature via a probe placed near the embryo (STC-1000, Elite Electronics, China). The temperature can be set within 0.1°C and maintained within ±1° accuracy. We calibrated the temperature controller settings using an analog thermometer placed within the chamber. Temperature was kept at 38°C. Humidity was maintained between 60-70% using an ultrasonic nebulizer (Walgreens, Deerfield, IL). The heat lamp and fan were powered through an IEC C13 power cord while the humidifier had a separate power cord. The chamber measures 48 cm wide by 53 cm deep by 56 cm tall.

A major issue with previous long-term imaging studies was desiccation of the embryo and vitelline membrane as water evaporated from the exposed surface of the egg (Happel et al., 2011). We found that bridging the gap between the egg and imaging probe (2.5 cm) with a section of corrugated tubing prevented desiccation and allowed long-term survival of embryos (Figure 27). We tested embryos up to 48 hours and observed no developmental delays when compared with eggs incubated in a traditional force-draft incubator. Our OCT system included a live feed CCD video, which allowed us to monitor the status of the chick embryo while inside the chamber.

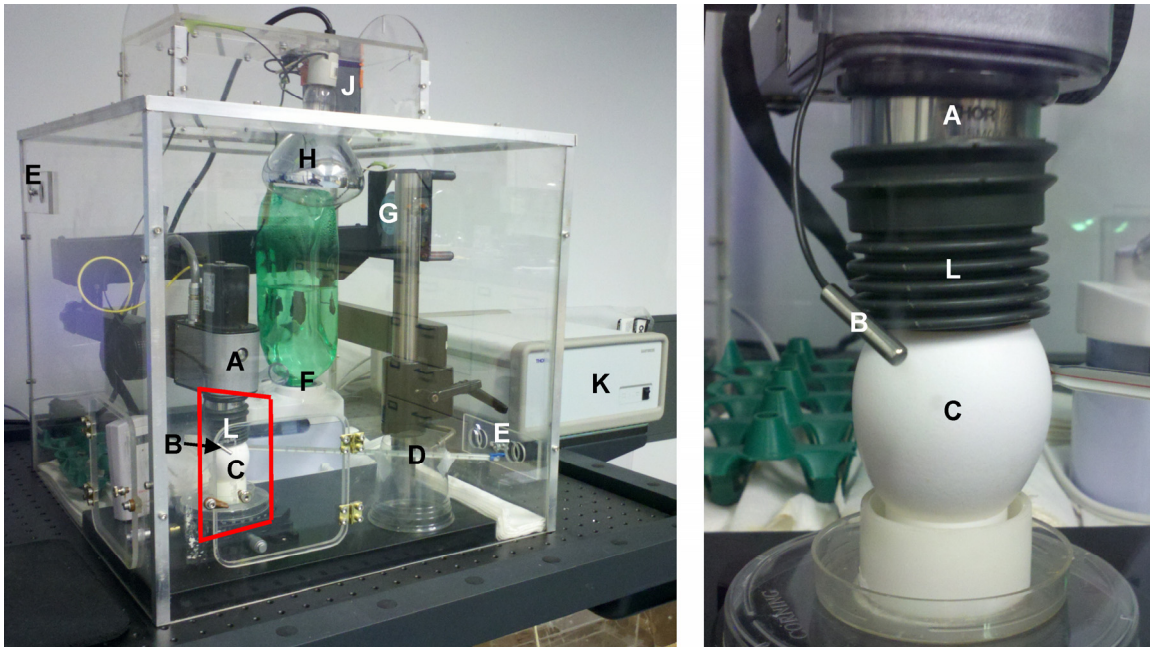

Figure 27. The environmental chamber surrounding our OCT system. A heat lamp (H) regulated by a digital temperature controller (J) maintains a 38°C environment and an ultrasonic humidifier (F) keeps humidity at 60-70%. A fan (G) circulates air through the chamber while vents (E) allow air flow to and from the ambient room climate. The temperature sensor (B) is positioned near the egg. A close-up view of the area marked by the red box is shown in the right panel. A section of corrugated tubing (L) bridges the gap between the egg (C) and OCT scan probe (A) to prevent desiccation. D – analog thermometer, K – OCT base unit.

4.2.3 OCT acquisition

We used a spectral domain (SD) OCT system (Thorlabs Spectral Domain Ganymede, Thorlabs, Inc., NJ) to acquire noninvasive, *in vivo* images of the chick embryo (4.3 μm resolution). OCT is an echo-based modality, which uses low-coherence interferometry to measure the axial distance of back-reflected light (Huang et al., 1991). The OCT light source is comprised of a 930 nm center wavelength (λ) superluminescent diode with a spectral bandwidth ($\Delta\lambda$, FWHM) of 100

nm. The 930 nm source is within the 600-1300 nm "therapeutic window" for optical radiation, while the total optical power on the sample was 1.5 mW, producing no thermal damage (Berlien and Müller, 1997; Boulnois, 1986; Parrish, 1981). Sensitivity of the OCT system defines the minimum detectable change in index of refraction and was measured experimentally to be 91 dB (manufacturer specification). The theoretical axial resolution depends on the coherence length of the OCT light source, and is expressed as $2\ln(2)\lambda^2/\Delta\lambda\pi n$, where n is the refractive index of the sample medium (Fercher et al., 2003). In SDOCT, the design of the spectrometer and signal processing both affect the actual resolution. The spectrometer used in our OCT system can image a spectral range (δ) of 150 μm, while the OCT software applied Hann-windowing of the spectrum to give smooth axial point-spread functions. The actual axial resolution of our system was $\lambda^2/(\delta n)$, equivalent to 5.8 μm in air and 4.3 μm in water. Lateral resolution is set by the minimum waist radius of the focused OCT beam, which in our system was 15 μm. The spectrometer used in our OCT system consisted of a 12 bit high-sensitivity CCD camera with 2.0 μm pixel spacing. A pair of x- and y-galvo-controlled mirrors within the scan head moves the position of the A-line during scanning. Data was transferred in real-time over a GigE connection to a PC with a 3.3 GHz processor. The maximum A-scan rate of our OCT system was 29 kHz. The rate of data transfer produced an actual recorded frame rate of 32 fps for a 494 A-line image (15.8 kHz). The sample refractive index is defined for the medium surrounding the sample and was considered 1.33 for *in ovo* embryo imaging.

We designed a custom software interface to control the OCT system for automated time-lapse imaging (LabVIEW, Austin, TX). At a set interval, a 3D volume comprised of multiple B-scans is recorded. Our coordinate system was such that the x- and y-directions were parallel to the surface of the egg and the z-direction was depth into the egg. A-scans were swept in the x-

direction, and the B-scan thus lay in the xz-plane. The volume is therefore composed of multiple xz slices. In the software, the user sets the scan width (x displacement) of the B-scan and then positions the first slice within the volume by adjusting the x- and y-galvos while live streaming the B-scan. The scan length (y displacement) is then set by positioning the last B-scan in the volume. The user then inputs the number of A-lines per B-scan and the number of slices. The scan depth (z displacement) and z-pixel spacing are predetermined by the OCT system. The scan interval is then selected and the first volume scan is initiated. At each slice (y-position), multiple B-scans are recorded, creating a movie. The absolute time of each B-scan is recorded so time intervals between B-scans or slices can be computed. Once the entire volume has been saved, the galvos return to the position of the first slice. The process is repeated automatically based on the interval set by the user. This OCT acquisition is summarized in Figure 28. The number of B-scans per slice and refractive index of the sample are also set by the user. For the current study, we imaged a vitelline artery for 10 hours, at 60 minute intervals beginning at HH16, totaling 11 volume scans (Figure 26). The scan settings are summarized in Table 9. We positioned our B-scan to obtain a longitudinal section through the vessel (Figure 28). In general, the x-direction aligned with the vessel axis, and the yz-plane contains the vessel cross section. Prior to the start of each volume scan, we adjusted the position of the embryo and OCT scan probe to account for drift. We used anatomical landmarks to re-establish the volume limits, using the previous B-scans as a guide. This process helped to ensure that we scanned the same region each time.

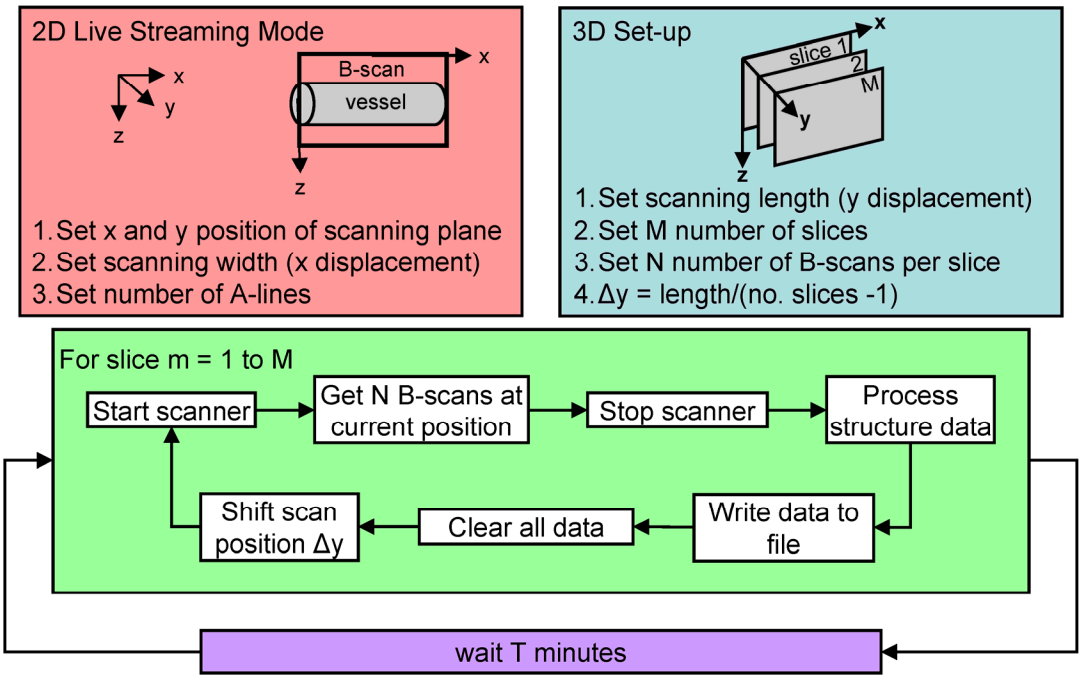

Figure 28. Flow chart describing the automated OCT data acquisition.

Table 9. Scan settings used during long-term imaging.

refractive index	depth (mm)	z pixels	width (mm)	A lines	length (mm)	slices	B-scans per slice	T (min)
1.33	2.074	1024	1.001	494	0.703	116	16	60

4.2.4 Reconstruction of 3D vessel geometry

Segmentation of OCT data requires specialized algorithms due to low signal to noise ratio compared to contrast MRM or micro-CT (Kajic et al., 2013; Pilch et al., 2012; Yousefi et al., 2013). We applied the active shape model technique to segment the vitelline artery in our OCT data (Pilch et al., 2012). This method combines a statistical shape model with regional intensity similarity to segment axial vessel cross-sections. All codes were written in MATLAB (version R2011a, Mathworks, Natick, MA). For each slice, we first took an intensity average of all B-scans. We combined these average B-scans to create a 3D volume array with one intensity value

per voxel. We then rotated our data 90° about the z-axis so that our slices were in the yz-plane and contained the axial cross-sections. Slices in which cross-sections were incomplete or unidentifiable were removed, cropping the data in the x-direction. Data was also cropped in the z-direction to remove everything below the artery and create a smaller dataset. To create the statistical shape model, we manually identified the vessel boundary in 20 cross-sectional slices evenly distributed along the axial direction. For each slice, the manually selected boundary points were fit to a piecewise polynomial curve, which was resampled at 100 evenly spaced landmark points ordered in a counter-clockwise direction. These boundary shapes were then used to build a statistical shape model as described by Pilch et al. (Pilch et al., 2012).

Beginning with the first manually segmented yz-slice, the statistical shape model was fit to the manually identified boundary points. At each of the 100 landmarks, the intensities of the surrounding 20 by 20 pixel area was recorded. For the next unsegmented slice, the statistical shape model was positioned at the centroid from the previous slice and its landmark points were incrementally shifted to maximize the correlation between the surrounding 20 by 20 pixel area and the pixel are recorded at the same landmark point in the previous slice. These pixel displacements were then applied to the statistical shape model to compute the cross-section boundary. This process was repeated for a slice range of ± one half the slice interval between manually segmented cross-sections. Thus, each manually segmented cross-section was combined with the statistical shape model and local intensities to create the active shape model for the neighboring slices. Once each cross section boundary had been determined, pixels inside the boundary were given a value of 1 and pixels outside a value of 0. Combining all of the segmented slices together created the binary 3D volume.

From the binary 3D volume, we created a tetrahedral mesh to obtain the surface of the artery (Fang and Boas, 2009). The mesh was exported as a stereolithography (STL) file and imported into Geomagic Studio 10 (Geomagics, Inc., Durham, NC) to apply our smoothing protocols (Dur et al., 2011). The process was repeated for each of the 11 volume scans.

4.2.5 Morphometric analysis

We computed global and local vascular growth from the reconstructed 3D vessels. For each vessel, we first determined the centerline based on the surface mesh vertices. Beginning at the centroid of the vertices, we determined the coordinate and tangent vector of the centerline using an optimization approach. For a given vector **a** originating at the centroid $\mathbf{p}_0$ and defined in spherical coordinates (θ, φ), we collected all of the vertices v such that $\left|(\mathbf{p}_v - \mathbf{p}_0)\cdot\mathbf{a}\right| \le h$, where $\mathbf{p}_v$ is the coordinate of vertex v and h is a height of a cylinder (15 μm in this study). All points $\mathbf{p}_v$ were projected onto the plane defined by point $\mathbf{p}_0$ and normal vector **a**. An ellipse was fit to the projection of $\mathbf{p}_v$, and the root mean square (RMS) value of the fit ellipse was reported. This sequence was set as an optimization problem, with objective function RMS and variables θ and φ. In effect, we found the best fit cylinder at the point $\mathbf{p}_0$. The centerline coordinate was therefore the centroid of the best fit cylinder and the tangent vector was **a**. Once the centerline coordinate was found, we moved it along its tangent line 20 μm to define the new $\mathbf{p}_0$ and repeated the process. After the entire vessel had been traversed, we had obtained a set of centerline coordinates. The coordinates were fit to a piecewise polynomial spline, giving the centerline of the vessel. We found that an elliptical fit was best suited for our data, and the optimal RMS values were approximately $7\text{x}10^{-6}$.

The cylindrical fitting approach produced the best fit ellipse for multiple positions (typically 45) along the vessel length. These elliptical fits provided some characteristic

information about the vessel, including radial tapering and cross-section eccentricity. The mean major and minor radii were also computed, giving a single parameter to describe the vessel size. We examined the trend in mean radii over the entire 10 hour imaging time to quantify global growth.

To estimate the morphometric error, we performed our 3D OCT acquisiton, segmentation, and reconstruction techniques using a vessel phantom consisting of a nylon filament submerged in water (Stren Original 4 lb monofilament fishing line, Pure Fishing, Inc., SC). The expected uniform radius was 101.5 μm, measured with a micrometer, and the expected cross-section eccentricity was 1.0. The mean radius measured with our OCT-based method was 104 μm ± 2.8 μm standard deviation (SD) over the vessel length. The mean error is thus 2.5%, or 2.5 μm, which is below the resolution of our OCT system, validating our measurements. The mean eccentricity was 1.26 ± 0.01, which indicates that the eccentricity of our vascular cross sections was over estimated. This over estimation occurs because the lateral margins of a circular or elliptical cross section are obscured as the height of the refractive boundary at these regions drops to below the OCT resolution. Therefore, the horizontal axis of the cross-section tends to be underestimated when using OCT. Indeed, the minor axis is always oriented perpendicular to the OCT probe. Additional steps to correct for this underestimation can be added to future reconstruction methods.

In order to quantify local growth, we first applied a morphing algorithm to transform the vessel at time t into the vessel at time $t+T$. Vessels were translated such that the y- and z-coordinates of midpoint of their centerlines were both 0. The x-coordinate was retained, since the cropping during segmentation would cause poor alignment. For each vertex of the surface mesh of vessel t, the corresponding centerline coordinate was computed such that $(\mathbf{p}_v - \mathbf{c}) \cdot \mathbf{u} = \mathbf{0}$,

where **c** is the centerline coordinate and **u** is the tangent vector at **c**. For each point **c** on the centerline of vessel t, the closest point **c′** on the centerline of vessel $t+T$ was then determined. In this manner, the centerline of vessel t was transformed into the centerline of vessel $t+T$. At each point **c**, there exists the orthogonal bases vectors **u**, **v**, and **w**. Base vectors **v** and **w** were found by computing the rotation for **u** to become $\hat{\mathbf{k}}$ and applying the inverse rotation to $\hat{\mathbf{i}}$ and $\hat{\mathbf{j}}$, respectively. Vertex $\mathbf{p}_v$ can then be represented in polar coordinates (R, θ), where θ is measured from **v**. Similarly, the point **c′** has orthogonal bases **u′**, **v′**, and **w′**. Using this system, the vertex point $\mathbf{p}_v$ was transformed to $\mathbf{p}_v'$, corresponding with centerline point **c′**, by applying its polar coordinates to the bases **u′**, **v′**, and **w′**. Repeating this process for every vertex of vessel t, vessel t was morphed such that only radial growth remained to generate vessel $t+T$. Local radial growth was determined by computing the intersection between the line $\mathbf{p}_v' + \alpha\mathbf{r}$ and the surface of vessel $t+T$, where α is a scalar **r** is the radial direction at point $\mathbf{p}_v'$.

4.3 Results

We completed a continuous 10 hour period of OCT imaging of a chick embryo, taking a volume scan of a vitelline artery every 60 minutes. After the imaging period, the embryo appeared normal with no signs of dysmorphic morphology or delayed development (Figure 26). Monitoring the embryo via a live video feed during the imaging period, we did not observe any abnormalities in cardiac rate. We returned the embryo to a forced-draft incubator and it continued to survive an additional 24 hours, at which point it was sacrificed.

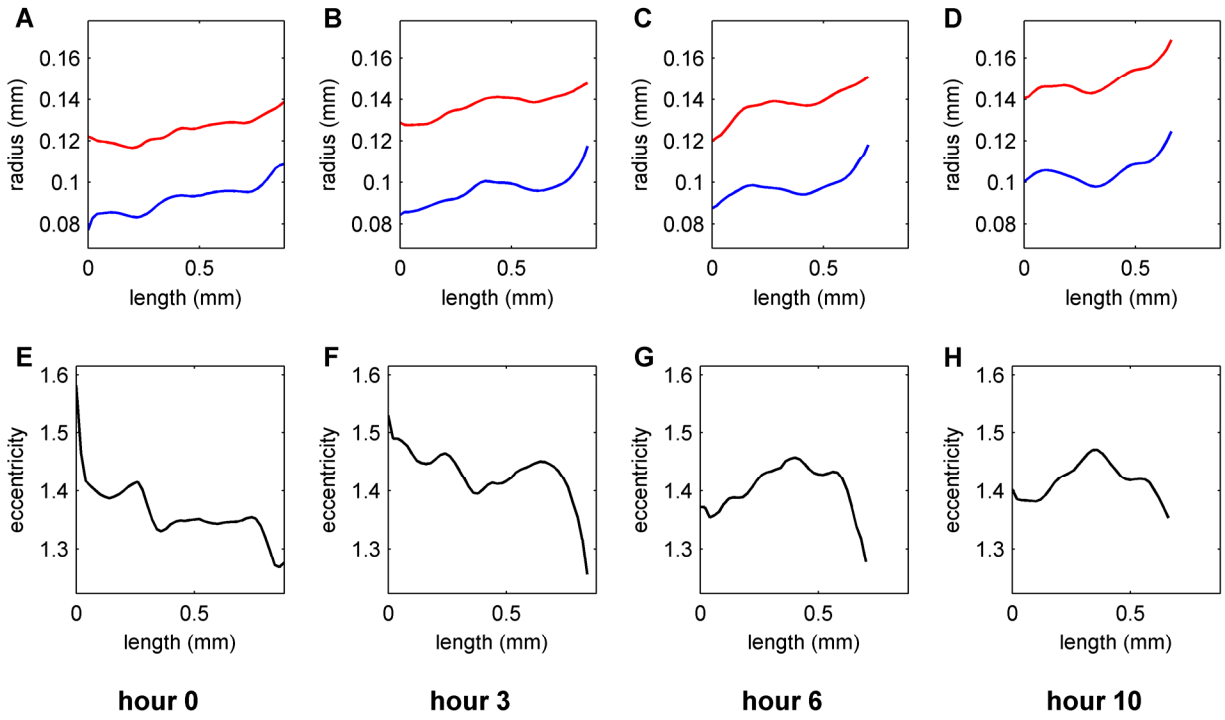

Figure 29. Morphometric analysis of the vitelline artery at four selected time points. (A-D) The major (red) and minor (blue) cross-section radii over vessel length at time 0, 3, 6, and 10 hours. (E-H) The cross-section eccentricity over vessel length. The x-axis is oriented proximal to distal.

We examined the morphology of the vitelline artery at each time point (Figure 29). The major and minor radii of the elliptical cross sections enlarged distally, which was unexpected as arterial vessels tend to reduce in diameter as the vessel becomes farther removed from the heart. This distal enlargement may be due to branching of the artery, which occurs near the distal boundary of our scanning region. We also observed eccentricity of the vascular cross-section (defined by the ratio of major to minor radius), which ranged from 1.25 to 1.6 (Figure 29). It appears that eccentricity reduced distally, but this trend does not hold for all time points. Comparison of mean radii over the imaging period revealed a linear increase in arterial caliber (Figure 30). The artery major and minor radii increased at a rate of approximately 1.8 and 1.2

μm/s, respectively. While the general trend increased, it was not continuous over the entire time period. In some cases, the artery radius reduced slightly. This feature may show a rapid morphogenetic response to altered flow or WSS, but the cause cannot be determined without additional data.

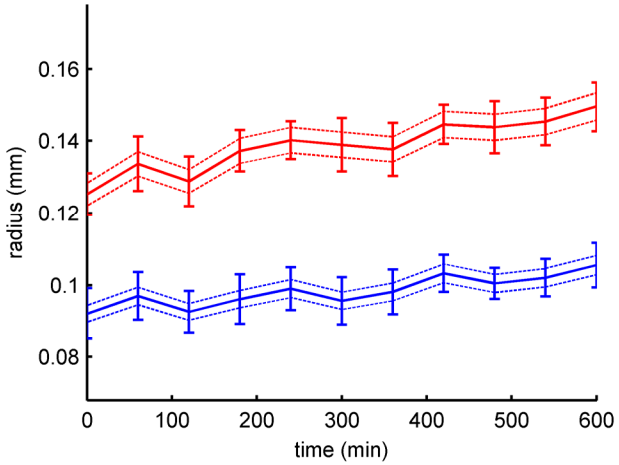

Figure 30. Global growth of the mean major (red) and minor (blue) radii of the vitelline artery over the 10 hour period. Bars indicate the SD over the vessel length. Dashed lines show the ±2.5% margins of error in our measurement. The major radius increased at a rate of 1.8 μm/s and the minor radius at a rate of 1.2 μm/s.

Quantitative analysis of local growth is presented in Figure 31. Cropping 3D data in the x-direction lead to mismatches in vessel length. Those sections that do not overlap with the subsequent time point are shown in gray. Radial growth varied spatially and both inward (negative) and outward (positive) growth was observed at all time points. At hour intervals 0-1, 2-3, 3-4, 6-7, and 9-10, outward radial growth dominated. These trends match the global radius growth (Figure 30) as the same intervals show periods of radial enlargement. Similarly, those time points where inward (negative) radial growth appears to dominate (Figure 31) are matched

with intervals of decreasing global radius (Figure 30). The data presented here are the first quantitative local radial growth measurements derived from time-lapse imaging of the chick embryo.

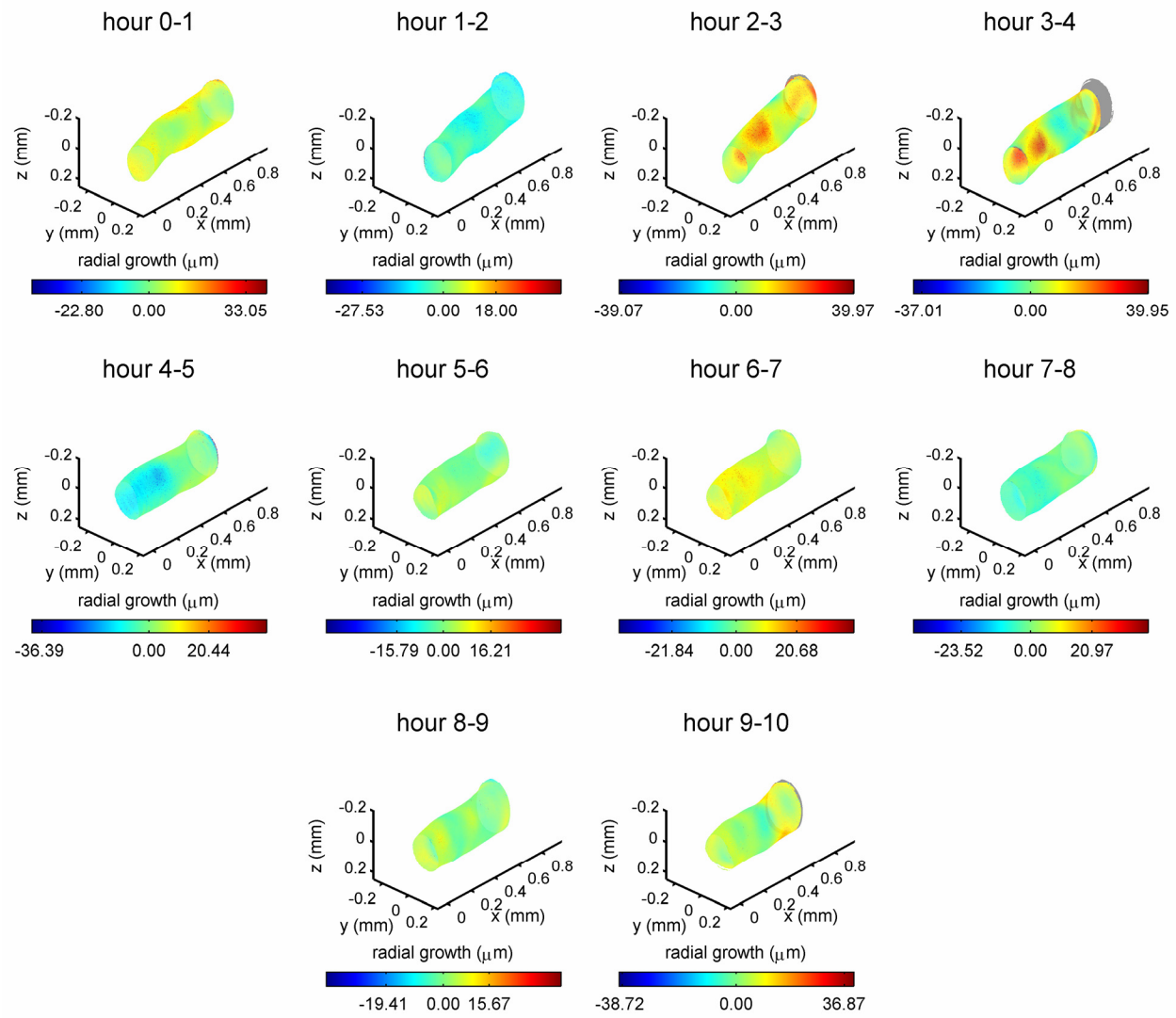

Figure 31. Quantitative local radial growth of the vitelline artery. For each time point, the radial growth that will occur by the next time point is shown as surface color. Color gradient scales are equivalent for all vessels; the minimum and maximum growth is marked on each scale. Outward radial growth is positive. Sections that do not overlap with the next time point due to cropping during segmentation are colored gray. The x-axis is oriented proximal to distal.

4.4 Discussion

Our study represents the first time-lapse quantification of local vascular growth and morphogenesis in the chick embryo. Other studies have measured cardiac volumes, cardiac function, and vascular diameters in multiple embryos at specific developmental stages (Henning et al., 2011; Holmes et al., 2009; Hu and Clark, 1989; Keller et al., 1991; Kowalski et al., 2013; Wang et al., 2009). These data provide valuable information on the overall hemodynamic and morphologic development of the embryo and their large sample sizes permit statistical comparisons. However, the process of averaging measurements among a large group of embryos masks individual variations in these trends. Furthermore, in the case of morphologic measurements, the practice of taking one measurement per structure (i.e. vessel), or spatially averaging 2-4 measurements to create a single value, does not capture local variations and thus presents a limited view of morphogenesis. Our technique can be used to derive global growth trends (i.e. change in vessel diameter, Figure 30) as well as local growth maps (Figure 31), providing a complete, quantitative analysis of vascular morphogenesis.

Time-lapse imaging and computation of local growth has a variety of applications towards understanding the mechanisms and principles of vascular morphogenesis. OCT has the capacity to obtain velocity measurements by analyzing the Doppler shift of successive A-lines (Davis et al., 2009). This Doppler data can be acquired simultaneously with the structural data in our system. An important caveat of Doppler-OCT data is that it measures the component of the velocity vector in the scan direction only (the *z*-component in the current study) (Davis et al., 2009). Therefore, the true velocity vector must be computed by combining with the angle between the scan direction and vessel axis. As this angle approaches 90° (as in the vessel used in this study), there is greater uncertainty in the velocity measurement. For this reason, our lab

demonstrated that the red blood cells, which are visible with OCT, can be used as tracers to perform particle image velocimetry (PIV) on OCT images (Chen et al., 2012). This technique presents an alternative method for acquiring velocity data. Obtaining time-lapse velocity data would allow us to track hemodynamic trends such as flow and heart rate increases. Hemodynamic WSS can be derived from velocity measurements, providing the spatially resolved local biomechanical loading. Combining the local growth data described in this study with complementary local WSS data would enable quantification of the relationship between WSS and vascular morphogenesis; a relationship that has thus far been estimated from sample-averaged flow and morphologic measurements, with hemodynamic and morphometric data often taken from different embryos (Kowalski et al., 2013). Acquiring both data in the same embryo at a local level would allow us to test various relationships between flow and growth and deduce quantitative principles that describe the well-established, but currently largely descriptive, role of hemodynamics in shaping vascular morphology.

The morphometric data obtained in our study can also be used in the development of predictive growth models. Previous models of both adult and embryonic vascular growth rely on phenomenological relationships and are validated by limited experimental data (Figueroa et al., 2009; Taber, 1998b; Taber and Eggers, 1996; Wagenseil, 2010; Watton et al., 2009). Our time-lapse imaging and growth analysis can be used to 1) design and train the growth laws used in these models to improve their predictive capacity and 2) test and validate the models. Interventions such as vitelline vein ligation, left atrial ligation, and outflow tract banding can be applied prior to or during imaging, which can test the predictive capabilities of these growth models in abnormal hemodynamic conditions. Acquisition of both growth and flow data as suggested above would further improve the training and testing of vascular growth models.

Our technique has applications to understanding the biology of vascular morphogenesis as well. The introduction of molecular constructs such as morpholinos by electroporation or transplantation has been used to study the role of various proteins in developmental events (De Bellard et al., 2007; El-Ghali et al., 2010; Kirby et al., 1997; Shiau et al., 2008). Combining these interventions with our technique would allow quantification of morphogenetic effects of these constructs. Obtaining quantifiable phenotypic differences after molecular intervention is vital to understanding the genetics and biology of cardiovascular development.

This study was primarily designed to demonstrate a new technique for long-term, time-lapse imaging of the chick embryo and quantification of vascular morphogenesis. Some limitations could be overcome to improve our method. The use of fiducial markers may improve the analysis of local morphogenesis by providing landmarks to accurately align vessels when computing growth vectors (Filas et al., 2007). We applied a morphing algorithm that minimizes the total displacement of one vessel relative to another, but this assumption may be incorrect. More advanced 3D segmentation techniques may be necessary to reconstruct complex morphologies such as vitelline networks and the aortic arches. Doppler-OCT or PIV analysis could be added to provide simultaneous velocity measurements as discussed previously. Finally, as OCT technology continues to advance, increased imaging depth would enable more complete views of large structures such as the embryonic heart.

We have demonstrated the first long-term, time-lapse *in ovo* imaging system for quantifying local vascular growth and morphogenesis in the chick embryo. Our imaging chamber required inexpensive components and successfully maintained normal embryonic development. Automated time-lapse acquisition of a vitelline artery was completed using our custom-built software interface and our segmentation and reconstruction methods provided 3D

models of the vessel at each imaging cycle. Our computational growth analysis quantified a linear change in the vessel radius and spatially resolved local growth, which revealed non-uniform changes in vessel shape. Our technique can be combined with velocimetry to discern quantitative relationships between hemodynamics and vascular morphogenesis, predictive growth models, and molecular interventions to uncover quantifiable phenotypic consequences. The utility of this technique will augment future studies of cardiovascular morphogenesis and further our understanding of this complex developmental process.

Chapter 5

Left atrial ligation alters intracardiac flow patterns and the biomechanical landscape in the chick embryo

5.1 Introduction

Hypoplastic left heart syndrome (HLHS), is a rare but serious congenital heart defect, occurring in 1 of every 5000 births (Go et al., 2013). The hallmarks of HLHS are an underdeveloped and nonfunctioning left ventricle and hypoplastic ascending and transverse aorta in association with stenosis or atresia of the mitral and/or aortic valves, and intra-uterine compensatory enlargement of right sided cardiac structures (Friedman et al., 1951; Noonan and Nadas, 1958). A genetic component for HLHS is supported by studies that examined heritability, which show that HLHS is linked to chromosomes 10q and 6q and genetically related to bicuspid aortic valve (Hinton et al., 2007; Hinton et al., 2009), although the strength of this relationship is unknown (McBride et al., 2009). The genetic basis of HLHS is still largely undetermined and no transgenic animal models have recapitulated the human HLHS phenotype (Sedmera et al., 2005). Clinical innovations and scientific research has significantly improved the outlook for infants born with HLHS from a fatality rate of over 95% in 1980 to our current projections that 70% of infants born with HLHS are expected to survive to adulthood (Feinstein et al., 2012). These advances in diagnostic and treatment strategies are remarkable, however the pathogenesis of HLHS during embryonic and fetal life remains poorly understood. Fetal interventions have become available with the goal of positively impacting fetal and post-natal cardiac growth and remodeling.

For most of its history, HLHS has been classified as a "flow defect," attributed to altered hemodynamic loading of the left heart structures, and fetal echocardiography has demonstrated

that blood flow patterns have an important role in the development of HLHS (Grossfeld et al., 2009). An abnormally small or absent foramen ovale may be one key component, reducing flow to the left heart and impairing normal growth of left heart structures (Chin et al., 1990; Feit et al., 1991; Rychik et al., 1999), and one study has shown a correlation between diameter of the foramen ovale and relative right heart and/or left heart flow (Atkins et al., 1982). Obstructed inflow or outflow of the left ventricle due to valvular defects is more likely, however, as there is a strong correlation between the diameter of the left atrioventricular (AV) junction and left ventricle or aortic root (Sedmera et al., 2005). While the initial insult causing HLHS, genetic or structural, is unknown, the resulting hemodynamic alterations are significant and progressive. A typical diagnostic scenario in the clinic is detection of normal left heart dimensions with reduced function at mid-gestation, which is later followed by progressive involution of the left ventricle in the third trimester of pregnancy (McElhinney et al., 2010). One unifying hypothesis is that altered intracardiac flow patterns (ICFP) and altered mechanical loading conditions result in left ventricular hypoplasia due to the lack of sufficient mechanical loading to stimulate cardiac growth and remodeling. This hypothesis has been applied as a rationale for fetal interventions, in which fetal balloon aortic valvuloplasty is performed to restore normal antegrade aortic flow and left ventricular loading conditions (McElhinney et al., 2010).

A large number of transgenic animal models have revealed key roles for signaling pathways and transcription factors in many of the events required for normal cardiovascular development, including outflow tract (OT) septation (Franz, 1989; Tallquist and Soriano, 2003), valve morphogenesis and remodeling (de la Pompa et al., 1998; Dunker and Krieglstein, 2002; Hurlstone et al., 2003; Ranger et al., 1998), and myocardial contraction (Bartman et al., 2004). However, embryonic models that alter the mechanical environment in the setting of a normal

genotype are limited. These studies are usually performed in avian embryos, mainly represented by vitelline vein ligation (Hogers et al., 1997; Rychter and Lemez, 1965), conotruncal banding (Clark et al., 1989), and left atrial ligation (Rychter and Lemez, 1965; Sedmera et al., 1999). Acquiring reliable, spatially-resolved velocity measurements in the embryonic heart remains challenging, and many studies lack a quantitative analysis of the biomechanical environment after these perturbations. Newborn and juvenile models of univentricular circulation have been developed in sheep to monitor cardiac function after repair of HLHS, though their long-term success and application is limited (Myers et al., 2006; Rodefeld et al., 2003). Further research using these existing mechanical models, and the development of novel models, is necessary to understand the role of hemodynamics and optimize fetal intervention strategies (Pekkan and Keller, 2013).

Left atrial ligation (LAL) in the chick embryo remains the only long term prenatal animal model of HLHS (Rychter, 1962). In the LAL model, tying off the presumptive left atrium as a recoverable procedure disrupts inflow to the left side of the embryonic ventricle. Measured as early as one hour after ligation, cardiac output is transiently reduced, returning to normal levels by 32 hours post-LAL, while downstream cardiac pressures remain normal throughout (Lucitti et al., 2005). Signs of remodeling of the ventricular myocardium can be observed two days after ligation, including decreased myocardial volume, accelerated trabecular compaction, and delayed changes in transmural myofiber angle (Sedmera et al., 1999; Tobita et al., 2005). Circumferential and longitudinal strain increases in both ventricles after LAL, while the onset of preferential circumferential strain patterns in the right ventricle are accelerated and the preferential longitudinal strain patterns in the left ventricle are abolished (Tobita and Keller, 2000). Cellular changes after LAL include reduced proliferation in the left ventricular compact

layer and trabeculae, decreased expression of FGF-2 and PDGF-B throughout the heart, and an increased number of apopototic cells in the right AV cushions (Sedmera et al., 2002) as well as increased microtubule density in the left ventricular compact layer (Schroder et al., 2002). In spite of the limited number of studies focusing on vascular development compared to the ventricle, downstream vessels are also affected in LAL; flow distribution within the aortic arches (AA) is disrupted, and defects including aortic arch hypoplasia and interrupted aortic arch are observed as early as 32 hours after ligation (Hu et al., 2009).

These previous studies clearly demonstrate the morphologic, structural remodeling, and cellular consequences of LAL. However, to date there has not been a *quantitative* analysis of changes in ICFP that occur following LAL. While hemodynamic anomalies such as reduced left ventricular filling and mitral, tricuspid, and aortic valve regurgitation have been recorded, these were observed four days post-LAL (deAlmeida et al., 2007). The immediate effects of LAL (< 1 hour after ligation) on flow patterns are therefore unknown. Furthermore, quantitative analysis of hemodynamic loading after LAL has not been performed. In this study, we test the hypothesis that ICFP are altered immediately following LAL. Validation of this hypothesis would demonstrate that changes in ICFP precede changes in ventricular morphology and structure, supporting the idea that flow patterns are a primary factor in the production of the HLHS phenotype after LAL. We applied a quantitative analysis of fluorescent dye microinjections to map the location of the intracardiac flow stream within the ventricle and OT. We further developed a computational fluid dynamics (CFD) model of the normal and LAL heart loop to estimate changes in wall shear stress (WSS) that may occur due to the occlusion of the left atrium. Our results show that the position of the intracardiac flow stream is shifted significantly in 2 out of 3 injected venous sites and that WSS is reduced at the left AV canal and left ventricle.

Thus, LAL immediately re-routes flow through the heart, likely causing reduced biomechanical loading and growth of left heart structures and leading to impaired remodeling and eventual HLHS.

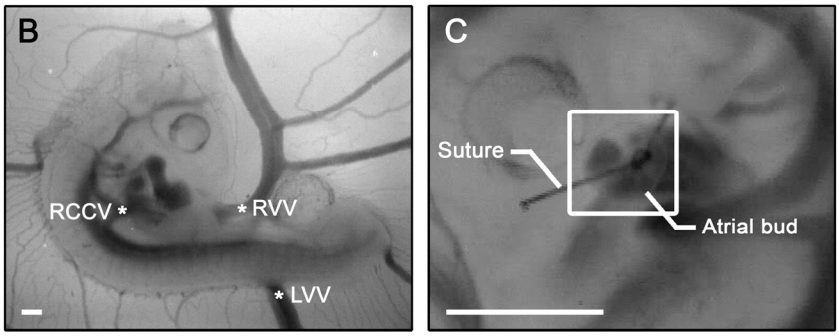

Figure 32. The HH21 chick embryo experimental model. B) Stereomicroscope image of a normal HH21 embryo, viewed from the right lateral perspective. Venous injection sites used in this study are labeled. The right common cardinal vein (RCCV) is the confluence of the right anterior and posterior cardinal veins, which drain blood from the embryo proper. The left and right vitelline veins (LVV, RVV) return blood from the extraembryonic vitelline bed. C) Stereomicroscope image of an LAL embryo, viewed from the left lateral perspective. The primitive left atrium is tied off with a 10-0 nylon suture. All scale bars are 500 μm.

5.2 Results

5.2.1 Intracardiac flow streams in normal and LAL embryos

We performed LAL at HH21 (Al Naieb et al., 2012; Hamburger and Hamilton, 1951). At HH21, cardiac looping is largely complete, with only minor migration and rotation of the OT progressing through HH24 (Manner, 2000). The left and right atrial cavities have formed and ventricular trabeculation is present, though neither septum has fully formed (Martinsen, 2005). The dorsal and ventral AV canal cushions have started to form (De la Cruz et al., 1983), and four

of the five primary OT cushions are present (Qayyum et al., 2001). Blood enters the common atrium through several venous sites including the vitelline veins (VV), which drain the vitelline bed, the right and left common cardinal veins (CCV), which return blood from the embryo proper, and the allantoic veins, which drain the allantois (Figure 32). The HH21 embryonic heart rate is 155 beats per minute and cardiac output is 1.28 mm^3/s (Hu and Clark, 1989).

To visualize flow streams, we injected embryos with fluorescent dye at three different venous sites: 1) the right CCV (RCCV), 2) the right VV (RVV), and 3) the left VV (LVV) (Figure 32). Each embryo was injected once; sham and LAL embryos were injected after a reincubation period lasting less than 1 hour. We computed a normalized intracardiac stream position from the recorded injections. Blood flow was laminar in all embryos. The heart continued to beat at a constant rate for a minimum of one minute after dye injection, allowing us to record multiple cardiac cycles. Low Reynolds number flow in the embryonic ventricle does not allow flow stream mixing. After removing the needle, blood hemorrhaged and the heart beat ceased rapidly afterward. Our fluorescent dye injections and image analysis allowed us to quantitatively compute the position of the intracardiac flow stream within the common ventricle and OT. Results of our experimental dye injections are summarized in Figure 33 and Figure 34. Our normalized stream position represents the distance from the dorsal wall of the embryonic heart, where 0 is exactly the dorsal wall and 1 is exactly the ventral wall. For control embryos, we found that dye injected at the RCCV took a slightly dorsal route, with an average stream location of 0.44±0.09 (n=12). The stream from the RVV was the most dorsal, with a position of 0.41±0.11 (n=17). The location of the LVV stream was 0.49±0.07 (n=13), directly through the midline of the heart. Sham embryos displayed similar ICFP, with no significant differences vs. the control group.

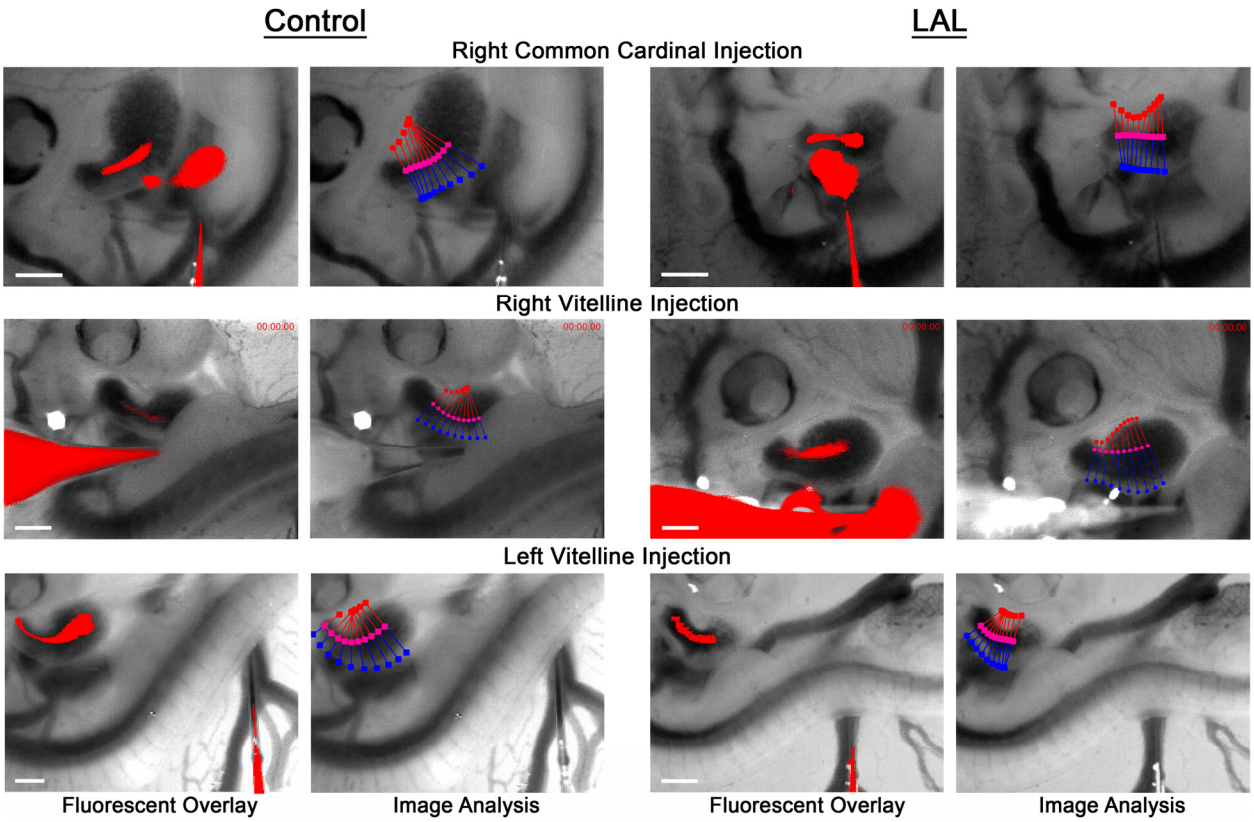

Figure 33. Representative images from the experimental fluorescent dye injections. Control embryos are on the left and LAL embryos are on the right. For each injection site, the overlay of the fluorescent and bright field image is shown alongside the output of the image analysis to measure the distance between the flow stream (pink) and the ventral (red lines) and dorsal (blue lines) walls of the heart. All scale bars are 250 μm.

The response of LAL embryos to insertion of the micro needle was similar to control embryos with no observable effect on hemodynamics or heart rate. For LAL embryos, our quantitative analysis revealed that the RCCV stream changed significantly ($p<0.05$), now taking a ventral course through the ventricle and OT, with an average location of 0.66±0.16 (n=11). The RVV stream also shifted toward the ventral side of the heart ($p<0.05$), positioned at 0.54±0.10 (n=7). The intracardiac path of the LVV remained similar at 0.52±0.08 (n=8, $p>0.05$).

In the LAL embryos, the RCCV and RVV streams were ventral to the LVV stream, the reverse of the control ICFP. Interestingly, all flow patterns shifted ventrally, although only the RCCV and RVV were significantly changed compared to the controls. We also observed some retrograde flow in the LAL embryos, where dye injected at the RVV and LVV would flow into the cardinal veins. These results demonstrate that LAL significantly alters ICFP in the embryo, and that this change occurs immediately following the intervention.

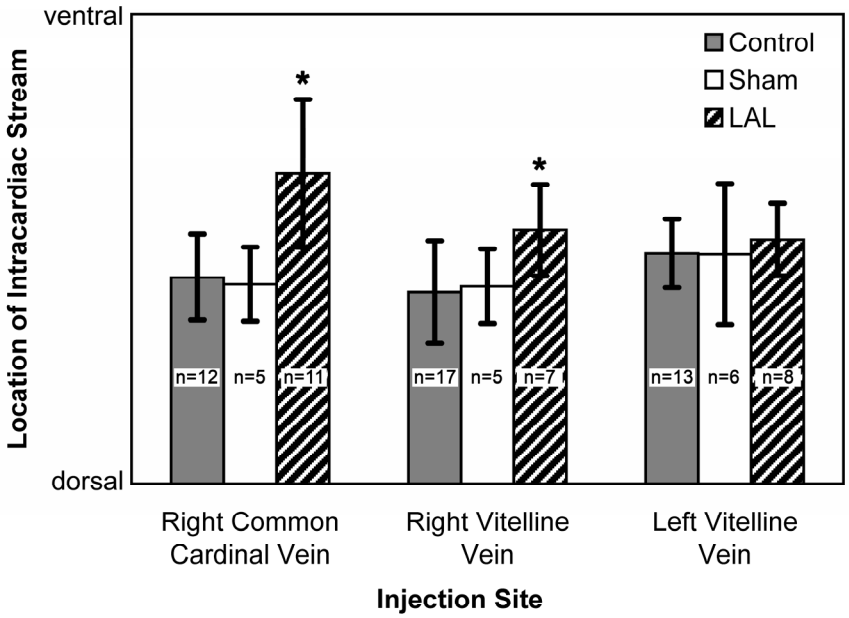

Figure 34. Results of the intracardiac stream measurements. The average location of the stream in control, sham, and LAL embryos is shown. Error bars represent the standard deviation. Numbers within each bar indicate the sample size. * Indicates a statistically significant ($p<0.05$) difference vs. the control group.

5.2.2 *In silico* LAL model

We performed 3D CFD simulations of steady flow through control and LAL models of the HH21 heart loop. Both models were created in the computer using our in-house surgical

planning suite (Dur et al., 2011; Pekkan et al., 2008d). Blood flow was modeled using our in-house immersed boundary cardiovascular flow solver, which has previously been validated for models of the HH11, 13, and 18 heart loop, comparing accurately with the commercial second-order unstructured grid flow solver Fluent (version 6.3.26, ANSYS Inc., Canonsburg, PA) and experimental microfluidic models of the embryonic heart tube (Pekkan et al., 2009). Mean total cardiac output was 1.28 mm^3/s, equivalent to HH21 Doppler flow measurements (Yoshigi et al., 2000), and rigid, no-slip walls were assumed for simplicity, simulating mean quasi-steady flow conditions in the heart. We computed color-coded flow streamlines originating from the right and left vitelline veins in order to observe ICFP in our CFD models (Figure 35). There were some subtle differences, including an overall ventral shift of the flow streams in the LAL model (Figure 35). This movement of ICFP toward the ventral margin of the heart is similar to our experimental observation. Flow from the RVV seemed to follow the inner curvature of the heart more tightly in the LAL model as well. However, the variation between the control and LAL CFD models is far less pronounced than the experimental results, and we did not observe the reversal of RVV and LVV stream positions (Figure 35), prompting future improvements in computational model. We computed the velocity profile at the OT and found that it was slightly more skewed in the ventral and left directions in the LAL vs. control model. To examine changes in biomechanical loading that occur due to removal of the left atrium, we calculated WSS from our CFD results (Figure 36). The maximum WSS levels in the heart were 3.5 Pa, found at the CCV and VV inlets and the ventral side of the OT outlet, consistent with WSS values derived from particle image velocimetry in similar stage chick embryos (Poelma et al., 2010). Compared to the control model, WSS in the LAL model was reduced at the left side of the AV canal and left side of the common ventricle (Figure 36). WSS was also slightly increased

at the ventral surface of the distal OT. These simplified, static CFD models show that redistribution of the left atrial volume is sufficient to alter ICFP and WSS loading, while the disparity with the experimental results supports the additional roles of the endocardial cushions and dynamic ventricular suction during relaxation in determining ICFP.

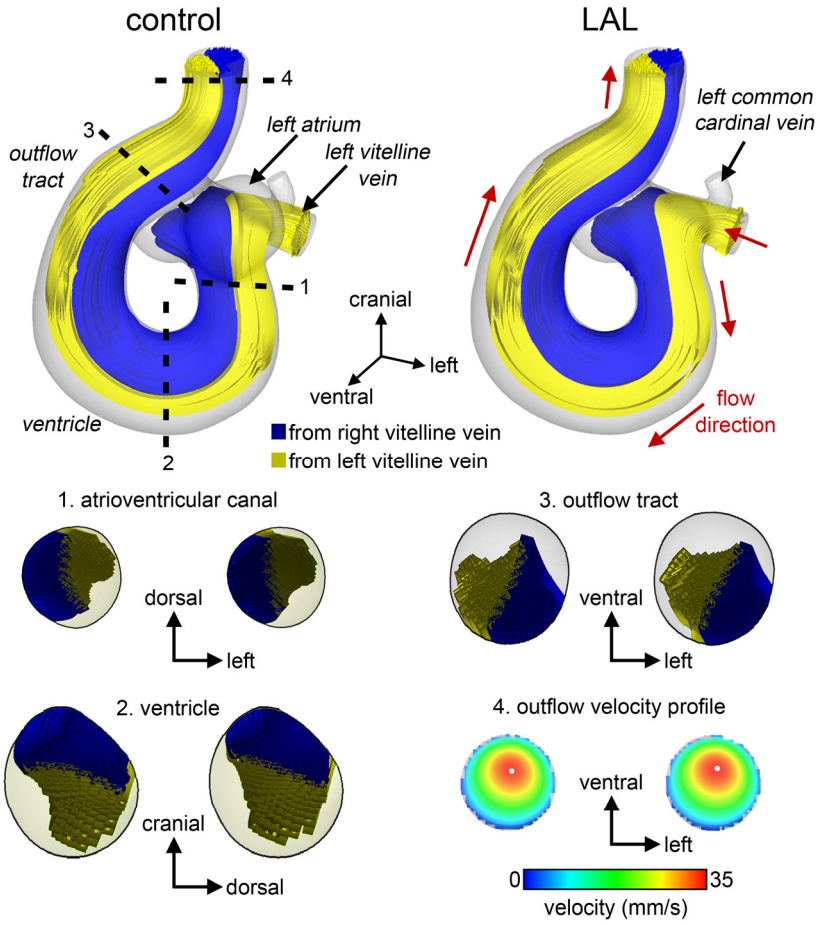

Figure 35. Intracardiac flow patterns in CFD models of control and *in silico* LAL embryonic cardiac geometries. The control model is on the left and the LAL model is on the right. In the upper figures, color coded streamlines are shown, with blue representing flow emanating from the RVV and yellow depicting flow from the LVV. Red arrows give the forward flow direction. The bottom panels show cross-sections at each of the sites labeled in the control flow stream figure. Control cross-sections are on the left and LAL on the right. The cross-sections reveal a

slight overall ventral shift of flow paths in the LAL model. The velocity profile at the OT is shown for cross-section 4, where a ventral shift of the peak flow location is observed in the LAL model.

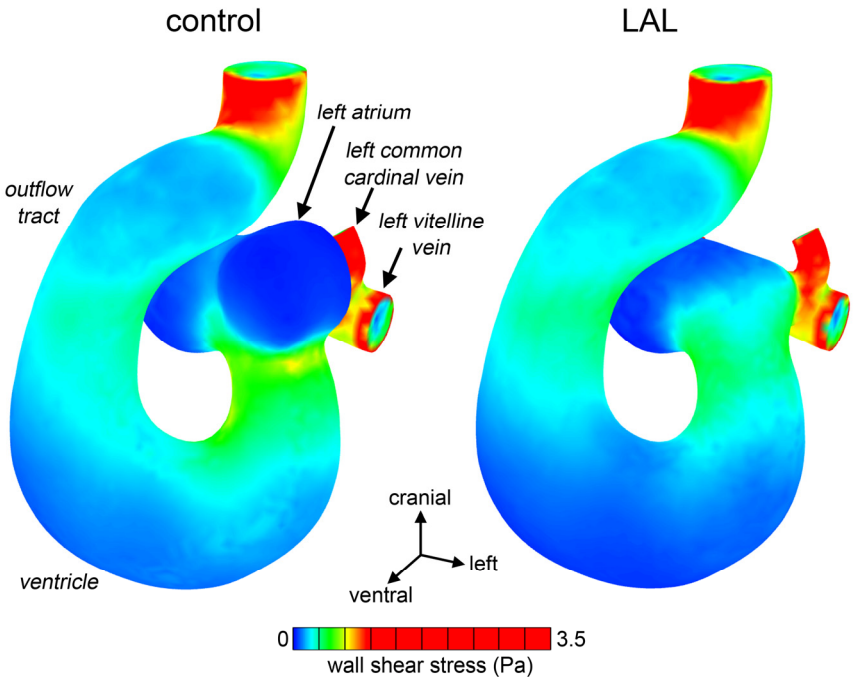

Figure 36. WSS computed from CFD models of control and *in silico* LAL embryonic cardiac geometries. The control model is on the left and the LAL model is on the right. Reduced WSS can be seen at the left side of the AV canal and left region of the common ventricle. Increased WSS is located at the ventral side of the distal OT. To display a broader range of WSS, a peak WSS of 1.0 Pa is shown.

5.3 Discussion

Qualitative description of normal ICFP in the chick embryo has been taken up by several authors, giving rise to some contradictions (Bremer, 1932; Hogers et al., 1995; Jaffee, 1967;

Rychter and Lemez, 1965; Yoshida et al., 1983). Early studies attempted to follow red blood cells as they coursed through the heart, and led to the widely perceived notion that two separate streams spiraled around each other through the OT (Bremer, 1932; Jaffee, 1967). The presence of these streams was thought to shape the spiral aortopulmonary septum, with anomalous spiraling proposed as a major cause of septation defects (Jaffee, 1965). This notion was challenged when researchers began injecting dyes or India ink and did not observe spiraling outflow streams (Hogers et al., 1995; Yoshida et al., 1983). In their comprehensive study of chick embryos between HH14-22, Yoshida et al. observed two types of intracardiac streams which depended on both injection site and developmental age (Yoshida et al., 1983). These streams did not spiral around one another, but rather followed a dorsal or ventral path through the ventricle and OT. These patterns were later confirmed by Hogers et al. using India ink injections of embryos between HH12-17 (Hogers et al., 1995). Their study revealed distinct ICFP for blood emanating from different yolk sac regions, further demonstrating the significance of venous return sites and the presence of multiple simultaneous ICFP. Our ICFP observed in control HH21 embryos matched those of Yoshida et al. (Yoshida et al., 1983), with blood from the RVV taking a more dorsal path compared to blood from the LVV. No study has examined either CCV. In no cases did we observe evidence of spiraling streams through the OT. The work of Yoshida et al. also suggested that blood from the RVV and LVV perfused only the ipsilateral AA at HH21 (Yoshida et al., 1983). This pattern was contradicted by other studies, which showed that the distribution through the AA was not a simple left and right current (Hogers et al., 1995; Hu et al., 2009; Rychter and Lemez, 1965). While we did not examine ICFP beyond the OT in this study, our previous investigations dedicated to the AA corresponds with a complex perfusion pattern (Kowalski et al., 2013; Wang et al., 2009).

Yoshida et al. observed nearly the exact reverse ICFP in embryos HH17-18: blood from the RVV took a more ventral route compared to blood from the LVV, and the two streams perfused the contralateral AA (Yoshida et al., 1983). These patterns transitioned at around HH19, and the authors attributed the dramatic reversal to the changes in the vitelline venous system. Our data show that in LAL HH21 embryos, blood from the RVV courses more ventrally compared to blood from the LVV, similar to the HH17-18 patterns described by Yoshida et al. (Figure 33). It may be that obstruction of the left atrium prevents the change in RVV and LVV patterns or returns ICFP to their earlier state. Prior to HH18, the atrial cavities are small and hardly distinguishable from the heart tube. Between HH18 and 21, however, the atria significantly increase in size, particularly the left atrium, which becomes larger than the right (Kim et al., 2011; Manner, 2000; van den Berg and Moorman, 2011; Yalcin et al., 2011). This expansion of atrial volume and the atrial contribution to ventricular filling may relate to the change in ICFP, which occurs during the same interval. As the expansion of the left atrium is more pronounced than the right, its ligation may return the cardiac geometry to resemble HH17, causing ICFP to revert. Ventricular trabeculation may also have a role in the changing flow patterns at HH19. Beginning at HH16/17, trabeculation progresses rapidly during this period, and is largely responsible for increases in myocardial mass (Sedmera et al., 2000). Another key morphologic event occurring during the period between HH17 and 25 involves substantial growth and remodeling of the endocardial cushions lining the AV canal and OT, brought on by the invasion of cells that begin to undergo epithelial to mesenchymal transformations at HH17 (Butcher et al., 2007; Noden, 1991). LAL may interfere with these events by preventing growth of the left atrium, limiting the expansion of the AV canal, or displacing the endocardial cushions.

Our numerical control vs. LAL CFD models confirmed the variation in the location of the flow streams originating from the RVV and LVV, but these are less pronounced that the *in vivo* injections (Figure 35). A major difference is that we do not see the dramatic ventral shift of the RVV flow stream after LAL. Presently, our CFD model did not incorporate the endocardial cushions or ventricular trabeculae and applied rigid, no-slip walls and steady, unidirectional flow, ignoring the AV synchronous contractions and pulsatile flow environment. Furthermore, the external boundary conditions specified at the vessel inlet and outlets, as well as the neglected wall movement, may suppress the *in vivo* observed internal flow differences. These limitations influence the numerical model of ICFP and mask key elements of the biomechanical environment such as oscillatory WSS. Effects of flow pulsatility is less important, illustrated in our previous pulsatile CFD models of the HH18 heart loop, which revealed that Womersely numbers were low (0.44), suggesting that the effects of pulsatile flow are small (Pekkan et al., 2009). The assumptions described above were necessary to reduce computational time and produce a solvable model. Differences between the comparative model and experiment may indicate that those aspects absent from the model, such as cardiac contractions, endocardial cushions, and ventricular trabeculae, are vital to establishing ICFP. Even without these features, however, our models show that simply removing the left atrium can alter the course of blood and WSS levels in the heart realistically. In particular, WSS was reduced at the left side of the common ventricle and left wall of the AV canal and slightly increased on the ventral surface of the OT (Figure 36). WSS differed by 0.5 Pa at these sites, which is above the known threshold to initiate an endothelial response (Egorova et al., 2011b). These areas are commonly affected in HLHS, suggesting that LAL may redirect flow to unload the presumptive left ventricle and its inflow. The velocity profile change in the *in silico* LAL model may indicate a reason for altered

AA perfusion and defects in LAL embryos (Hu et al., 2009). However, our recent simulations of AA flow using various velocity profile shapes at the OT do not show significant changes in flow distribution or WSS, again demonstrating the importance of the dynamic contractions (Kowalski et al., 2013).

Morphogenesis of the veno-atrial region is ongoing at HH21, and the veno-atrial connections may differ between embryos (Manner and Merkel, 2007; van den Berg and Moorman, 2011). Our model geometry includes proximal separation of the right and left vitelline veins, a centrally located venous sinus, and symmetric cardinal veins, all of which are characteristic of the early state of veno-atrial morphogenesis (Figure 35). By HH24, however, the proximal vitelline veins have fused, the sinus connection is limited to the right atrium, and the left cardinal vein is elongated. As this transformation likely influences ICFP, we modified our model geometry to correspond with this later state venous anatomy and repeated our control and LAL flow models (Figure 37). As with our original geometry, flow patterns in the LAL model were not substantially different from the control. This later state model, therefore, reinforces our previous reasoning that those features not incorporated, i.e. cardiac contractions, endocardial cushions, and ventricular trabeculae, have a role in directing intracardiac blood flow. We did find, however, that the outflow velocity profile was more skewed in the ventral direction after changing the venous morphology (Figure 35 and Figure 37). These two models suggest that morphogenesis of the sinuatrial region can influence ICFP and may provide an explanation for the changes in flow patterns that occur in normal embryos from HH18 to 24 (Yoshida et al., 1983).

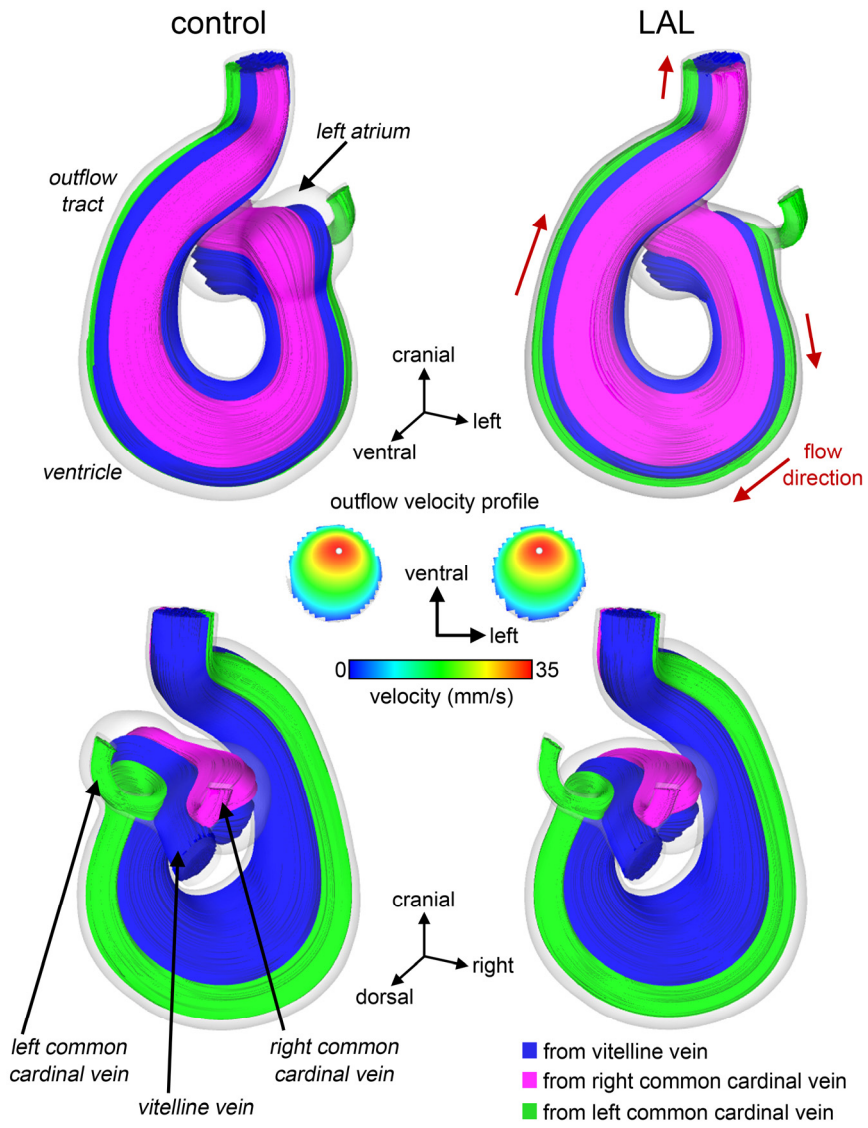

Figure 37. Intracardiac flow patterns in CFD models of control and *in silico* LAL embryonic cardiac geometries. The control model is on the left and the LAL model is on the right. The cardiac geometries were modified from those shown in Figure 35 to examine later venous remodeling, including the rightward shift of the venous inlet and proximal fusion of the vitelline veins. The model is viewed from the ventral (upper panels) and dorsal (lower panels) perspectives. Color coded streamlines are shown, with blue representing flow emanating from the VV, pink depicting flow from the RCCV, and green depicting flow from the LCCV. Red arrows give the forward flow direction. At the center, the outflow velocity profiles are shown.

Static CFD models of flow in the human embryonic heart show the presence of multiple simultaneous intracardiac streams, with patterns similar to those observed in the chick embryo, demonstrating the relevance of these animal models to human development (DeGroff et al., 2003). While success has been made in reconstructing static embryonic cardiac geometries from polymeric casting (Wang et al., 2009; Yalcin et al., 2011), there is no existing model of the dynamic embryonic heart. Recent techniques have simulated blood flow in the contractile OT (Liu et al., 2011), though this work is in nascent stages and has yet to incorporate the upstream heart and downstream vessels. Validation of such models will require information of 3D velocity profile shapes *in vivo*. We have recently explored a combined particle image velocimetry and optical coherence tomography technique to acquire velocity measurements non-invasively, which can be applied to future studies (Chen et al., 2012).

The mechanosensitivity of endocardial cells, coupled with the changed ICFP after LAL, likely results in abnormal morphogenesis and remodeling of the AV and OT cushions, leading to valve defects normally present in HLHS. Although our technique does not capture total flow through the AV canal, the quantitative measurements through the OT show a significant ventral shift of the RVV and RCCV streams (Figure 34). In the RVV ligation model of Hogers et al., flow streams from two of the four yolk sac regions saw a similar dorsal to ventral shift (Hogers et al., 1997). It is interesting that the outlet of the left ventricle is dorsal to that of the right ventricle in the mature chick. The lack of a dominant dorsal stream after LAL may cause reduced WSS on the dorsal cushions present at HH21, impairing the formation of the left ventricle OT and aortic valve.

Our experiments support the hypothesis that LAL immediately alters ICFP in the chick embryo. We quantitatively showed a significant ventral shift in both the RVV and RCCV flow

streams. While the LVV flow stream did not change significantly, the LVV and RVV streams switched relative positions in LAL compared to control hearts, resembling earlier HH18 patterns (Yoshida et al., 1983). Our static CFD model of the embryonic heart loop further revealed that removing the left atrium volume was sufficient to alter WSS at critical locations within the left heart. These results suggest that changes in ICFP following LAL precede structural defects such as bicuspid aortic valve and the characteristic undersized left ventricle. The concordance between control and sham embryos suggests that the manipulations required to perform LAL do not cause a change in flow patterns. However, the ligation itself may cause structural damage to the heart, which can affect its further development. While we take great care and reject any embryos that show bleeding after LAL, we cannot rule out this trauma as a cause for HLHS defects. Therefore, we conclude that the change in ICFP occurs early in development of HLHS after LAL, but may not be the only or initial insult.

5.4 Experimental Procedures

5.4.1 Experimental measurement of intracardiac stream position

5.4.1.1 Embryo preparation and injection

Fertile white Leghorn chicken eggs were incubated blunt end up in a forced draft incubator at 37°C and 50% humidity for 84 hours to Hamburger-Hamilton HH21 (Al Naieb et al., 2012; Hamburger and Hamilton, 1951). To access the developing embryo, we gently cracked the eggshell above the air sac and peeled back the shell and membrane to form a 1 cm^2 window. We then removed the overlying extraembryonic membrane using microforceps (Dumont M5, WPI, Sarasota, FL). Limb size, spinal curvature, and the presence of body tissues were used to stage embryos, and any that were dysmorphic, such as lacking retina, displaying axial twisting, or left

side up were excluded. To perform LAL, we positioned embryos *in ovo* under a stereomicroscope (Leica M165FC, Leica Microsystems GmbH, Germany), dissected the amniotic membrane and flipped the embryo to reveal the presumptive left atrium. We used microforceps to make a slit-like opening in the thoracic wall above the atrium and tightened an overhand knot formed from 10-0 nylon suture around the primitive left atrium, decreasing its effective volume (Figure 32) (Tobita et al., 2005). We repositioned the embryo to its original right-side up orientation, sealed the window with Parafilm M (Pechiney Plastic Packaging, Menasha, WI), and reincubated for one hour to restore normal heart rhythms. Control embryos had only the overlying membrane removed and were injected immediately with no reincubation. Sham embryos had a slit made in the thoracic wall above the left atrium and were reincubated for one hour.

To inject embryos, we pulled needles from 1.0 mm inner diameter glass capillary pipettes to 15 μm inner diameter and a 30° bevel (PC-10 Puller, EG-44 Microgrinder, Narishige Inc., Japan). Needles were connected via polyethylene tubing (PE100, Braintree Scientific, Braintree, MA) to a 10 μl glass Hamilton gastight syringe (1701LT, Fisher Scientific, Waltham, MA). The syringe was mounted on a three-axis mechanical micromanipulator (Leica Microsystems GmbH, Germany). We primed the syringe, tubing, and needle with chick Ringer's solution and then drew up 1 μl of Cy5-diethyl fluorescent dye diluted 1:1 in PBS (excitation wavelength 626 nm, emission wavelength 666 nm). Cy5 dyes were prepared at the Molecular Biosensor Imaging Center at CMU (Mujumdar et al., 1993). We injected embryos at three different venous sites: 1) RCCV, 2) RVV, and 3) LVV, with all embryos viewed in the right side up orientation (Figure 32). Each embryo was placed under the stereomicroscope and the yolk sac membrane (RVV, LVV sites) or amnion (RCCV site) was removed above the injection site. The needle was

inserted into the selected vein and a bright field movie was recorded using a low light monochrome digital camera (Leica DFC 350FX, Leica Microsystems, GmbH, Germany). We then injected 0.3 µl of dye, visualized using an external fluorescent light source (Leica EL6000, Leica Microsystems, GmbH, Germany) and recorded the flow streams. This volume of injected dye has been shown to minimally affect normal hemodynamics, resulting in less than a 10% change in stroke volume and mean arterial pressure (Wagman et al., 1990). A total of 84 embryos were injected: 28 RCCV (12 control, 5 sham, 11 LAL), 29 RVV (17 control, 5 sham, 7 LAL), and 27 LVV (13 control, 6 sham, 8 LAL). All injections were performed *in ovo* and only one site was injected per embryo.

5.4.1.2 Quantitative measurement of the intracardiac flow stream

We applied a quantitative approach to determine the location of the intracardiac streams. End-diastolic still images (696x520 pixels) were extracted from the recorded bright field movies and used to manually identify the ventral and dorsal boundaries of the ventricle and OT. The manually selected points were used to form polynomial expressions defining the shape of the ventral and dorsal margins, giving two continuous functions. We used the horizontal position as the independent variable, and rotated images, if necessary, so that the long axis of the heart was approximately horizontal. We then extracted still frames from the fluorescent recordings of the injections, which showed the flow stream as it passed through the ventricle and OT. The centerline of the flow stream was manually identified and used to form a third polynomial expression. Any rotations applied to the bright field image were applied exactly to the fluorescent image. For each point along the flow stream, we were then able to mathematically calculate the two points of intersection between the line normal to the stream and the ventral and dorsal walls of the heart. Using these intersection points, we then calculated the Euclidean

distance between the centerline of the stream and the ventral (ε) and dorsal (δ) walls. The normalized intracardiac stream position was defined as δ/(ε+δ). We computed the position for 10 evenly distributed points along the stream centerline and took the mean value as the final intracardiac stream position (Figure 33). The entire process was performed using a semi-automated *ad hoc* program developed in MATLAB (R2011a, Mathworks, Natick, MA). We performed the analysis once per embryo.

The bright field movie was recorded after insertion of the needle into the vessel, but before injection of the dye. The injection movie was then recorded without moving the embryo or changing the zoom level, in order to facilitate direct overlapping. As a check, we can clearly observe that the dye within the needle seen in the fluorescent image directly overlaps with the bore of the needle visible in the bright field image (Figure 33). When performing our analysis, we rejected any overlays that did not meet this registration test. In addition, as the AA, dorsal aorta, and extraembryonic vessels were filled with dye, their patterns directly overlapped with these vessels in the bright field image, further demonstrating that no movement occurred between the recording of the brightfield and fluorescent data. When manually selecting the ventral and dorsal boundaries, we chose points along the outer surface of the heart, as it was easier to identify. Though these boundaries are not the inner lumen, we were consistent in our selection, allowing for a one to one comparison between control and LAL embryos.

We performed two-tailed, unpaired t-tests to determine differences in ICFP between groups. A p-value of less than 0.05 was considered significant.

5.4.2 Computational fluid dynamics model of an *in silico* LAL HH21 heart

5.4.2.1 Creation of geometric heart loop models

We based the geometry and proportions of our control HH21 heart loop model on a variety of anatomical imaging studies including serial histology (van den Berg and Moorman, 2011), scanning electron microscopy (Manner, 2000), micro computed tomography (Kim et al., 2011), magnetic resonance imaging (Yelbuz et al., 2003), and optical coherence tomography (Davis et al., 2008). The general "looped tube" structure was designed in Pro-Engineer (Parametric Technology Corp., Needham, MA) based on previous sketches and models (Manner, 2004; Patten, 1920). Atrial and ventricular bulbs, OT tapering, and the venous inlets (RVV, LVV, and both CCV) were added using our in-house sketch-based anatomical editing tool, SketchCAD. The heart geometry was modeled at end diastole. The model was completed and made CFD-ready using Geomagic Studio 10 (Geomagic Inc., Durham, NC). An *in silico* LAL surgery was performed by removing the presumptive left atrium volume and creating a smoothed surface to connect the left wall of the AV canal to the remaining right atrium, using our in-house surgical planning suite (Dur et al., 2011; Pekkan et al., 2008d). The finished control and LAL models were rendered in Geomagic Studio 10 (Geomagic Inc., Durham, NC) and exported into GAMBIT (ANSYS Inc., Cannonsburg, PA), to create a surface triangular mesh. The triangular mesh was imported into our in-house CFD pre-processor, which generates an unstructured 3D Cartesian immersed boundary mesh. The immersed boundary grid had a spatial resolution of 14 μm for both the control and LAL models.

5.4.2.2 Computational fluid dynamics

Blood flow through the embryonic heart was modeled using our in-house immersed boundary cardiovascular flow solver incorporating a validated second-order accurate multi-grid artificial

compressibility numerical method, described in our previous studies (Menon et al., 2012; Payli et al., 2007; Pekkan et al., 2009). Flow was simulated in terms of inlet normalized spatio-temporal units, on a high-resolution unstructured Cartesian immersed boundary grid with finite-difference numerical treatment. The objective of the CFD model was to determine if the geometric change of removing the left atrial volume was sufficient to alter ICFP and WSS. Therefore, we performed a steady-state simulation with fixed walls and no slip boundary conditions. The mean cardiac output of the HH21 chick embryo, 1.28 mm^3/s (Yoshigi et al., 2000), was used to compute inflow boundary conditions at each of the four venous inlets. As reliable data for the venous flow rates was not available, we prescribed an inflow distribution of 25/75 between the blood returned from the embryo by the CCV and blood returned from the vitelline bed by the VV (Hu et al., 1996). Further, a 50/50 split was specified between the cumulative inflows from the laterals. The Reynolds number (Re) of each of the CCV inlets was therefore 0.25, the Re of the VV inlets was 0.76, and the Re at the OT was 2. A plug flow profile was assigned to all inlets. An instantaneous mass-flow preserving outflow boundary condition was adopted. Blood was treated as a Newtonian fluid with constant hemodynamic properties ($\rho = 1060\ kg/m^3$, $\mu = 3.71 \times 10^{-3}$ Pa.s) (Al-Roubaie et al., 2011). In the case of the later stage model, which has only three inlets, the cardiac output remained the same, with 75% from the vitelline vein and 12.5% from each of the CCV. All other boundary conditions and assumptions were unchanged.

CFD simulations were conducted at Pittsburgh Supercomputing Center's Blacklight supercomputing cyber-infrastructure using a stable, parallel scalable high-performance version of our in-house CFD solver code. Each simulation cost an average of 22 hours at 32 core parallelism. Convergence of the steady inflow CFD solution was monitored using the running average velocity field, which converged to steady state quickly, due to the low physiological Re.

Chapter 6

Summary and conclusions

The research presented in this thesis expands the current knowledge of vascular morphogenesis and hemodynamic loading in the chick embryo. In particular, a quantitative approach was taken to provide the scientific field with reference values for describing cardiovascular development and its relationship to the hemodynamic environment. The results from multimodal imaging experiments combined with computational models revealed key features during vascular morphogenesis and further support the role of hemodynamics in shaping the cardiovascular system. The studies presented here can guide future experiments and models to explore biomechanical regulation of cardiovascular development and its function in the progression of congenital heart defects.

The embryonic AA represent a complex vascular network that undergoes rapid remodeling in an active biomechanical environment. Morphologic analysis showed that timing of AA transformations is not uniform, demonstrated by the presence of multiple AA patterns at HH21. CFD models of blood flow through the AA revealed that this period of instability coincides with an acute increase in AA WSS. The onset and duration of this WSS increase may trigger the rapid re-patterning of the AA to form the more stable HH24 configuration. Thus, key events such as AA selection likely occur during the period around HH21, representing a possible window where the system is vulnerable to morphogenetic errors leading to CHD.

AA selection was investigated using a novel optimization-based growth model, which incorporated the rotation of the OT under the hypothesis that this rotation preferentially directs blood flow to the eventual dominant arch of aorta. The growth model showed that the multiple AA configuration is reduced to a single AA in order to minimize total power expended. The

orientation of the OT was critical in determining the dominant AA, providing a possible link to great vessel defects observed clinically.

The development of predictive growth models requires experimental data for training and validation. OCT was used to perform time-lapse volumetric imaging of a vitelline artery in order to assess vascular growth at high spatial and temporal resolutions. Global growth trends and local morphogenesis were derived from morphometric analysis of the OCT data. This novel technique is the first to produce a quantitative description of local 3D vascular morphogenesis in the chick embryo. This method can be used to determine phenotypic consequences of hemodynamic or biologic interventions and test computational models of embryonic arterial growth.

The LAL intervention in the chick embryo has long been used as a prenatal model of hypoplastic left heart syndrome (HLHS). Clinical data has shown that HLHS is closely linked to flow defects in the fetal heart, leading to fetal intervention strategies to restore normal flow patterns. Using the chick embryo, alterations of intracardiac flow patterns after LAL were quantified. The intracardiac position of blood streams from the right common cardinal vein and right vitelline vein shifted significantly toward the ventral wall of the ventricle *in vivo*. An *in silico* CFD model of LAL reveled that WSS was reduced at the left atrioventricular canal and left side of the common ventricle, two sites commonly affected in HLHS. These results suggest that the changes in flow patterns are an early insult leading to the progression of HLHS after LAL.

Each study presented in this thesis lends itself to further investigation. CFD models of AA blood flow incorporating inlet velocity profiles after an intervention such as LAL would provide insight into the role of the disrupted intracardiac flow patterns on the downstream hemodynamic environment. Similarly, abnormal flow can be applied to more sophisticated

growth models to predict the morphogenetic response, particularly in cases where it cannot be readily observed *in vivo*.

Perhaps the greatest applications come from the long-term imaging and morphometric analysis techniques developed in Chapter 4. Growth data available from structural OCT imaging can be combined with velocity data obtained from Doppler OCT data or PIV measurements performed on the OCT B-scans. The combined data can then be used to deduce quantitative relationships between vascular morphogenesis and hemodynamic loading. In addition, the long-term imaging can be used to quantify the effects of hemodynamic interventions such as vitelline vein ligation, biologic manipulations including siRNA, or pharmaceutical agents. However, this method can only measure luminal growth and does not incorporate remodeling of the vascular wall. Therefore, complementary histochemical techniques are needed to provide a full view of vascular development. The time-lapse confocol protocols referenced in Chapter 4 may be well suited for this purpose.

In the embryo, the cardiovascular system is subjected to constant hemodynamic forces from the moment blood flow begins. This biomechanical environment continues to influence cardiac and vascular growth and remodeling until the final heart beat. Understanding the role of hemodynamics will improve diagnostic and treatment options for congenital heart disease as well as atherosclerosis, cerebral aneurysms, coronary artery disease, and a host of other conditions. While this thesis examined the embryonic cardiovascular system, the results and findings are relevant to the broader population. New strategies to treat or prevent cardiovascular disease are rapidly emerging, and many have roots in the study of the embryo.

References

Abu-Issa, R., Waldo, K., Kirby, M. L., 2004. Heart fields: one, two or more? Dev Biol. 272**,** 281-5.

Al-Roubaie, S., Jahnsen, E. D., Mohammed, M., Henderson-Toth, C., Jones, E. A., 2011. Rheology of embryonic avian blood. Am J Physiol Heart Circ Physiol. 301**,** H2473-81.

Al Naieb, S., Happel, C. M., Yelbuz, T. M., 2012. A detailed atlas of chick heart development in vivo. Ann Anat.

Alford, P. W., Humphrey, J. D., Taber, L. A., 2008. Growth and remodeling in a thick-walled artery model: effects of spatial variations in wall constituents. Biomech Model Mechanobiol. 7**,** 245-62.

Anderson, M. J., Pham, V. N., Vogel, A. M., Weinstein, B. M., Roman, B. L., 2008. Loss of unc45a precipitates arteriovenous shunting in the aortic arches. Dev Biol. 318**,** 258-67.

Anderson, R. H., Webb, S., Brown, N. A., Lamers, W., Moorman, A., 2003. Development of the heart: (3) formation of the ventricular outflow tracts, arterial valves, and intrapericardial arterial trunks. Heart. 89**,** 1110-8.

Asanuma, K., Magid, R., Johnson, C., Nerem, R. M., Galis, Z. S., 2003. Uniaxial strain upregulates matrix-degrading enzymes produced by human vascular smooth muscle cells. Am J Physiol Heart Circ Physiol. 284**,** H1778-84.

Atkins, D. L., Clark, E. B., Marvin, W. J., Jr., 1982. Foramen ovale/atrial septum area ratio: a marker of transatrial blood flow. Circulation. 66**,** 281-3.

Auerbach, R., Kubai, L., Knighton, D., Folkman, J., 1974. A simple procedure for the long-term cultivation of chicken embryos. Dev Biol. 41**,** 391-4.

Baba, K., Kawamura, T., Shibata, M., Sohirad, M., Kamiya, A., 1995. Capillary-tissue arrangement in the skeletal muscle optimized for oxygen transport in all mammals. Microvasc Res. 49**,** 163-79.

Backer, C. L., Mavroudis, C., 1997. Surgical approach to vascular rings. Adv Card Surg. 9**,** 29-64.

Bain, M. M., Fagan, A. J., Mullin, J. M., McNaught, I., McLean, J., Condon, B., 2007. Noninvasive monitoring of chick development in ovo using a 7T MRI system from day 12 of incubation through to hatching. J Magn Reson Imaging. 26**,** 198-201.

Bajolle, F., Zaffran, S., Kelly, R. G., Hadchouel, J., Bonnet, D., Brown, N. A., Buckingham, M. E., 2006. Rotation of the myocardial wall of the outflow tract is implicated in the normal positioning of the great arteries. Circulation Research. 98**,** 421-8.

Baker, K., Holtzman, N. G., Burdine, R. D., 2008. Direct and indirect roles for Nodal signaling in two axis conversions during asymmetric morphogenesis of the zebrafish heart. Proc Natl Acad Sci U S A. 105**,** 13924-9.

Barry, A., 1942. The intrinsic pulsation rates of fragments of the embryonic chick heart. Journal of Experimental Zoology. 91**,** 119-130.

Barry, A., 1951. The aortic arch derivatives in the human adult. Anatomical record. 111**,** 221-238.

Bartman, T., Walsh, E. C., Wen, K. K., McKane, M., Ren, J., Alexander, J., Rubenstein, P. A., Stainier, D. Y., 2004. Early myocardial function affects endocardial cushion development in zebrafish. PLoS Biol. 2**,** E129.

Bayer, I. M., Adamson, S. L., Langille, B. L., 1999. Atrophic remodeling of the artery-cuffed artery. Arterioscler Thromb Vasc Biol. 19**,** 1499-505.

Beloussov, L. V., 2008. Mechanically based generative laws of morphogenesis. Phys Biol. 5**,** 015009.
Beloussov, L. V., Grabovsky, V. I., 2006. Morphomechanics: goals, basic experiments and models. Int J Dev Biol. 50**,** 81-92.
Bergwerff, M., DeRuiter, M. C., Hall, S., Poelmann, R. E., Gittenberger-de Groot, A. C., 1999. Unique vascular morphology of the fourth aortic arches: possible implications for pathogenesis of type-B aortic arch interruption and anomalous right subclavian artery. Cardiovasc Res. 44**,** 185-96.
Bergwerff, M., DeRuiter, M. C., Poelmann, R. E., Gittenberger-de Groot, A. C., 1996. Onset of elastogenesis and downregulation of smooth muscle actin as distinguishing phenomena in artery differentiation in the chick embryo. Anat Embryol (Berl). 194**,** 545-57.
Bergwerff, M., Verberne, M. E., DeRuiter, M. C., Poelmann, R. E., Gittenberger-de Groot, A. C., 1998. Neural crest cell contribution to the developing circulatory system: implications for vascular morphology? Circ Res. 82**,** 221-31.
Berlien, Müller, 1997. Angewandte Lasermedizin. Ecomed.
Bharadwaj, K. N., Spitz, C., Shekhar, A., Yalcin, H. C., Butcher, J. T., 2012. Computational fluid dynamics of developing avian outflow tract heart valves. Ann Biomed Eng. 40**,** 2212-27.
Bland, J. M., Altman, D. G., 1986. Statistical methods for assessing agreement between two methods of clinical measurement. Lancet. 1**,** 307-10.
Bostrom, M. P., Hutchins, G. M., 1988. Arrested rotation of the outflow tract may explain double-outlet right ventricle. Circulation. 77**,** 1258-65.
Boulnois, J.-L., 1986. Photophysical processes in recent medical laser developments: A review. Lasers in Medical Science. 1**,** 47-66.
Bradshaw, L., Chaudhry, B., Hildreth, V., Webb, S., Henderson, D. J., 2009. Dual role for neural crest cells during outflow tract septation in the neural crest-deficient mutant Splotch(2H). Journal of Anatomy. 214**,** 245-57.
Brauner, C. J., Matey, V., Wilson, J. M., Bernier, N. J., Val, A. L., 2004. Transition in organ function during the evolution of air-breathing; insights from Arapaima gigas, an obligate air-breathing teleost from the Amazon. Journal of Experimental Biology. 207**,** 1433-8.
Bremer, J. L., 1928. Experiments on the aortic arches in the chick. Anatomical record. 37**,** 225-254.
Bremer, J. L., 1932. The presence and influence of two spiral streams in the heart of the chick embryo. American Journal of Anatomy. 49**,** 409-440.
Broekhuizen, M. L., Hogers, B., DeRuiter, M. C., Poelmann, R. E., Gittenberger-de Groot, A. C., Wladimiroff, J. W., 1999. Altered hemodynamics in chick embryos after extraembryonic venous obstruction. Ultrasound in obstetrics & gynecology : the official journal of the International Society of Ultrasound in Obstetrics and Gynecology. 13**,** 437-45.
Broekhuizen, M. L., Mast, F., Struijk, P. C., van der Bie, W., Mulder, P. G., Gittenberger-de Groot, A. C., Wladimiroff, J. W., 1993. Hemodynamic parameters of stage 20 to stage 35 chick embryo. Pediatr Res. 34**,** 44-6.
Brooks, A. R., Lelkes, P. I., Rubanyi, G. M., 2002. Gene expression profiling of human aortic endothelial cells exposed to disturbed flow and steady laminar flow. Physiol Genomics. 9**,** 27-41.
Bruneau, B. G., 2008. The developmental genetics of congenital heart disease. Nature. 451**,** 943-8.

Buffinton, C. M., Faas, D., Sedmera, D., 2013. Stress and strain adaptation in load-dependent remodeling of the embryonic left ventricle. Biomech Model Mechanobiol. 12**,** 1037-51.

Burggren, W. W., Keller, B. B., 1998. Development of Cardiovascular Systems: Molecules to Organisms. Cambridge University Press, New York.

Butcher, J. T., Markwald, R. R., 2007. Valvulogenesis: the moving target. Philos Trans R Soc Lond B Biol Sci. 362**,** 1489-503.

Butcher, J. T., Sedmera, D., Guldberg, R. E., Markwald, R. R., 2007. Quantitative volumetric analysis of cardiac morphogenesis assessed through micro-computed tomography. Dev Dyn. 236**,** 802-9.

Chen, B. P., Li, Y. S., Zhao, Y., Chen, K. D., Li, S., Lao, J., Yuan, S., Shyy, J. Y., Chien, S., 2001. DNA microarray analysis of gene expression in endothelial cells in response to 24-h shear stress. Physiol Genomics. 7**,** 55-63.

Chen, C.-Y., Menon, P. G., Kowalski, W., Pekkan, K., 2012. Time-resolved OCT-μPIV: a new microscopic PIV technique for noninvasive depth-resolved pulsatile flow profile acquisition. Experiments in Fluids. 54**,** 1-9.

Chen, C. Y., Patrick, M. J., Corti, P., Kowalski, W., Roman, B. L., Pekkan, K., 2011. Analysis of early embryonic great-vessel microcirculation in zebrafish using high-speed confocal μPIV. Biorheology. 48**,** 305-21.

Chien, S., 2007. Mechanotransduction and endothelial cell homeostasis: the wisdom of the cell. Am J Physiol Heart Circ Physiol. 292**,** H1209-24.

Chin, A. J., Weinberg, P. M., Barber, G., 1990. Subcostal two-dimensional echocardiographic identification of anomalous attachment of septum primum in patients with left atrioventricular valve underdevelopment. J Am Coll Cardiol. 15**,** 678-81.

Clark, E. B., Hu, N., 1982. Developmental hemodynamic changes in the chick embryo from stage 18 to 27. Circulation Research. 51**,** 810-5.

Clark, E. B., Hu, N., Dummett, J. L., Vandekieft, G. K., Olson, C., Tomanek, R., 1986. Ventricular function and morphology in chick embryo from stages 18 to 29. Am J Physiol. 250**,** H407-13.

Clark, E. B., Hu, N., Frommelt, P., Vandekieft, G. K., Dummett, J. L., Tomanek, R. J., 1989. Effect of increased pressure on ventricular growth in stage 21 chick embryos. Am J Physiol. 257**,** H55-61.

Coffin, J. D., Poole, T. J., 1988. Embryonic vascular development: immunohistochemical identification of the origin and subsequent morphogenesis of the major vessel primordia in quail embryos. Development. 102**,** 735-48.

Collette, Y., Siarry, P., 2003. Multiobjective optimization : principles and case studies. Springer, Berlin ; New York.

Congdon, E. D., Wang, H. D., 1926. The mechanical processes concerned in the formation of the different types of aortic arches in the chick and pig and the divergent early development of their pulmonary arches. American Journal of Anatomy. 37**,** 499-520.

Corti, P., Young, S., Chen, C. Y., Patrick, M. J., Rochon, E. R., Pekkan, K., Roman, B. L., 2011. Interaction between alk1 and blood flow in the development of arteriovenous malformations. Development. 138**,** 1573-82.

Culver, J. C., Dickinson, M. E., 2010. The effects of hemodynamic force on embryonic development. Microcirculation. 17**,** 164-78.

Davis, A., Izatt, J., Rothenberg, F., 2009. Quantitative measurement of blood flow dynamics in embryonic vasculature using spectral Doppler velocimetry. Anat Rec (Hoboken). 292**,** 311-9.

Davis, A. M., Rothenberg, F. G., Shepherd, N., Izatt, J. A., 2008. In vivo spectral domain optical coherence tomography volumetric imaging and spectral Doppler velocimetry of early stage embryonic chicken heart development. J Opt Soc Am A Opt Image Sci Vis. 25**,** 3134-43.

De Bellard, M. E., Barembaum, M., Arman, O., Bronner-Fraser, M., 2007. Lunatic fringe causes expansion and increased neurogenesis of trunk neural tube and neural crest populations. Neuron Glia Biol. 3**,** 93-103.

De la Cruz, M. V., Gimenez-Ribotta, M., Saravalli, O., Cayre, R., 1983. The contribution of the inferior endocardial cushion of the atrioventricular canal to cardiac septation and to the development of the atrioventricular valves: study in the chick embryo. American Journal of Anatomy. 166**,** 63-72.

de la Cruz, M. V., Markwald, R. R., Embryological development of the ventricular inlets. Septation and atrioventricular valve apparatus. In: M. V. de la Cruz, R. R. Markwald, Eds.), Living morphogenesis of the heart. Birkhauser, Boston, MA, 2000, pp. 131-157.

de la Cruz, M. V., Sanchez Gomez, C., Arteaga, M. M., Arguello, C., 1977. Experimental study of the development of the truncus and the conus in the chick embryo. J Anat. 123**,** 661-86.

de la Pompa, J. L., Timmerman, L. A., Takimoto, H., Yoshida, H., Elia, A. J., Samper, E., Potter, J., Wakeham, A., Marengere, L., Langille, B. L., Crabtree, G. R., Mak, T. W., 1998. Role of the NF-ATc transcription factor in morphogenesis of cardiac valves and septum. Nature. 392**,** 182-6.

deAlmeida, A., McQuinn, T., Sedmera, D., 2007. Increased ventricular preload is compensated by myocyte proliferation in normal and hypoplastic fetal chick left ventricle. Circulation Research. 100**,** 1363-70.

DeGroff, C. G., Thornburg, B. L., Pentecost, J. O., Thornburg, K. L., Gharib, M., Sahn, D. J., Baptista, A., 2003. Flow in the early embryonic human heart: a numerical study. Pediatr Cardiol. 24**,** 375-80.

DeRuiter, M. C., Poelmann, R. E., Mentink, M. M., Vaniperen, L., Gittenberger-De Groot, A. C., 1993. Early formation of the vascular system in quail embryos. Anat Rec. 235**,** 261-74.

Dor, X., Corone, P., 1985. Migration and torsions of the conotruncus in the chick embryo heart: observational evidence and conclusions drawn from experimental intervention. Heart Vessels. 1**,** 195-211.

Dunker, N., Krieglstein, K., 2002. Tgfbeta2 -/- Tgfbeta3 -/- double knockout mice display severe midline fusion defects and early embryonic lethality. Anat Embryol (Berl). 206**,** 73-83.

Dur, O., Coskun, S. T., Coskun, K. O., Frakes, D., Kara, L. B., Pekkan, K., 2011. Computer-Aided Patient-Specific Coronary Artery Graft Design Improvements Using CFD Coupled Shape Optimizer. Cardiovasc Eng Technol. 2**,** 35-47.

Dur, O., Wang, Y., Patrick, M., Tinney, J., Keller, B., Pekkan, K., Correlation of wall shear stress and pharyngeal arch lumen diameter during early embryonic development in the chick. BMES Annual Fall Meeting, Pittsburgh, PA, 2009.

Echtler, K., Stark, K., Lorenz, M., Kerstan, S., Walch, A., Jennen, L., Rudelius, M., Seidl, S., Kremmer, E., Emambokus, N. R., von Bruehl, M. L., Frampton, J., Isermann, B., Genzel-Boroviczeny, O., Schreiber, C., Mehilli, J., Kastrati, A., Schwaiger, M., Shivdasani, R.

A., Massberg, S., 2010. Platelets contribute to postnatal occlusion of the ductus arteriosus. Nat Med. 16**,** 75-82.

Egorova, A. D., Khedoe, P. P., Goumans, M. J., Yoder, B. K., Nauli, S. M., ten Dijke, P., Poelmann, R. E., Hierck, B. P., 2011a. Lack of primary cilia primes shear-induced endothelial-to-mesenchymal transition. Circ Res. 108**,** 1093-101.

Egorova, A. D., Van der Heiden, K., Van de Pas, S., Vennemann, P., Poelma, C., DeRuiter, M. C., Goumans, M. J., Gittenberger-de Groot, A. C., ten Dijke, P., Poelmann, R. E., Hierck, B. P., 2011b. Tgfbeta/Alk5 signaling is required for shear stress induced klf2 expression in embryonic endothelial cells. Dev Dyn. 240**,** 1670-80.

El-Ghali, N., Rabadi, M., Ezin, A. M., De Bellard, M. E., 2010. New methods for chicken embryo manipulations. Microsc Res Tech. 73**,** 58-66.

Evans, D. H., Piermarini, P. M., Choe, K. P., 2005. The multifunctional fish gill: dominant site of gas exchange, osmoregulation, acid-base regulation, and excretion of nitrogenous waste. Physiol Rev. 85**,** 97-177.

Fang, Q., Boas, D., 2009. Tetrahedral mesh generation from volumetric binary and gray-scale images. Proceedings of IEEE International Symposium on Biomedical Imaging 2009. 1142-1145.

Feinstein, J. A., Benson, D. W., Dubin, A. M., Cohen, M. S., Maxey, D. M., Mahle, W. T., Pahl, E., Villafane, J., Bhatt, A. B., Peng, L. F., Johnson, B. A., Marsden, A. L., Daniels, C. J., Rudd, N. A., Caldarone, C. A., Mussatto, K. A., Morales, D. L., Ivy, D. D., Gaynor, J. W., Tweddell, J. S., Deal, B. J., Furck, A. K., Rosenthal, G. L., Ohye, R. G., Ghanayem, N. S., Cheatham, J. P., Tworetzky, W., Martin, G. R., 2012. Hypoplastic left heart syndrome: current considerations and expectations. J Am Coll Cardiol. 59**,** S1-42.

Feit, L. R., Copel, J. A., Kleinman, C. S., 1991. Foramen ovale size in the normal and abnormal human fetal heart: an indicator of transatrial flow physiology. Ultrasound Obstet Gynecol. 1**,** 313-9.

Fercher, A. F., Drexler, W., Hitzenberger, C. K., Lasser, T., 2003. Optical coherence tomography - principles and applications. Reports on Progress in Physics. 66**,** 239-303.

Figueroa, C. A., Baek, S., Taylor, C. A., Humphrey, J. D., 2009. A Computational Framework for Fluid-Solid-Growth Modeling in Cardiovascular Simulations. Comput Methods Appl Mech Eng. 198**,** 3583-3602.

Filas, B. A., Efimov, I. R., Taber, L. A., 2007. Optical coherence tomography as a tool for measuring morphogenetic deformation of the looping heart. Anat Rec (Hoboken). 290**,** 1057-68.

Flynn, M. E., Pikalow, A. S., Kimmelman, R. S., Searls, R. L., 1991. The mechanism of cervical flexure formation in the chick. Anat Embryol (Berl). 184**,** 411-20.

Forouhar, A. S., Liebling, M., Hickerson, A., Nasiraei-Moghaddam, A., Tsai, H. J., Hove, J. R., Fraser, S. E., Dickinson, M. E., Gharib, M., 2006. The embryonic vertebrate heart tube is a dynamic suction pump. Science. 312**,** 751-3.

Franz, T., 1989. Persistent truncus arteriosus in the Splotch mutant mouse. Anat Embryol (Berl). 180**,** 457-64.

Friedman, S., Murphy, L., Ash, R., 1951. Aortic atresia with hypoplasia of the left heart and aortic arch. J Pediatr. 38**,** 354-68.

Fung, Y. C., 1990. Biomechanics : motion, flow, stress, and growth. Springer-Verlag, New York.

Fung, Y. C., 1997. Biomechanics : circulation. Springer, New York.

Fung, Y. C., Liu, S. Q., 1991. Changes of zero-stress state of rat pulmonary arteries in hypoxic hypertension. J Appl Physiol (1985). 70**,** 2455-70.
Gargesha, M., Jenkins, M. W., Wilson, D. L., Rollins, A. M., 2009. High temporal resolution OCT using image-based retrospective gating. Opt Express. 17**,** 10786-99.
Gessner, I. H., 1966. Spectrum of congenital cardiac anomalies produced in chick embryos by mechanical interference with cardiogenesis. Circulation Research. 18**,** 625-33.
Girerd, X., London, G., Boutouyrie, P., Mourad, J. J., Safar, M., Laurent, S., 1996. Remodeling of the radial artery in response to a chronic increase in shear stress. Hypertension. 27**,** 799-803.
Gleason, R. L., Humphrey, J. D., 2004. A mixture model of arterial growth and remodeling in hypertension: altered muscle tone and tissue turnover. J Vasc Res. 41**,** 352-63.
Glickman, N. S., Yelon, D., 2002. Cardiac development in zebrafish: coordination of form and function. Semin Cell Dev Biol. 13**,** 507-13.
Go, A. S., Mozaffarian, D., Roger, V. L., Benjamin, E. J., Berry, J. D., Borden, W. B., Bravata, D. M., Dai, S., Ford, E. S., Fox, C. S., Franco, S., Fullerton, H. J., Gillespie, C., Hailpern, S. M., Heit, J. A., Howard, V. J., Huffman, M. D., Kissela, B. M., Kittner, S. J., Lackland, D. T., Lichtman, J. H., Lisabeth, L. D., Magid, D., Marcus, G. M., Marelli, A., Matchar, D. B., McGuire, D. K., Mohler, E. R., Moy, C. S., Mussolino, M. E., Nichol, G., Paynter, N. P., Schreiner, P. J., Sorlie, P. D., Stein, J., Turan, T. N., Virani, S. S., Wong, N. D., Woo, D., Turner, M. B., 2013. Heart disease and stroke statistics--2013 update: a report from the American Heart Association. Circulation. 127**,** e6-e245.
Goor, D. A., Edwards, J. E., 1973. The spectrum of transposition of the great arteries: with specific reference to developmental anatomy of the conus. Circulation. 48**,** 406-15.
Groenendijk, B. C., Hierck, B. P., Gittenberger-De Groot, A. C., Poelmann, R. E., 2004. Development-related changes in the expression of shear stress responsive genes KLF-2, ET-1, and NOS-3 in the developing cardiovascular system of chicken embryos. Dev Dyn. 230**,** 57-68.
Grossfeld, P., Ye, M., Harvey, R., 2009. Hypoplastic left heart syndrome: new genetic insights. J Am Coll Cardiol. 53**,** 1072-4.
Grote, K., Flach, I., Luchtefeld, M., Akin, E., Holland, S. M., Drexler, H., Schieffer, B., 2003. Mechanical stretch enhances mRNA expression and proenzyme release of matrix metalloproteinase-2 (MMP-2) via NAD(P)H oxidase-derived reactive oxygen species. Circ Res. 92**,** e80-6.
Gruionu, G., Hoying, J. B., Pries, A. R., Secomb, T. W., 2005. Structural remodeling of mouse gracilis artery after chronic alteration in blood supply. Am J Physiol Heart Circ Physiol. 288**,** H2047-54.
Guyton, J. R., Hartley, C. J., 1985. Flow restriction of one carotid artery in juvenile rats inhibits growth of arterial diameter. Am J Physiol. 248**,** H540-6.
Hacking, W. J., VanBavel, E., Spaan, J. A., 1996. Shear stress is not sufficient to control growth of vascular networks: a model study. Am J Physiol. 270**,** H364-75.
Hamburger, V., Hamilton, H. L., 1951. A Series of Normal Stages in the Development of the Chick Embryo. Journal of Morphology. 88**,** 49-92.
Hanke, M., 2004. Benchmarking FEMLAB 3.0a: Laminar Flows in 2D, Report No. 2004:01.
Happel, C. M., Thrane, L., Thommes, J., Manner, J., Yelbuz, T. M., 2011. Integration of an optical coherence tomography (OCT) system into an examination incubator to facilitate

in vivo imaging of cardiovascular development in higher vertebrate embryos under stable physiological conditions. Ann Anat. 193**,** 425-35.
Henning, A. L., Jiang, M. X., Yalcin, H. C., Butcher, J. T., 2011. Quantitative three-dimensional imaging of live avian embryonic morphogenesis via micro-computed tomography. Dev Dyn. 240**,** 1949-57.
Hinton, R. B., Jr., Lincoln, J., Deutsch, G. H., Osinska, H., Manning, P. B., Benson, D. W., Yutzey, K. E., 2006. Extracellular matrix remodeling and organization in developing and diseased aortic valves. Circ Res. 98**,** 1431-8.
Hinton, R. B., Jr., Martin, L. J., Tabangin, M. E., Mazwi, M. L., Cripe, L. H., Benson, D. W., 2007. Hypoplastic left heart syndrome is heritable. J Am Coll Cardiol. 50**,** 1590-5.
Hinton, R. B., Martin, L. J., Rame-Gowda, S., Tabangin, M. E., Cripe, L. H., Benson, D. W., 2009. Hypoplastic left heart syndrome links to chromosomes 10q and 6q and is genetically related to bicuspid aortic valve. J Am Coll Cardiol. 53**,** 1065-71.
Hiruma, T., Hirakow, R., 1995. Formation of the pharyngeal arch arteries in the chick embryo. Observations of corrosion casts by scanning electron microscopy. Anat Embryol (Berl). 191**,** 415-23.
Hogers, B., DeRuiter, M. C., Baasten, A. M., Gittenberger-de Groot, A. C., Poelmann, R. E., 1995. Intracardiac blood flow patterns related to the yolk sac circulation of the chick embryo. Circ Res. 76**,** 871-7.
Hogers, B., DeRuiter, M. C., Gittenberger-de Groot, A. C., Poelmann, R. E., 1997. Unilateral vitelline vein ligation alters intracardiac blood flow patterns and morphogenesis in the chick embryo. Circ Res. 80**,** 473-81.
Hogers, B., DeRuiter, M. C., Gittenberger-de Groot, A. C., Poelmann, R. E., 1999. Extraembryonic venous obstructions lead to cardiovascular malformations and can be embryo lethal. Cardiovasc Res. 41**,** 87-99.
Holmes, W. M., McCabe, C., Mullin, J. M., Condon, B., Bain, M. M., 2009. In ovo non-invasive quantification of the myocardial function and mass of chick embryos using magnetic resonance imaging. NMR Biomed. 22**,** 745-52.
Holzapfel, G. A., Gasser, T. C., Ogden, R. W., 2000. A new constitutive framework for arterial wall mechanics and a comparative study of material models. Journal of Elasticity. 61**,** 1-48.
Holzapfel, G. A., Ogden, R. W., 2010. Constitutive modelling of arteries. Proceedings of the Royal Society a-Mathematical Physical and Engineering Sciences. 466**,** 1551-1596.
Hove, J. R., Koster, R. W., Forouhar, A. S., Acevedo-Bolton, G., Fraser, S. E., Gharib, M., 2003. Intracardiac fluid forces are an essential epigenetic factor for embryonic cardiogenesis. Nature. 421**,** 172-7.
Hu, N., Christensen, D. A., Agrawal, A. K., Beaumont, C., Clark, E. B., Hawkins, J. A., 2009. Dependence of aortic arch morphogenesis on intracardiac blood flow in the left atrial ligated chick embryo. Anat Rec (Hoboken). 292**,** 652-60.
Hu, N., Clark, E. B., 1989. Hemodynamics of the stage 12 to stage 29 chick embryo. Circulation Research. 65**,** 1665-70.
Hu, N., Ngo, T. D., Clark, E. B., 1996. Distribution of blood flow between embryo and vitelline bed in the stage 18, 21 and 24 chick embryo. Cardiovasc Res. 31 Spec No**,** E127-31.
Huang, D., Swanson, E. A., Lin, C. P., Schuman, J. S., Stinson, W. G., Chang, W., Hee, M. R., Flotte, T., Gregory, K., Puliafito, C. A., et al., 1991. Optical coherence tomography. Science. 254**,** 1178-81.

Hudetz, A. G., Kiani, M. F., 1992. The role of wall shear stress in microvascular network adaptation. Adv Exp Med Biol. 316**,** 31-9.
Hughes, A. F. W., 1934. On the development of the blood vessels in the head of the chick. Philosophical Transactions of the Royal Society of London Series B-Biological Sciences. 224**,** 75-U42.
Hughes, A. F. W., 1943. The histogenesis of the arteries of the chick embryo. Journal of Anatomy. 77**,** 266-287.
Hughes, G. M., Morgan, M., 1973. Structure of Fish Gills in Relation to Their Respiratory Function. Biological Reviews of the Cambridge Philosophical Society. 48**,** 419-475.
Humphrey, J. D., 1999. Remodeling of a collagenous tissue at fixed lengths. J Biomech Eng. 121**,** 591-7.
Hurlstone, A. F., Haramis, A. P., Wienholds, E., Begthel, H., Korving, J., Van Eeden, F., Cuppen, E., Zivkovic, D., Plasterk, R. H., Clevers, H., 2003. The Wnt/beta-catenin pathway regulates cardiac valve formation. Nature. 425**,** 633-7.
Intengan, H. D., Deng, L. Y., Li, J. S., Schiffrin, E. L., 1999a. Mechanics and composition of human subcutaneous resistance arteries in essential hypertension. Hypertension. 33**,** 569-74.
Intengan, H. D., Thibault, G., Li, J. S., Schiffrin, E. L., 1999b. Resistance artery mechanics, structure, and extracellular components in spontaneously hypertensive rats : effects of angiotensin receptor antagonism and converting enzyme inhibition. Circulation. 100**,** 2267-75.
Isogai, S., Horiguchi, M., Weinstein, B. M., 2001. The vascular anatomy of the developing zebrafish: an atlas of embryonic and early larval development. Developmental biology. 230**,** 278-301.
Jackson, Z. S., Gotlieb, A. I., Langille, B. L., 2002. Wall tissue remodeling regulates longitudinal tension in arteries. Circ Res. 90**,** 918-25.
Jaffee, O. C., 1965. Hemodynamic Factors in the Development of the Chick Embryo Heart. Anat Rec. 151**,** 69-75.
Jaffee, O. C., 1967. The development of the arterial outflow tract in the chick embryo heart. Anat Rec. 158**,** 35-42.
Kajic, V., Esmaeelpour, M., Glittenberg, C., Kraus, M. F., Honegger, J., Othara, R., Binder, S., Fujimoto, J. G., Drexler, W., 2013. Automated three-dimensional choroidal vessel segmentation of 3D 1060 nm OCT retinal data. Biomed Opt Express. 4**,** 134-50.
Kamei, M., Weinstein, B. M., 2005. Long-term time-lapse fluorescence imaging of developing zebrafish. Zebrafish. 2**,** 113-23.
Kamino, K., Hirota, A., Fujii, S., 1981. Localization of pacemaking activity in early embryonic heart monitored using voltage-sensitive dye. Nature. 290**,** 595-7.
Kamiya, A., Takeda, S., Shibata, M., 1987. Optimum capillary number for oxygen delivery to tissue in man. Bull Math Biol. 49**,** 351-61.
Kamiya, A., Togawa, T., 1980. Adaptive regulation of wall shear stress to flow change in the canine carotid artery. Am J Physiol. 239**,** H14-21.
Kamiya, A., Wakayama, H., Baba, K., 1993. Optimality analysis of vascular-tissue system in mammals for oxygen transport. J Theor Biol. 162**,** 229-42.
Kardong, K. V., 2009. Vertebrates : comparative anatomy, function, evolution. McGraw-Hill Higher Education, Boston.

Kassab, G. S., Fung, Y. C., 1995. The pattern of coronary arteriolar bifurcations and the uniform shear hypothesis. Annals of Biomedical Engineering. 23**,** 13-20.
Kastschenko, N., 1887. Das schlundspaltengebiet des Huhnchens. Arch f anat u Physiol, Anat Abt. 258-300.
Keenan, R. L., Rodbard, S., 1973. Competition between collateral vessels. Cardiovasc Res. 7**,** 670-5.
Keller, B. B., Hu, N., Serrino, P. J., Clark, E. B., 1991. Ventricular pressure-area loop characteristics in the stage 16 to 24 chick embryo. Circ Res. 68**,** 226-31.
Keller, B. B., Yoshigi, M., Tinney, J. P., 1997. Ventricular-vascular uncoupling by acute conotruncal occlusion in the stage 21 chick embryo. Am J Physiol. 273**,** H2861-6.
Khanin, M. A., Bukharov, I. B., 1994. Optimal structure of the microcirculatory bed. J Theor Biol. 169**,** 267-73.
Kim, J. S., Min, J., Recknagel, A. K., Riccio, M., Butcher, J. T., 2011. Quantitative three-dimensional analysis of embryonic chick morphogenesis via microcomputed tomography. Anat Rec (Hoboken). 294**,** 1-10.
Kirby, M. L., Gale, T. F., Stewart, D. E., 1983. Neural crest cells contribute to normal aorticopulmonary septation. Science. 220**,** 1059-61.
Kirby, M. L., Hunt, P., Wallis, K., Thorogood, P., 1997. Abnormal patterning of the aortic arch arteries does not evoke cardiac malformations. Dev Dyn. 208**,** 34-47.
Kowalski, W. J., Dur, O., Wang, Y., Patrick, M. J., Tinney, J. P., Keller, B. B., Pekkan, K., 2013. Critical transitions in early embryonic aortic arch patterning and hemodynamics. PLoS One. 8**,** e60271.
Kowalski, W. J., Teslovich, N. C., Dur, O., Keller, B. B., Pekkan, K., 2012. Computational hemodynamic optimization predicts dominant aortic arch selection is driven by embryonic outflow tract orientation in the chick embryo. Biomech Model Mechanobiol. 11**,** 1057-73.
Kulesa, P. M., Bailey, C. M., Cooper, C., Fraser, S. E., 2010. In ovo live imaging of avian embryos. Cold Spring Harb Protoc. 2010**,** pdb prot5446.
Kuratani, S. C., Kirby, M. L., 1991. Initial migration and distribution of the cardiac neural crest in the avian embryo: an introduction to the concept of the circumpharyngeal crest. Am J Anat. 191**,** 215-27.
LaBarbera, M., 1990. Principles of design of fluid transport systems in zoology. Science. 249**,** 992-1000.
Langille, B. L., O'Donnell, F., 1986. Reductions in arterial diameter produced by chronic decreases in blood flow are endothelium-dependent. Science. 231**,** 405-7.
le Noble, F., Klein, C., Tintu, A., Pries, A., Buschmann, I., 2008. Neural guidance molecules, tip cells, and mechanical factors in vascular development. Cardiovasc Res. 78**,** 232-41.
le Noble, F., Moyon, D., Pardanaud, L., Yuan, L., Djonov, V., Matthijsen, R., Breant, C., Fleury, V., Eichmann, A., 2004. Flow regulates arterial-venous differentiation in the chick embryo yolk sac. Development. 131**,** 361-75.
Lee, Y. H., Saint-Jeannet, J. P., 2009. Characterization of molecular markers to assess cardiac cushions formation in Xenopus. Dev Dyn. 238**,** 3257-65.
Lehoux, S., Castier, Y., Tedgui, A., 2006. Molecular mechanisms of the vascular responses to haemodynamic forces. J Intern Med. 259**,** 381-92.

Levine, A. J., Munoz-Sanjuan, I., Bell, E., North, A. J., Brivanlou, A. H., 2003. Fluorescent labeling of endothelial cells allows in vivo, continuous characterization of the vascular development of Xenopus laevis. Dev Biol. 254**,** 50-67.

Li, D., Robertson, A. M., 2009. A structural multi-mechanism damage model for cerebral arterial tissue. J Biomech Eng. 131**,** 101013.

Liebau, G., 1957. [Significance of forces of inertia in the dynamics of blood circulation]. Z Kreislaufforsch. 46**,** 428-38.

Liem, K. F., Bemis, W. E., Walker, W. F., Grande, L., 2001. Functional anatomy of the vertebrates : an evolutionary perspective. Thomson Brooks/Cole, Belmont, CA.

Lin, I. E., Taber, L. A., 1995. A model for stress-induced growth in the developing heart. J Biomech Eng. 117**,** 343-9.

Liu, A., Nickerson, A., Troyer, A., Yin, X., Cary, R., Thornburg, K., Wang, R., Rugonyi, S., 2011. Quantifying blood flow and wall shear stresses in the outflow tract of chick embryonic hearts. Comput Struct. 89**,** 855-867.

Liu, A., Yin, X., Shi, L., Li, P., Thornburg, K. L., Wang, R., Rugonyi, S., 2012. Biomechanics of the chick embryonic heart outflow tract at HH18 using 4D optical coherence tomography imaging and computational modeling. PLoS One. 7**,** e40869.

Liu, C., Liu, W., Palie, J., Lu, M. F., Brown, N. A., Martin, J. F., 2002. Pitx2c patterns anterior myocardium and aortic arch vessels and is required for local cell movement into atrioventricular cushions. Development. 129**,** 5081-91.

Lohr, J. L., Yost, H. J., 2000. Vertebrate model systems in the study of early heart development: Xenopus and zebrafish. Am J Med Genet. 97**,** 248-57.

Lomonico, M. P., Bostrom, M. P., Moore, G. W., Hutchins, G. M., 1988. Arrested rotation of the outflow tract may explain tetralogy of Fallot and transposition of the great arteries. Pediatr Pathol. 8**,** 267-81.

Lu, X., Zhao, J. B., Wang, G. R., Gregersen, H., Kassab, G. S., 2001. Remodeling of the zero-stress state of femoral arteries in response to flow overload. Am J Physiol Heart Circ Physiol. 280**,** H1547-59.

Lucitti, J. L., Tobita, K., Keller, B. B., 2005. Arterial hemodynamics and mechanical properties after circulatory intervention in the chick embryo. Journal of Experimental Biology. 208**,** 1877-85.

Lucitti, J. L., Visconti, R., Novak, J., Keller, B. B., 2006. Increased arterial load alters aortic structural and functional properties during embryogenesis. Am J Physiol Heart Circ Physiol. 291**,** H1919-26.

Ma, Z., Liu, A., Yin, X., Troyer, A., Thornburg, K., Wang, R. K., Rugonyi, S., 2010. Measurement of absolute blood flow velocity in outflow tract of HH18 chicken embryo based on 4D reconstruction using spectral domain optical coherence tomography. Biomed Opt Express. 1**,** 798-811.

Manner, J., 2000. Cardiac looping in the chick embryo: a morphological review with special reference to terminological and biomechanical aspects of the looping process. Anat Rec. 259**,** 248-62.

Manner, J., 2004. On rotation, torsion, lateralization, and handedness of the embryonic heart loop: new insights from a simulation model for the heart loop of chick embryos. Anat Rec A Discov Mol Cell Evol Biol. 278**,** 481-92.

Manner, J., Merkel, N., 2007. Early morphogenesis of the sinuatrial region of the chick heart: a contribution to the understanding of the pathogenesis of direct pulmonary venous

connections to the right atrium and atrial septal defects in hearts with right isomerism of the atrial appendages. Anat Rec (Hoboken). 290**,** 168-80.
Manner, J., Seidl, W., Steding, G., 1993. Correlation between the Embryonic Head Flexures and Cardiac Development - an Experimental-Study in Chick-Embryos. Anatomy and Embryology. 188**,** 269-285.
Manner, J., Seidl, W., Steding, G., 1995. Formation of the Cervical Flexure - an Experimental-Study on Chick-Embryos. Acta Anatomica. 152**,** 1-10.
Manner, J., Thrane, L., Norozi, K., Yelbuz, T. M., 2008. High-resolution in vivo imaging of the cross-sectional deformations of contracting embryonic heart loops using optical coherence tomography. Dev Dyn. 237**,** 953-61.
Manner, J., Wessel, A., Yelbuz, T. M., 2010. How does the tubular embryonic heart work? Looking for the physical mechanism generating unidirectional blood flow in the valveless embryonic heart tube. Dev Dyn. 239**,** 1035-46.
Markwald, R. R., Fitzharris, T. P., Manasek, F. J., 1977. Structural development of endocardial cushions. The American journal of anatomy. 148**,** 85-119.
Marler, R. T., Arora, J. S., 2004. Survey of multi-objective optimization methods for engineering. Structural and Multidisciplinary Optimization. 26**,** 369-395.
Martinsen, B. J., 2005. Reference guide to the stages of chick heart embryology. Dev Dyn. 233**,** 1217-37.
McBride, K. L., Zender, G. A., Fitzgerald-Butt, S. M., Koehler, D., Menesses-Diaz, A., Fernbach, S., Lee, K., Towbin, J. A., Leal, S., Belmont, J. W., 2009. Linkage analysis of left ventricular outflow tract malformations (aortic valve stenosis, coarctation of the aorta, and hypoplastic left heart syndrome). Eur J Hum Genet. 17**,** 811-9.
McCormick, S. M., Eskin, S. G., McIntire, L. V., Teng, C. L., Lu, C. M., Russell, C. G., Chittur, K. K., 2001. DNA microarray reveals changes in gene expression of shear stressed human umbilical vein endothelial cells. Proc Natl Acad Sci U S A. 98**,** 8955-60.
McDougall, S. R., Anderson, A. R., Chaplain, M. A., Sherratt, J. A., 2002. Mathematical modelling of flow through vascular networks: implications for tumour-induced angiogenesis and chemotherapy strategies. Bull Math Biol. 64**,** 673-702.
McElhinney, D. B., Tworetzky, W., Lock, J. E., 2010. Current status of fetal cardiac intervention. Circulation. 121**,** 1256-63.
Meeson, A., Palmer, M., Calfon, M., Lang, R., 1996. A relationship between apoptosis and flow during programmed capillary regression is revealed by vital analysis. Development. 122**,** 3929-38.
Menon, P. G., Sotiropoulos, F., Pekkan, K., CFD challenge: Computational hemodynamics analysis of patient-specific internal carotid artery aneursym using an in-house finite difference cardiovascular flow solver. ASME Summer Bioengineering Conference, Fajardo, Puerto Rico, 2012.
Mercola, M., Levin, M., 2001. Left-right asymmetry determination in vertebrates. Annu Rev Cell Dev Biol. 17**,** 779-805.
Miller, C. E., Wong, C. L., Sedmera, D., 2003. Pressure overload alters stress-strain properties of the developing chick heart. Am J Physiol Heart Circ Physiol. 285**,** H1849-56.
Milnor, W. R., 1989. Hemodynamics. Williams & Wilkins, Baltimore.
Mjaatvedt, C. H., Nakaoka, T., Moreno-Rodriguez, R., Norris, R. A., Kern, M. J., Eisenberg, C. A., Turner, D., Markwald, R. R., 2001. The outflow tract of the heart is recruited from a novel heart-forming field. Dev Biol. 238**,** 97-109.

Molin, D. G., DeRuiter, M. C., Wisse, L. J., Azhar, M., Doetschman, T., Poelmann, R. E., Gittenberger-de Groot, A. C., 2002. Altered apoptosis pattern during pharyngeal arch artery remodelling is associated with aortic arch malformations in Tgfbeta2 knock-out mice. Cardiovasc Res. 56**,** 312-22.

Molin, D. G., Poelmann, R. E., DeRuiter, M. C., Azhar, M., Doetschman, T., Gittenberger-de Groot, A. C., 2004. Transforming growth factor beta-SMAD2 signaling regulates aortic arch innervation and development. Circ Res. 95**,** 1109-17.

Mujumdar, R. B., Ernst, L. A., Mujumdar, S. R., Lewis, C. J., Waggoner, A. S., 1993. Cyanine dye labeling reagents: sulfoindocyanine succinimidyl esters. Bioconjug Chem. 4**,** 105-11.

Murray, C. D., 1926. The Physiological Principle of Minimum Work: I. The Vascular System and the Cost of Blood Volume. Proc Natl Acad Sci U S A. 12**,** 207-14.

Myers, C. D., Mattix, K., Presson, R. G., Jr., Vijay, P., Maynes, D., Litwak, K. N., Brown, J. W., Rodefeld, M. D., 2006. Twenty-four hour cardiopulmonary stability in a model of assisted newborn Fontan circulation. Ann Thorac Surg. 81**,** 264-70; discussion 270-1.

Nieuwkoop, P. D., Faber, J., 1994. Normal table of Xenopus laevis (Daudin) : a systematical and chronological survey of the development from the fertilized egg till the end of metamorphosis. Garland Pub., New York.

Nikmanesh, M., Shi, Z. D., Tarbell, J. M., 2012. Heparan sulfate proteoglycan mediates shear stress-induced endothelial gene expression in mouse embryonic stem cell-derived endothelial cells. Biotechnol Bioeng. 109**,** 583-94.

Nissen, R., Cardinale, G. J., Udenfriend, S., 1978. Increased turnover of arterial collagen in hypertensive rats. Proc Natl Acad Sci U S A. 75**,** 451-3.

Noden, D. M., 1991. Origins and patterning of avian outflow tract endocardium. Development. 111**,** 867-76.

Noonan, J. A., Nadas, A. S., 1958. The hypoplastic left heart syndrome; an analysis of 101 cases. Pediatr Clin North Am. 5**,** 1029-56.

Okamoto, N., Akimoto, N., Hidaka, N., Shoji, S., Sumida, H., 2010. Formal genesis of the outflow tracts of the heart revisited: previous works in the light of recent observations. Congenit Anom (Kyoto). 50**,** 141-58.

Olesen, S. P., Clapham, D. E., Davies, P. F., 1988. Haemodynamic shear stress activates a K+ current in vascular endothelial cells. Nature. 331**,** 168-70.

Olivetti, G., Anversa, P., Melissari, M., Loud, A. V., 1980. Morphometry of medial hypertrophy in the rat thoracic aorta. Lab Invest. 42**,** 559-65.

Oosterbaan, A. M., Ursem, N. T., Struijk, P. C., Bosch, J. G., van der Steen, A. F., Steegers, E. A., 2009. Doppler flow velocity waveforms in the embryonic chicken heart at developmental stages corresponding to 5-8 weeks of human gestation. Ultrasound Obstet Gynecol. 33**,** 638-44.

Orhan, G., Baron, S., Norozi, K., Manner, J., Hornung, O., Blume, H., Misske, J., Heimann, B., Wessel, A., Yelbuz, T. M., 2007. Construction and establishment of a new environmental chamber to study real-time cardiac development. Microsc Microanal. 13**,** 204-10.

Othman-Hassan, K., Patel, K., Papoutsi, M., Rodriguez-Niedenfuhr, M., Christ, B., Wilting, J., 2001. Arterial identity of endothelial cells is controlled by local cues. Dev Biol. 237**,** 398-409.

Parrish, J. A., 1981. New concepts in therapeutic photomedicine: photochemistry, optical targeting and the therapeutic window. J Invest Dermatol. 77**,** 45-50.

Patrick, M. J., Chen, C. Y., Frakes, D. H., Dur, O., Pekkan, K., 2011. Cellular-level near-wall unsteadiness of high-hematocrit erythrocyte flow using confocal μPIV. Experiments in Fluids. 50**,** 887-904.

Patten, B. M., 1920. The early embryology of the chick. P. Blakiston's Son & Co., Philadelphia.

Patten, B. M., Kramer, T. C., 1933. The initiation of contraction in the embryonic chick heart. American Journal of Anatomy. 53**,** 349-375.

Payli, R., Pekkan, K., Zelicourt, D., Frakes, D., Sotiropoulos, F., Yoganathan, A., High Performance Clinical Computing on the TeraGrid: Patient-Specific Hemodynamic Analysis and Surgical Planning. TeraGrid 2007 Conference Madison, WI, 2007.

Pekkan, K., Dasi, L., Dur, O., Keller, B. B., Fogel, M., Yoganathan, A. P., In vitro hemodynamics of embryonic heart with Tetralogy of Fallot at late gestation. Fifth International Caltech Bio-Fluid Symposium and Workshop, California Institute of Technology, Pasadena, California, 2008a.

Pekkan, K., Dasi, L. P., Nourparvar, P., Yerneni, S., Tobita, K., Fogel, M. A., Keller, B., Yoganathan, A., 2008b. In vitro hemodynamic investigation of the embryonic aortic arch at late gestation. J Biomech. 41**,** 1697-706.

Pekkan, K., Dur, O., Sundareswaran, K., Kanter, K., Fogel, M., Yoganathan, A., Undar, A., 2008c. Neonatal aortic arch hemodynamics and perfusion during cardiopulmonary bypass. J Biomech Eng. 130**,** 061012.

Pekkan, K., Dur, O., Zelicourt, D., Payli, R., Sotiropoulos, F., Kowalski, W. J., Chen, C.-Y., Patrick, M. J., Kara, L., Keller, B. B., Embryonic intra-cardiac flow fields at three idealized ventricular morphologies. 62nd Annual Meeting of the APS Division of Fluid Dynamics, Minneapolis, MN, 2009.

Pekkan, K., Keller, B. B., 2013. Guest Editorial: Special Issue on Fetal Hemodynamics. Cardiovascular Engineering and Technology. 1-3.

Pekkan, K., Whited, B., Kanter, K., Sharma, S., de Zelicourt, D., Sundareswaran, K., Frakes, D., Rossignac, J., Yoganathan, A. P., 2008d. Patient-specific surgical planning and hemodynamic computational fluid dynamics optimization through free-form haptic anatomy editing tool (SURGEM). Med Biol Eng Comput. 46**,** 1139-52.

Person, A. D., Klewer, S. E., Runyan, R. B., 2005. Cell biology of cardiac cushion development. Int Rev Cytol. 243**,** 287-335.

Pexieder, T., 1969. Some quantitative aspects on the development of aortic arches in chick embryos between the 2nd and 8th day of incubation. Folia Morphol (Praha). 17**,** 102-36.

Pickering, J. W., 1893. Observations on the Physiology of the Embryonic Heart. J Physiol. 14**,** 382 2-466.

Piiper, J., 1982. Respiratory gas exchange at lungs, gills and tissues: mechanisms and adjustments. Journal of Experimental Biology. 100**,** 5-22.

Pilch, M., Wenner, Y., Strohmayr, E., Preising, M., Friedburg, C., Meyer Zu Bexten, E., Lorenz, B., Stieger, K., 2012. Automated segmentation of retinal blood vessels in spectral domain optical coherence tomography scans. Biomed Opt Express. 3**,** 1478-91.

Poelma, C., Kloosterman, A., Hierck, B. P., Westerweel, J., 2012. Accurate blood flow measurements: are artificial tracers necessary? PLoS One. 7**,** e45247.

Poelma, C., Van der Heiden, K., Hierck, B. P., Poelmann, R. E., Westerweel, J., 2010. Measurements of the wall shear stress distribution in the outflow tract of an embryonic chicken heart. Journal of the Royal Society Interface. 7**,** 91-103.

Poelma, C., Vennemann, P., Lindken, R., Westerweel, J., 2008. In vivo blood flow and wall shear stress measurements in the vitelline network. Exp Fluids. 45.

Poelmann, R. E., Gittenberger-de Groot, A. C., Hierck, B. P., 2008. The development of the heart and microcirculation: role of shear stress. Med Biol Eng Comput. 46**,** 479-84.

Pries, A. R., Reglin, B., Secomb, T. W., 2001. Structural adaptation of microvascular networks: functional roles of adaptive responses. Am J Physiol Heart Circ Physiol. 281**,** H1015-25.

Pries, A. R., Secomb, T. W., Gaehtgens, P., 1995. Design principles of vascular beds. Circulation Research. 77**,** 1017-23.

Pries, A. R., Secomb, T. W., Gaehtgens, P., 1998. Structural adaptation and stability of microvascular networks: theory and simulations. Am J Physiol. 275**,** H349-60.

Qayyum, S. R., Webb, S., Anderson, R. H., Verbeek, F. J., Brown, N. A., Richardson, M. K., 2001. Septation and valvar formation in the outflow tract of the embryonic chick heart. Anat Rec. 264**,** 273-83.

Ranger, A. M., Grusby, M. J., Hodge, M. R., Gravallese, E. M., de la Brousse, F. C., Hoey, T., Mickanin, C., Baldwin, H. S., Glimcher, L. H., 1998. The transcription factor NF-ATc is essential for cardiac valve formation. Nature. 392**,** 186-90.

Rawles, M. E., 1943. The heart-forming areas of the early chick blastoderm. Physiological Zoology. 16.

Reckova, M., Rosengarten, C., deAlmeida, A., Stanley, C. P., Wessels, A., Gourdie, R. G., Thompson, R. P., Sedmera, D., 2003. Hemodynamics is a key epigenetic factor in development of the cardiac conduction system. Circulation Research. 93**,** 77-85.

Redkar, A., Montgomery, M., Litvin, J., 2001. Fate map of early avian cardiac progenitor cells. Development. 128**,** 2269-79.

Rodbard, S., 1975. Vascular caliber. Cardiology. 60**,** 4-49.

Rodefeld, M. D., Boyd, J. H., Myers, C. D., LaLone, B. J., Bezruczko, A. J., Potter, A. W., Brown, J. W., 2003. Cavopulmonary assist: circulatory support for the univentricular Fontan circulation. Ann Thorac Surg. 76**,** 1911-6.

Rodriguez, E. K., Hoger, A., McCulloch, A. D., 1994. Stress-dependent finite growth in soft elastic tissues. J Biomech. 27**,** 455-67.

Roger, V. L., Go, A. S., Lloyd-Jones, D. M., Adams, R. J., Berry, J. D., Brown, T. M., Carnethon, M. R., Dai, S., de Simone, G., Ford, E. S., Fox, C. S., Fullerton, H. J., Gillespie, C., Greenlund, K. J., Hailpern, S. M., Heit, J. A., Ho, P. M., Howard, V. J., Kissela, B. M., Kittner, S. J., Lackland, D. T., Lichtman, J. H., Lisabeth, L. D., Makuc, D. M., Marcus, G. M., Marelli, A., Matchar, D. B., McDermott, M. M., Meigs, J. B., Moy, C. S., Mozaffarian, D., Mussolino, M. E., Nichol, G., Paynter, N. P., Rosamond, W. D., Sorlie, P. D., Stafford, R. S., Turan, T. N., Turner, M. B., Wong, N. D., Wylie-Rosett, J., 2011. Heart disease and stroke statistics--2011 update: a report from the American Heart Association. Circulation. 123**,** e18-e209.

Roman, B. L., Pekkan, K., 2012. Mechanotransduction in embryonic vascular development. Biomech Model Mechanobiol. 11**,** 1149-68.

Rosenquist, G. C., 1971a. The common cardinal veins in the chick embryo: their origin and development as studied by radioautographic mapping. Anat Rec. 169**,** 501-7.

Rosenquist, G. C., 1971b. Pulmonary veins in the chick embryo: origin as determined by radioautographic mapping. Anat Rec. 169**,** 65-9.

Rugonyi, S., Shaut, C., Liu, A., Thornburg, K., Wang, R. K., 2008. Changes in wall motion and blood flow in the outflow tract of chick embryonic hearts observed with optical

coherence tomography after outflow tract banding and vitelline-vein ligation. Phys Med Biol. 53**,** 5077-91.
Rychik, J., Rome, J. J., Collins, M. H., DeCampli, W. M., Spray, T. L., 1999. The hypoplastic left heart syndrome with intact atrial septum: atrial morphology, pulmonary vascular histopathology and outcome. J Am Coll Cardiol. 34**,** 554-60.
Rychter, Z., 1962. Experimental morphology of the aortic arches and the heart loop in chick embryos. Advances in Morphogenesis. 2**,** 333-371.
Rychter, Z., Kopecky, M., Lemez, L., 1955. A micromethod for determination of the circulating blood volume in chick embryos. Nature. 175**,** 1126-7.
Rychter, Z., Lemez, L., 1965. Changes in localization in aortic arches of laminar blood streams of main venous trunks to heart after exclusion of vitelline vessels on second day of incubation. Fed Proc Transl Suppl. 24**,** 815-20.
Sabin, F. R., 1917. Development of the primitive vessels of the chick and of the pig. Contributions to Embryology. 6**,** 63-U16.
Sadler, T. W., Langman, J., 2006. Langman's medical embryology. Lippincott Williams & Wilkins, Philadelphia.
Sanchez Gomez, C., Pliego Pliego, L., Contreras Ramos, A., Angel Munguia Rosas, M., Salazar Garcia, M., Garcia Romero, H. L., Gonzalez Jimenez, M. A., 2005. Histological study of the proximal and distal segments of the embryonic outflow tract and great arteries. Anat Rec A Discov Mol Cell Evol Biol. 283**,** 202-11.
Santhanakrishnan, A., Nguyen, N., Cox, J. G., Miller, L. A., 2009. Flow within models of the vertebrate embryonic heart. J Theor Biol. 259**,** 449-61.
Savolainen, S. M., Foley, J. F., Elmore, S. A., 2009. Histology atlas of the developing mouse heart with emphasis on E11.5 to E18.5. Toxicol Pathol. 37**,** 395-414.
Schittowski, K., 1985. NLQPL: A FORTRAN-Subroutine Solving Constrained Nonlinear Programming Problems. Annals of Operations Research. 5**,** 485-500.
Schroder, E. A., Tobita, K., Tinney, J. P., Foldes, J. K., Keller, B. B., 2002. Microtubule involvement in the adaptation to altered mechanical load in developing chick myocardium. Circ Res. 91**,** 353-9.
Sedmera, D., Cook, A. C., Shirali, G., McQuinn, T. C., 2005. Current issues and perspectives in hypoplasia of the left heart. Cardiol Young. 15**,** 56-72.
Sedmera, D., Hu, N., Weiss, K. M., Keller, B. B., Denslow, S., Thompson, R. P., 2002. Cellular changes in experimental left heart hypoplasia. Anat Rec. 267**,** 137-45.
Sedmera, D., Pexieder, T., Rychterova, V., Hu, N., Clark, E. B., 1999. Remodeling of chick embryonic ventricular myoarchitecture under experimentally changed loading conditions. Anat Rec. 254**,** 238-52.
Sedmera, D., Pexieder, T., Vuillemin, M., Thompson, R. P., Anderson, R. H., 2000. Developmental patterning of the myocardium. Anat Rec. 258**,** 319-37.
Sherman, T. F., 1981. On connecting large vessels to small. The meaning of Murray's law. J Gen Physiol. 78**,** 431-53.
Shiau, C. E., Lwigale, P. Y., Das, R. M., Wilson, S. A., Bronner-Fraser, M., 2008. Robo2-Slit1 dependent cell-cell interactions mediate assembly of the trigeminal ganglion. Nat Neurosci. 11**,** 269-76.
Shibeshi, S. S., Collins, W. E., 2005. The Rheology of Blood Flow in a Branched Arterial System. Appl Rheol. 15**,** 398-405.

Smith, B. R., Effmann, E. L., Johnson, G. A., 1992. MR microscopy of chick embryo vasculature. J Magn Reson Imaging. 2**,** 237-40.
Stekelenburg-de Vos, S., Ursem, N. T., Hop, W. C., Wladimiroff, J. W., Gittenberger-de Groot, A. C., Poelmann, R. E., 2003. Acutely altered hemodynamics following venous obstruction in the early chick embryo. Journal of Experimental Biology. 206**,** 1051-7.
Stewart, D. E., Kirby, M. L., Sulik, K. K., 1986. Hemodynamic changes in chick embryos precede heart defects after cardiac neural crest ablation. Circulation Research. 59**,** 545-50.
Strilic, B., Kucera, T., Eglinger, J., Hughes, M. R., McNagny, K. M., Tsukita, S., Dejana, E., Ferrara, N., Lammert, E., 2009. The molecular basis of vascular lumen formation in the developing mouse aorta. Dev Cell. 17**,** 505-15.
Strilic, B., Kucera, T., Lammert, E., 2010. Formation of cardiovascular tubes in invertebrates and vertebrates. Cell Mol Life Sci. 67**,** 3209-18.
Sun, S., Wheeler, M. F., Obeyesekere, M., Patrick, C. W., Jr., 2005. A deterministic model of growth factor-induced angiogenesis. Bull Math Biol. 67**,** 313-37.
Taber, L. A., 1998a. Mechanical aspects of cardiac development. Prog Biophys Mol Biol. 69**,** 237-55.
Taber, L. A., 1998b. A model for aortic growth based on fluid shear and fiber stresses. J Biomech Eng. 120**,** 348-54.
Taber, L. A., 1998c. An optimization principle for vascular radius including the effects of smooth muscle tone. Biophys J. 74**,** 109-14.
Taber, L. A., 2009. Towards a unified theory for morphomechanics. Philos Transact A Math Phys Eng Sci. 367**,** 3555-83.
Taber, L. A., Chabert, S., 2002. Theoretical and experimental study of growth and remodeling in the developing heart. Biomech Model Mechanobiol. 1**,** 29-43.
Taber, L. A., Eggers, D. W., 1996. Theoretical study of stress-modulated growth in the aorta. J Theor Biol. 180**,** 343-57.
Taber, L. A., Humphrey, J. D., 2001. Stress-modulated growth, residual stress, and vascular heterogeneity. J Biomech Eng. 123**,** 528-35.
Taber, L. A., Ng, S., Quesnel, A. M., Whatman, J., Carmen, C. J., 2001. Investigating Murray's law in the chick embryo. J Biomech. 34**,** 121-4.
Taber, L. A., Zhang, J., Perucchio, R., 2007. Computational model for the transition from peristaltic to pulsatile flow in the embryonic heart tube. J Biomech Eng. 129**,** 441-9.
Tallquist, M. D., Soriano, P., 2003. Cell autonomous requirement for PDGFRalpha in populations of cranial and cardiac neural crest cells. Development. 130**,** 507-18.
Tan, H., Junor, L., Price, R. L., Norris, R. A., Potts, J. D., Goodwin, R. L., 2011. Expression and deposition of fibrous extracellular matrix proteins in cardiac valves during chick development. Microsc Microanal. 17**,** 91-100.
Teddy, J. M., Lansford, R., Kulesa, P. M., 2005. Four-color, 4-D time-lapse confocal imaging of chick embryos. Biotechniques. 39**,** 703-10.
Tedgui, A., Merval, R., Esposito, B., 1992. Albumin transport characteristics of rat aorta in early phase of hypertension. Circ Res. 71**,** 932-42.
Thoma, R., 1893. Untersuchungen über die Histogenese und Histomechanik des Gefässsystems. Verlag von Ferdinand Enke, Stuttgart.

Thompson, R. P., Abercrombie, V., Wong, M., 1987. Morphogenesis of the truncus arteriosus of the chick embryo heart: movements of autoradiographic tattoos during septation. Anat Rec. 218**,** 434-40, 394-5.

Tobita, K., Garrison, J. B., Liu, L. J., Tinney, J. P., Keller, B. B., 2005. Three-dimensional myofiber architecture of the embryonic left ventricle during normal development and altered mechanical loads. Anat Rec A Discov Mol Cell Evol Biol. 283**,** 193-201.

Tobita, K., Keller, B. B., 2000. Right and left ventricular wall deformation patterns in normal and left heart hypoplasia chick embryos. Am J Physiol Heart Circ Physiol. 279**,** H959-69.

Tzima, E., Irani-Tehrani, M., Kiosses, W. B., Dejana, E., Schultz, D. A., Engelhardt, B., Cao, G., DeLisser, H., Schwartz, M. A., 2005. A mechanosensory complex that mediates the endothelial cell response to fluid shear stress. Nature. 437**,** 426-31.

Ursem, N. T., Struijk, P. C., Poelmann, R. E., Gittenberger-de Groot, A. C., Wladimiroff, J. W., 2001. Dorsal aortic flow velocity in chick embryos of stage 16 to 28. Ultrasound in medicine & biology. 27**,** 919-24.

Valentin, A., Humphrey, J. D., Holzapfel, G. A., 2011. A multi-layered computational model of coupled elastin degradation, vasoactive dysfunction, and collagenous stiffening in aortic aging. Annals of Biomedical Engineering. 39**,** 2027-45.

van den Berg, G., Moorman, A. F., 2011. Development of the pulmonary vein and the systemic venous sinus: an interactive 3D overview. PLoS One. 6**,** e22055.

Van der Heiden, K., Groenendijk, B. C., Hierck, B. P., Hogers, B., Koerten, H. K., Mommaas, A. M., Gittenberger-de Groot, A. C., Poelmann, R. E., 2006. Monocilia on chicken embryonic endocardium in low shear stress areas. Dev Dyn. 235**,** 19-28.

Vennemann, P., Kiger, K. T., Lindken, R., Groenendijk, B. C., Stekelenburg-de Vos, S., ten Hagen, T. L., Ursem, N. T., Poelmann, R. E., Westerweel, J., Hierck, B. P., 2006. In vivo micro particle image velocimetry measurements of blood-plasma in the embryonic avian heart. J Biomech. 39**,** 1191-200.

Vermot, J., Forouhar, A. S., Liebling, M., Wu, D., Plummer, D., Gharib, M., Fraser, S. E., 2009. Reversing blood flows act through klf2a to ensure normal valvulogenesis in the developing heart. PLoS Biol. 7**,** e1000246.

Voronov, D. A., Alford, P. W., Xu, G., Taber, L. A., 2004. The role of mechanical forces in dextral rotation during cardiac looping in the chick embryo. Dev Biol. 272**,** 339-50.

Wagenseil, J. E., 2010. A constrained mixture model for developing mouse aorta. Biomech Model Mechanobiol.

Wagman, A. J., Hu, N., Clark, E. B., 1990. Effect of Changes in Circulating Blood-Volume on Cardiac-Output and Arterial and Ventricular Blood-Pressure in the Stage-18, Stage-24, and Stage-29 Chick-Embryo. Circulation Research. 67**,** 187-192.

Waldo, K. L., Hutson, M. R., Stadt, H. A., Zdanowicz, M., Zdanowicz, J., Kirby, M. L., 2005a. Cardiac neural crest is necessary for normal addition of the myocardium to the arterial pole from the secondary heart field. Dev Biol. 281**,** 66-77.

Waldo, K. L., Hutson, M. R., Ward, C. C., Zdanowicz, M., Stadt, H. A., Kumiski, D., Abu-Issa, R., Kirby, M. L., 2005b. Secondary heart field contributes myocardium and smooth muscle to the arterial pole of the developing heart. Dev Biol. 281**,** 78-90.

Waldo, K. L., Kumiski, D., Kirby, M. L., 1996. Cardiac neural crest is essential for the persistence rather than the formation of an arch artery. Dev Dyn. 205**,** 281-92.

Waldo, K. L., Kumiski, D. H., Wallis, K. T., Stadt, H. A., Hutson, M. R., Platt, D. H., Kirby, M. L., 2001. Conotruncal myocardium arises from a secondary heart field. Development. 128**,** 3179-88.

Wang, J., Nagy, A., Larsson, J., Dudas, M., Sucov, H. M., Kaartinen, V., 2006. Defective ALK5 signaling in the neural crest leads to increased postmigratory neural crest cell apoptosis and severe outflow tract defects. BMC Dev Biol. 6**,** 51.

Wang, Y., Dur, O., Patrick, M. J., Tinney, J. P., Tobita, K., Keller, B. B., Pekkan, K., 2009. Aortic arch morphogenesis and flow modeling in the chick embryo. Ann Biomed Eng. 37**,** 1069-81.

Warkman, A. S., Krieg, P. A., 2007. Xenopus as a model system for vertebrate heart development. Semin Cell Dev Biol. 18**,** 46-53.

Watanabe, M., Choudhry, A., Berlan, M., Singal, A., Siwik, E., Mohr, S., Fisher, S. A., 1998. Developmental remodeling and shortening of the cardiac outflow tract involves myocyte programmed cell death. Development. 125**,** 3809-20.

Watanabe, M., Jafri, A., Fisher, S. A., 2001. Apoptosis is required for the proper formation of the ventriculo-arterial connections. Dev Biol. 240**,** 274-88.

Watton, P. N., Raberger, N. B., Holzapfel, G. A., Ventikos, Y., 2009. Coupling the hemodynamic environment to the evolution of cerebral aneurysms: computational framework and numerical examples. J Biomech Eng. 131**,** 101003.

Ya, J., van den Hoff, M. J., de Boer, P. A., Tesink-Taekema, S., Franco, D., Moorman, A. F., Lamers, W. H., 1998. Normal development of the outflow tract in the rat. Circ Res. 82**,** 464-72.

Yalcin, H. C., Shekhar, A., McQuinn, T. C., Butcher, J. T., 2011. Hemodynamic patterning of the avian atrioventricular valve. Dev Dyn. 240**,** 23-35.

Yashiro, K., Shiratori, H., Hamada, H., 2007. Haemodynamics determined by a genetic programme govern asymmetric development of the aortic arch. Nature. 450**,** 285-8.

Yelbuz, T. M., Choma, M. A., Thrane, L., Kirby, M. L., Izatt, J. A., 2002. Optical coherence tomography: a new high-resolution imaging technology to study cardiac development in chick embryos. Circulation. 106**,** 2771-4.

Yelbuz, T. M., Leatherbury, L., Johnson, M., Wolfe, R. R., Kirby, M. L., 2000. Quantitative Analyse der Ventrikelfunktion imfrühen embryonalen Herzen in "schalen-losen" Kulturen nach Ablation der Neuralleiste. Z. Kardiol. 89.

Yelbuz, T. M., Zhang, X., Choma, M. A., Stadt, H. A., Zdanowicz, M., Johnson, G. A., Kirby, M. L., 2003. Images in cardiovascular medicine. Approaching cardiac development in three dimensions by magnetic resonance microscopy. Circulation. 108**,** e154-5.

Yoshida, H., Manasek, F., Arcilla, R. A., 1983. Intracardiac flow patterns in early embryonic life. A reexamination. Circ Res. 53**,** 363-71.

Yoshigi, M., Knott, G. D., Keller, B. B., 2000. Lumped parameter estimation for the embryonic chick vascular system: a time-domain approach using MLAB. Comput Methods Programs Biomed. 63**,** 29-41.

Yousefi, S., Qin, J., Zhi, Z., Wang, R. K., 2013. Label-free optical lymphangiography: development of an automatic segmentation method applied to optical coherence tomography to visualize lymphatic vessels using Hessian filters. J Biomed Opt. 18**,** 86004.

Zamir, M., 1977. Shear forces and blood vessel radii in the cardiovascular system. J Gen Physiol. 69**,** 449-61.

Zhang, X., Yelbuz, T. M., Cofer, G. P., Choma, M. A., Kirby, M. L., Johnson, G. A., 2003. Improved preparation of chick embryonic samples for magnetic resonance microscopy. Magn Reson Med. 49**,** 1192-5.

Zheng, H. R., Liu, L. L., Williams, L., Hertzberg, J. R., Lanning, C., Shandas, R., 2006. Real time multicomponent echo particle image velocimetry technique for opaque flow imaging. Applied Physics Letters. 88.

Appendix A. Protocols for Chick Embryo Manipulation

Protocol E1
Microneedle Fabrication

1) Materials Needed:
   a) Narishige PC-10 Puller
   b) Narishige EG-44 Microgrinder
   c) A 1.0 mm ID glass capillary tube (WPI, thin wall with filament, TW100F-5)
   d) Forceps (WPI,14099, Dumont #55)

1. Pulling
   1.1. Take 1.0 mm ID glass capillary tube and place in between slots indicated by (A) in Figure A-1. The tube should be centered so that after pulling, each needle is of similar proportions. Ensure that the tube is gently slid within the heating coil so that it does not crack.
   1.2. Turn the knob indicated by (D) to step 1. This will result in a tip about 0.3 micrometers. For elongated cone shaped needle tips, this is only a one step process. Refer to the manual for different shape settings.
   1.3. The NO. 1 heater Adjuster should be set to around 66. 5.
   1.4. Press the start button. The coil should heat up and the weight should drop resulting in two needles.
   1.5. Shut the puller off and remove one needle for inspection
   1.6. Using a microscope inspect the needle for any blockage.
   1.7. With forceps, gently grasp the end of the needle and break it off into a diagonally shaped form leaving about 3 mm
   1.8. While maintaining the orientation of the point so that it opens downwards, place the needle in the grinder.

2. Grinding
   2.1. With the needle in the correct orientation as shown by Figure A-2, place it in the appropriate slot in the Narishige EG-44 microgrinder as shown by Figure A-3 (A).
   2.2. Set the dial to 25^{o}
   2.3. Set the motor adjuster as shown by Figure A-3 (B), to approximately 75.
   2.4. Fill the 30ml dropper with distilled water, Figure A-3 (D) and set so that it flows at one drop per second, or enough to consistently moisten the disk below.
   2.5. Press the power switch and slowly lower the needle onto the disk using the knob shown by Figure A-3 (C), until its contact can be heard.
   2.6. To ensure that the needle just barely touches the surface of the disk shine a light directly onto it and lower until the needle meets it shadow.
   2.7. Run for 30 minutes and inspect under microscope for any blockage or cracks

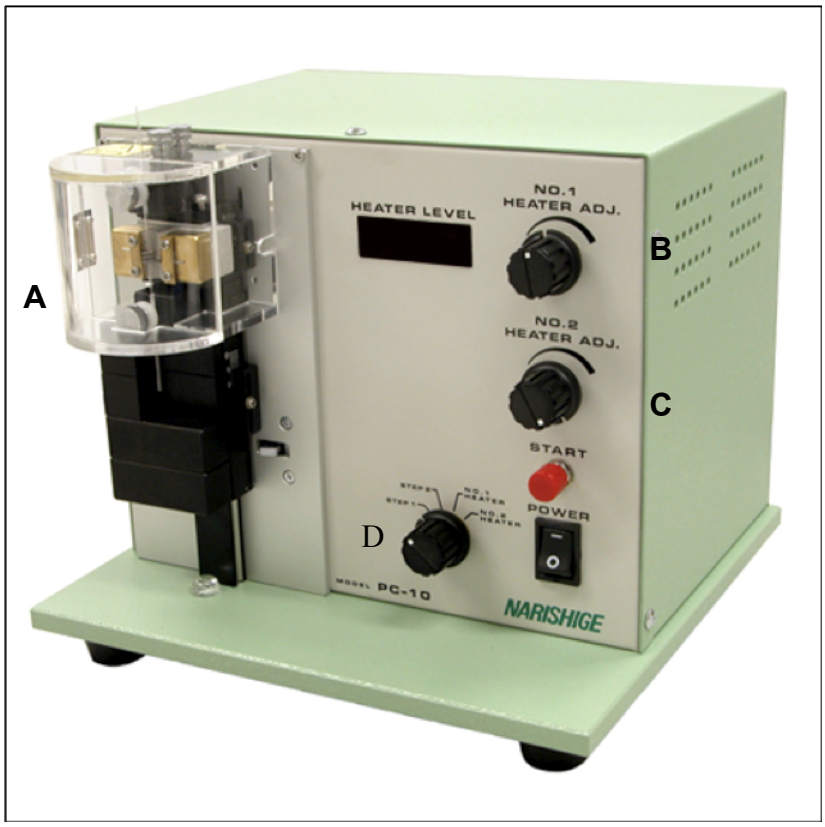

Figure A-1. Narishige PC-10 Puller.

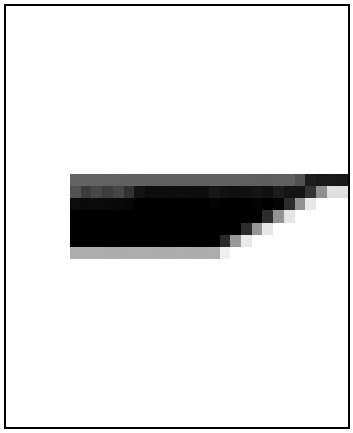

Figure A-2. Slanted needle point should face downwards.

Figure A-3. Narishige EG-44 Microgrinder.

Protocol E2
Microinjection of Chick Embryos *in ovo*

1) Materials and Equipment Used
   a) Stereomicroscope (Leica M165FC w/DFC350FX camera)
   b) Micromanipulator (Leitz 3-axis micromanipulator)
   c) External light source (Fostec 150W)
   d) Hamilton gastight syringe, either luer-tip or removable needle type (Fisher Scientific)
   e) 20 gauge blunt tip needle – if using luer-tip type syringe
   f) Removable needle for Hamilton syringe – if using removable-needle type syringe
   g) Epoxy – if using removable-needle type syringe
   h) PE-60 tubing (Braintree Scientific, PE-60-CL-50, 0.048" OD x 0.030" ID)
   i) A 1.0 mm ID glass capillary tube (WPI, thin wall with filament, TW100F-5)
   j) 28 gauge MicroFil (WPI, MF28G-5, 250 μm ID x 350 μm OD)
   k) Injection solution
   l) Chick embryo *in ovo* (white Leghorn)
   m) Egg holding ring
   n) Forceps (WPI, 14099, Dumont #55)
   o) Microscissors (WPI, 14122, curved 5mm blades x 0.1 mm tips)

1. A Hamilton gastight luer-tip syringe is connected to a 20 gauge blunt tip needle. Alternatively, a Hamilton gastight removable-needle syringe with corresponding needle can be used. Approximately 10 cm of PE-60 tubing is connected to the needle. If using the removable needle type syringe, epoxy can be used to obtain a secure seal. The syringe, needle and tubing are fastened to a micromanipulator. See Figure A-4.
2. The syringe, needle, and tubing are primed with the injection solution. If using a small volume syringe with small bore, a 28 gauge MicroFil needle can be used for priming.
3. A 1.0 mm ID glass capillary tube is pulled and beveled to a ~30 μm, 20° tip microneedle. See Protocol E1 for instructions.
4. The microneedle is primed with the injection solution using a 28 gauge MicroFil needle.
5. The primed microneedle is connected to the open end of the PE-60 tubing. Care should be taken not to introduce air into the system. The microneedle is held stationary using the shim insert. The entire set up is positioned for injection under a stereomicroscope. See Figure A-4.
6. A chick egg at the desired stage is removed from the incubator and windowed.
7. The entire egg is positioned under a stereomicroscope and the embryo is oriented to facilitate injection at the desired site. See Figure A-5.
8. Using the micromanipulator, the microneedle is positioned at the desired injection site and gently advanced to puncture the vascular tissue. Blood cells should be observed within the tip of the microneedle to ensure penetration into the lumen. Bleeding should not be observed, as it indicates a complete puncture through the vessel. If bleeding is observed, the microneedle is withdrawn and the embryo discarded.
9. The desired volume of solution is injected by depressing the plunger of the syringe. Light pressure should be applied so as to not burst the delicate embryo.
10. The microneedle is withdrawn from the vessel using the micromanipulator.

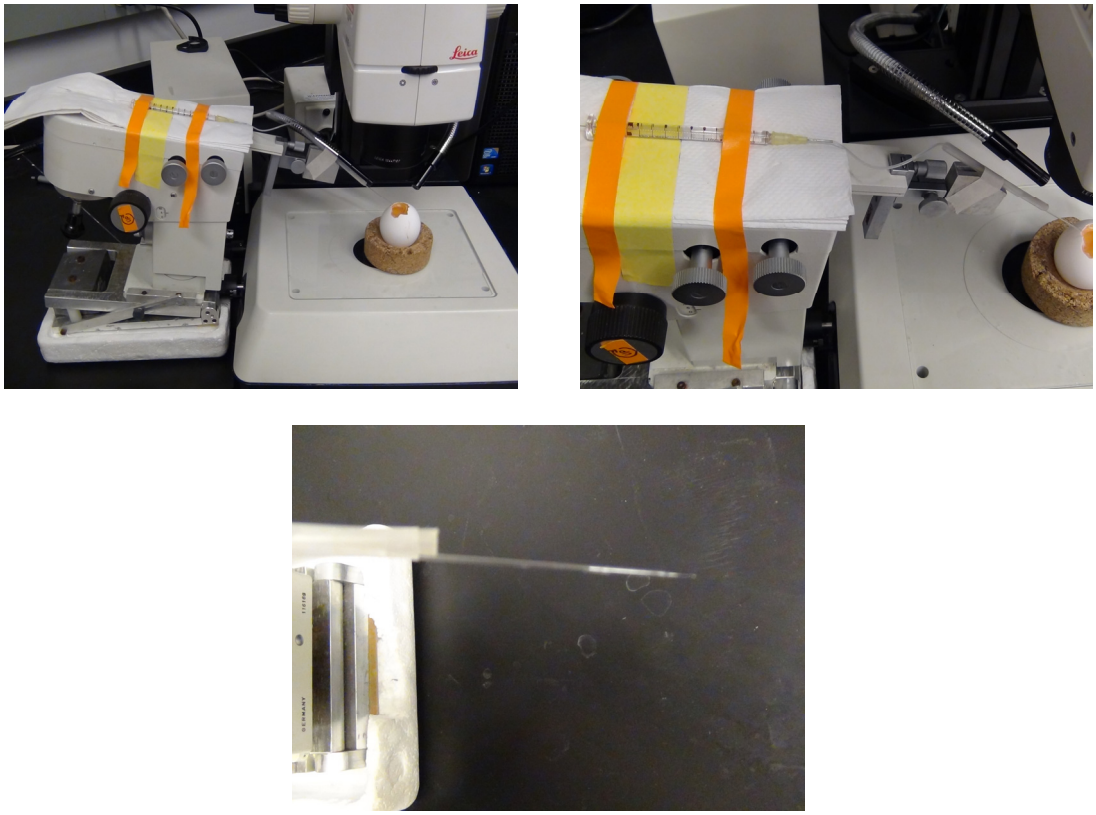

Figure A-4. Pre-injection set-up. The syringe, needle, tubing, and microneedle are mounted on the micromanipulator. The windowed egg is placed under the microscope.

Figure A-5. The embryo is oriented to facilitate injection at the desired location (ventricular apex). The needle is positioned for puncture.

Protocol E3
Perfusion Fixation of Chick Embryos

1) Materials needed
   a) A 100 µl Hamilton gastight luer-tip syringe (Fisher Scientific, 14-815-75, 1710LT 100UL) connected to a 20 gauge blunt end needle OR a100 µl Hamilton gastight removable-needle syringe with 22s gauge needle (Fisher Scientific, 14-815-80, 1710RN 100UL)
   b) PE-60 tubing (Braintree Scientific, PE-60-CL-50, 0.048" OD x 0.030" ID)
   c) Epoxy (if using removable needle syringe)
   d) A 1.0 mm ID glass capillary tube (WPI, thin wall with filament, TW100F-5)
   e) 28 gauge MicroFil (WPI, MF28G-5, 250 µm ID x 350 µm OD)
   f) Chick embryo (white Leghorn)
   g) Egg holding ring
   h) Forceps (WPI, 14099, Dumont #55)
   i) Microscissors (WPI, 14122, curved 5mm blades x 0.1 mm tips)
   j) Spoonulet (Fisher Scientific, 14-375-20)
   k) Microcentrifuge tubes (1-2ml volume)
   l) 10 cm petri dish
   m) Pipette, pipette tips (1ml)
   n) 4% paraformaldehyde solution
   o) Chick Ringer + 0.5 mM verapmil and 0.5 mM EGTA (alternative to paraformaldehyde if arresting in diastole)
   p) 1X PBS

1. Injection preparation
   1.1. A Hamilton syringe as specified in the materials is connected to a blunt end needle along with approximately 10 cm of PE-60 tubing. If using the 1710RN syringe with 22s gauge needle, epoxy can be applied to ensure a secure seal. The tubing may not be wide enough to accommodate the needle, so alternating between a capillary tube and forceps within the tubing should create an opening. The syringe, needle and tubing are fastened to a micromanipulator (see Protocol E2)
   1.2. The syringe, needle, and tubing are primed with 4% paraformaldehyde solution.
   1.3. A 1.0 mm ID glass capillary tube is pulled and beveled to a ~30 µm, 20° tip microneedle (see Protocol E1).
   1.4. The microneedle is primed with 4% paraformaldehyde solution using a 28 gauge MicroFil.
   1.5. The microneedle is connected to the PE-60 tubing. The entire set up is positioned for injection under a stereomicroscope.
2. Fertile chicken eggs are incubated blunt end up at 37°C and 60% relative humidity to the desired Hamburger Hamilton stage.
3. A small (1 cm^2) hole is made in the eggshell and the overlying extra embryonic (chorion, amnion) membranes are removed to expose the developing embryo.
4. The entire egg is positioned under a stereomicroscope and the embryo is oriented to facilitate injection. Injection sites can be modified according to the application, but a common site is

the ventricular apex. If the embryo is oriented in the left lateral view, the ventricle will be considerably obstructed. An arterial injection at the dorsal aorta can also be done. The vitelline veins are another acceptable injection site and preferred if the heart tissue is to be investigated.

5. Using the micromanipulator, the ventricular apex of the embryonic heart or desired vessel is punctured with the needle. Penetration into the lumen can be confirmed by a gentle retraction of the syringe plunger, upon which you should see some red blood cells flow into the needle.
6. Depressing the plunger, approximately 50 µl of paraformaldehyde is injected into the heart. The injected vessel becomes immediately transparent and the embryo gradually follows. Light pressure should be applied so as to not burst the delicate heart. Injection is complete at the cessation of the heartbeat.
7. The needle is extracted from the heart.
8. The embryo is left stationary for 15 minutes. During this time, the soft tissue of the embryo becomes more solid as the paraformaldehyde takes effect.

Note: the above instructions are for perfusion fixation, used for procedures that do not wish to study myocardial function (i.e. examine myocardial alignment of the ventricle). Alternatively, substitute Chick Ringer + 0.5 mM verapmil and 0.5 mM EGTA for the 4% paraformaldehyde to arrest the heart in diastole.

9. Using the spoonulet, the embryo is carefully removed from the yolk. Micro scissors or forceps can be used to cut the vitelline vessels.
10. The embryo is placed in a petri dish with 1X PBS for a 30 second wash to remove excess albumin and red blood cells.
11. At this point, the embryo can be trimmed of any extra membranes. Using the spoonulet, transfer the embryo and a drop or two of 1X PBS to the lid of the petri dish. Place under the stereomicroscope and trim away any excess membrane or tissue using the microscissors and forceps. Alternatively, this step can be done after fixation just before embedding.
12. The extracted embryo is placed in a microcentrifuge tube with 2 ml of 4% paraformaldehyde. The embryo remains immersed in paraformaldehyde for 1 hour or overnight.

Protocol E4
Polyacrylamide Embedding of Chick Embryos

1) Materials needed
   a) Fixed chick embryo in 4% paraformaldehyde in microcentrifuge tube (from Protocol E3)
   b) Forceps (WPI, 14099, Dumont #55)
   c) Microscissors (WPI, 14122, curved 5mm blades x 0.1 mm tips)
   d) Spoonulet (Fisher Scientific, 14-375-20)
   e) Stainless-steel mold (Fisher Scientific, 64-010-15, 10 x 10 x 5 mm) OR an acceptable alternative mold
   f) Microcentrifuge tubes (1-2ml volume)
   g) 10 cm petri dish
   h) Pipette, pipette tips (1ml)
   i) 1X PBS
   j) 13% acrylamide solution (for acrylamide embedding only)
   k) 2% ammonium persulfate (fresh) (for acrylamide embedding only)

1. Using forceps, the fixed embryo is carefully removed from the microcentrifuge tube and placed in a petri dish with a thin layer of 1X PBS. The petri dish is swirled to rinse the embryo.
2. At this point, the embryo can be placed under the stereomicroscope and trimmed using forceps and microscissors in order to gain optimal orientation when embedding. The orientation of the embryo within the embedding material critical and should be carefully chosen to obtain useful and advantageous sectioning.
3. Acrylamide Embedding (50-200 μm sections)
   3.1. Using a pipette, a thin layer of 13% acrylamide gel is poured into the stainless-steel mold. This layer should barely cover the bottom of the mold.
   3.2. Using a pipette, 2% ammonium persulfate is added, drop by drop, to the acrylamide solution in the mold. The ammonium persulfate causes the acrylamide to polymerize, and in general, 7-10 drops are added. The acrylamide should sit until it begins to gel.
   3.3. The trimmed embryo is placed into the acrylamide mold. Obtaining the optimal orientation is critical here. Allowing the acrylamide to partially solidify beforehand makes this step easier.
   3.4. Once the embryo is properly oriented, the mold is filled to the top with 13% acrylamide and 2% ammonium persulfate is added drop by drop to polymerize. In general, 5-10 drops can be added.
   3.5. The entire mold should sit until it has begun to polymerize. Fresh solutions should be prepared and kept cool up to 12 hours in order for polymerization to occur in a timely manner.
   3.6. The entire mold is placed in a petri dish and covered in 1X PBS (to prevent drying) and stored in a refrigerator at 4°C for at least one day and up to 4 months before sectioning.

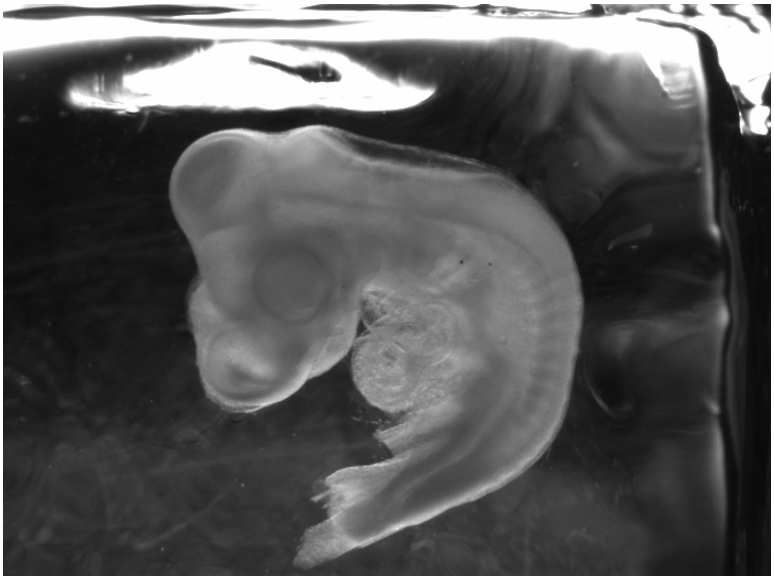

Figure A-6. Fixed HH21 chick embryo embedded in a polyacrylamide block.

Protocol E5
Vibratome Sectioning of Polyacrylamide Embedded Chick Embryos

1) Materials needed
   a) Vibrating-blade microtome, aka vibratome (Leica VT1000S)
      i) Knife holder
      ii) Buffer tray
      iii) Specimen disc
      iv) Injector razor blade (Shick)
      v) Allen key
      vi) Manipulator (has threaded end, screws into specimen disc)
   b) Cyanoacrylate adhesive (Krazy Glue)
   c) Kimwipes or filter paper
   d) 1X PBS
   e) 10 cm petri dish (2)
   f) 100 ml beaker
   g) Single edge razor blade (not the vibratome blade)
   h) Spoonulet (Fisher Scientific, 14-375-20)
   i) Lamp
   j) Glass slides
   k) Cover slips
   l) Clear nail polish

1. Mount polyacrylamide block with embedded tissue (see Protocol E4) to the specimen disc
   a) Using the spoonulet, carefully extract the polyacrylamide block from the mold into a bottom portion of a 10 cm petri dish filled with 1X PBS.
   b) Position the block so that it is in the exact orientation for slicing. The part of the polyacrylamide block intended to be attached to the specimen disc should be in full contact with the bottom of the petri dish
   c) Place the specimen disc next to the petri dish and apply a few drops of cyanoacrylate adhesive, enough so that the area covered is greater than the area of the base of the polyacrylamide block.
   d) Quickly, fold a kimwipe into quarters and stick it to the top of the polyacrylamide block. The moistness of the block will make the kimwipe stick.
   e) Quickly, using the kimwipe, transfer the polyacrylamide block from the petri dish to the specimen disc, making sure the bottom is completely within the cyanoacrylate area.
   f) Let the cyanoacrylate dry for 1 minute.
2. Place the specimen disc with polyacrylamide block attached into the vibratome
   a) Mount the buffer tray onto the bolt in the base of the vibratome. Turning the black lever on the buffer tray clockwise secures the buffer tray.
   b) Using the UP/DOWN button, lower the buffer tray to its lowest position (indicated by audible signal and red LED).
   c) Screw the manipulator (red handle) into the threaded hole in the specimen disc. Use the manipulator to place the specimen disc into the buffer tray. The notch in the

specimen disc lines up with the small bolt in the buffer tray to initially place it, then use the manipulator to rotate the disc to orient the block and secure the disc by tightening the bold with the Allen key. Unscrew the manipulator

d) When loading the specimen disc, the block should be at an oblique angle to the cutting direction (i.e. a corner of the block should point toward the blade).
e) Load a new injector blade into the knife holder and secure with the clamping screw using the Allen key.
f) Fix the knife holder to the vibratome.
g) Set the SPEED to 10 temporarily.
h) Using the REV/FORW button, place the knife edge right behind the rear edge of the specimen. This will be the start position for the slice.
i) Press the SINGLE/CONT button so that the green LED next to single is lit.
j) Press the section window button (the one with the two arrows) once. This sets the start position for the slice.
k) Use the REV/FORW button to place the edge of the knife just beyond the front edge of the specimen. This will be the end of the slice.
l) Press the section window button again (the one with the two arrows) to set this blade position as the end of the slice.
m) Use the REV/FORW button to move the knife back to about the first position.
n) Use the UP/DOWN button to move the top of the specimen to just at the level of the knife. If it is too far below the knife, you will cut air for a long time. If the block is too far above the knife, the first slice will be too thick and can ruin the specimen.
o) Fill the buffer tray with 1X PBS
p) Use the -/+ button to set the slice thickness (in μm). 150 μm is the recommended setting for polyacrylamide blocks.
q) Set the SPEED dial to just beyond the 0 mark. We want to use the lowest speed setting possible.
r) Set the FREQ dial to 10, the highest setting.
s) The amplitude of the vibratome should be at the highest setting (1 mm). See page 20, section 5.3 if you want to check the amplitude. If changed, return to 1 mm for the next user.

Note: the above instructions are generalized for sectioning a whole embryo embedded in a polyacrylamide block. Consult the Leica VT1000S manual for more detailed descriptions of the operating procedure.

3. Sectioning the specimen and collecting samples
    a) Place a 50 ml beaker filled with water next to the vibratome.
    b) Place a glass slide into an empty bottom portion of at 10 cm petri dish. Fill the dish with 1X PBS to just cover the slide. Cover the dish.
    c) Press the START button on the vibratome to begin sectioning. Each slice takes a long time, and we use single mode so the blade stops after each slice. Stopping the blade gives us time to collect the slice.
    d) Once the slice has been completed, the blade will automatically return to its first position.
    e) Use lamp to illuminate the buffer tray and scoop out the slice with the spoonulet. Usually, cornering the slice works to scoop it out.
    f) If the slice does not contain tissue, place in the 50 ml beaker filled with water.

g) If the slice contains tissue of interest, place it in the petri dish with glass slide. Re-cover the dish.
h) Press the START button to begin the next slice. The vibratome automatically moves the buffer tray.
i) Take the petri dish to a well-lit area. Use the spoonulet and forceps to place the slice onto the glass slide. As long as there is not too much PBS in the petri dish, the slice (or at least some of it) should stick to the slide so it doesn't move.
j) Multiple slices can be placed on the same slide, or you can do one slice per slide, depending on the application.
k) Repeat steps d-k for each slice.

Figure A-7. The Leica VT1000S.

Figure A-8. The Leica VT1000S control panel.

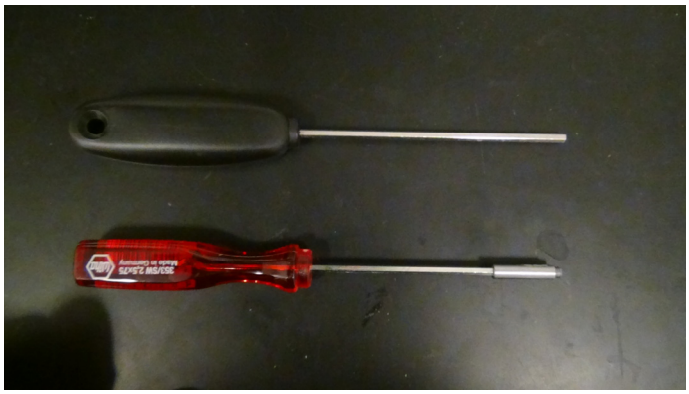

Figure A-9. Allen key (top) and Manipulator (bottom).

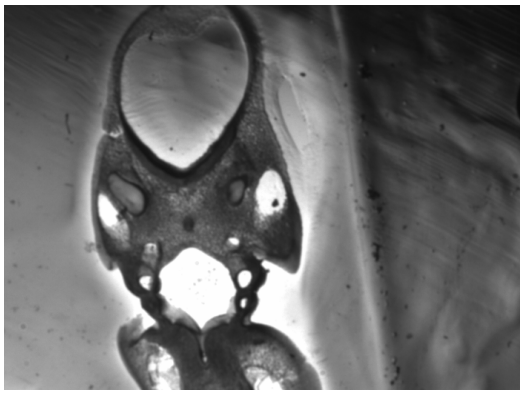

Figure A-10. A sample slice through the pharyngeal region of a HH21 chick embryo.

Protocol E6
Chick Ringer Solutions

Stock Chick Ringer Solution (Ca free)

	Concentration (mM)	Formula Weight (g/mol)	Amount for 1 L (g)	Sigma-Aldrich #
NaCl	135	58.440	7.889	71376
KCl	4	74.550	0.298	60129
Trizma-HCl	10	157.600	1.576	T5941
Trizma-base	10	121.140	1.211	T6066
Dextrose	11	180.160	1.982	G7520

pH adjusted to 7.4 at room temperature
Osmolality: 315-320 mOsm

Stock $CaCl_2$ solution

	Concentration (mM)	Formula Weight (g/mol)	Amount for 10 mL (g)	Sigma-Aldrich #
$CaCl_2$	1000	110.980	1.110	499609

To make 2mM Ca in 10 mL stock ringer solution:
add 0.02 mL (20 μL) stock $CaCl_2$ solution to 10 mL stock chick ringer solution

Note: according to the stock chick ringer solution, we can make 4 to 10 mM Ca solution without making new ringer solution (almost same osmolality).

High Potassium Chick Ringer Solution
adapted from: Tobita K, Schroder EA, Tinney JP, Garrison JB, Keller BB. 2002. Regional passive ventricular stress-strain relations during development of altered loads in chick embryo. *Am J Physiol Heart Circ Physiol*. 282:H2386-H2396

	Concentration (mM)	Formula Weight (g/mol)	Amount for 1 L (g)	Sigma-Aldrich #
NaCl	82	58.440	4.792	71376
KCl	60	74.550	4.473	60129
$CaCl_2$	2	110.980	0.222	499609
Trizma-HCl	10	157.600	1.576	T5941
Trizma-base	10	121.140	1.211	T6066
Dextrose	11	180.160	1.982	G7520

pH is adjusted to 7.4 at room temperature
Osmolality: 321 mOsm

Arrest Solution (add to High Potassium Chick Ringer Solution)

	Concentration (mM)	Formula Weight (g/mol)	Amount for 1 L (g)	Sigma-Aldrich #
Verapamil	0.5	491.060	0.246	V4629
EGTA	0.5	380.350	0.190	03777

Arrest at end-diastole (not zero-pressure)

Protocol E7
Polyacrylamide Solutions

4% Paraformaldehyde

	Amount	Sigma-Aldrich #
Paraformaldehyde	4g	158127
1X PBS	100ml	

To make 100ml 1X PBS, dilute 10ml 10X PBS with 90ml Millipore water (1:10 ratio 10X PBS:total volume).

13% Acrylamide Monomer

	Amount (ml)	Sigma-Aldrich #
30% Acrylimide	8.000	A3699
TEMED	0.310	T22500
3X PBS	6.000	
Millipore Water	3.700	

To make 10 ml 3X PBS, dilute 3ml 10X PBS with 7ml Millipore water (3:10 ratio 10X PBS:total volume).

Store at 4ºC for 1 month

2% Ammonium Persulfate

	Amount	Sigma-Aldrich #
Ammonium Persulfate	0.24g	A3678
Millipore Water	12.00ml	

The 2% ammonium persulfate must be fresh for proper polymerization.

Instructions:
To solidify the acrylimide, add 2% ammonium persulfate drop by drop.
It does not take much to solidify gel, but make sure it is dropped evenly over the sample

Store samples in a refrigerator after embedding with 1X PBS covering them to prevent the gel from drying out.

Appendix B. Environmental Chamber Parts List

Table B-1. Environmental Chamber Parts List.

Quantity	Item	Price
Enclosure		
(50)	5mm x 0.8mm allen head bolt	
(4)	3/4" hinges	
(3)	3/4" x 96" x .050" Alum. angles	$9.96
(2)	Door knobs	
(1)	9' x 1/4" x 1/4" foam weatherstrip	$4.00
(1)	36" x 72" x 0.220" Lexan plexiglass	$116.00
(1)	18" x 24" x 0.220" Lexan plexiglass	$19.97
Electronics		
(1)	Digital Temperature Controller	$16.99
(1)	120 x 25mm 110V fan	$12.00
(1)	Toggle Switch	
(1)	C13 Female Power Plug	
(1)	Computer power cord	
(1)	Light bulb socket	
(1)	250W heat lamp	
Total		$193.00

Appendix C. Publications and Conference Proceedings Resulting from this Thesis

Publications

1. Kowalski, W. J., Teslovich, N. C., Dur, O., Keller, B. B., Pekkan, K., 2012. Computational hemodynamic optimization predicts dominant aortic arch selection is driven by embryonic outflow tract orientation in the chick embryo. Biomech Model Mechanobiol. 11, 1057-73.

2. Kowalski, W. J., Dur, O., Wang, Y., Patrick, M. J., Tinney, J. P., Keller, B. B., Pekkan, K., 2013. Critical transitions in early embryonic aortic arch patterning and hemodynamics. PLoS One. 8, e60271.

3. Kowalski, W. J., Teslovich, N. C., Menon, P. G., Tinney, J. P., Keller, B. B., Pekkan, K., 2014. Left atrial ligation alters intracardiac flow patterns and the biomechanical landscape in the chick embryo. Dev Dyn. in press.

Conference Proceedings

1. Kowalski, W. J., Teslovich, N. C., Dur, O., Keller, B. B., Pekkan, K., Characterization of the outflow tract-aortic arch angle during embryonic development in the chick. BMES Annual Fall Meeting, Austin, TX, 2010.

2. Kowalski, W. J., Teslovich, N. C., Dur, O., Keller, B. B., Pekkan, K., Hemodynamics of aortic arch morphogenesis. USNCB 3rd Symposium on Frontiers in Biomechanics: Mechanics of Development, Farmington, PA, 2011.

3. Kowalski, W. J., Dur, O., Wang, Y., Tinney, J. P., Keller, B. B., Pekkan, K., Hemodynamics of the transitional aortic arch patterning at a key embryonic stage. ISACB 13th Biennial Meeting, London, UK, 2012.